VYSOKÉ UČENÍ TECHNICKÉ V BRNĚ
BRNO UNIVERSITY OF TECHNOLOGY

FAKULTA STROJNÍHO INŽENÝRSTVÍ
LETECKÝ ÚSTAV

FACULTY OF MECHANICAL ENGINEERING
INSTITUTE OF AEROSPACE ENGINEERING

VÝPOČETNÍ STUDIE MOŽNOSTÍ VYUŽITÍ AKTIVNÍHO ŘÍZENÍ PROUDU K SNÍŽENÍ INTENZITY KONCOVÝCH VÍRŮ NA KŘÍDLE

A COMPUTATIONAL STUDY ON THE EFFECTS OF ACTIVE FLOW CONTROL TO THE EVOLUTION OF THE WINGTIP VORTICES OF A THREE DIMENSIONAL WING

DIPLOMOVÁ PRÁCE
MASTER'S THESIS

AUTOR PRÁCE AUTHOR	Bc. VILÉM SKAROLEK
VEDOUCÍ PRÁCE SUPERVISOR	Ing. STAVROS KARAMPELAS, Ph.D.

BRNO 2012

Vysoké učení technické v Brně, Fakulta strojního inženýrství

Letecký ústav
Akademický rok: 2011/2012

ZADÁNÍ DIPLOMOVÉ PRÁCE

student(ka): Bc. Vilém Skarolek

který/která studuje v **magisterském navazujícím studijním programu**

obor: **Stavba letadel (2301T039)**

Ředitel ústavu Vám v souladu se zákonem č.111/1998 o vysokých školách a se Studijním a zkušebním řádem VUT v Brně určuje následující téma diplomové práce:

Výpočetní studie možností využití aktivního řízení proudu k snížení intenzity koncových vírů na křídle

v anglickém jazyce:

A computational study on the effects of active flow control to the evolution of the wingtip vortices of a three dimensional wing

Stručná charakteristika problematiky úkolu:

Performing computational fluid dynamics simulations past a three dimensional wing with embedded blowing jet devices. Identifying positions of those devices onto the wing, which could make them more interactive with the wing tip vortices. Evaluating the jet-wingtip vortex interaction in terms of the drag and lift forces acting onto the wing. Demonstrating the optimum solution, which minimizes the drag and therefore the aircraft's fuel consumption.

Cíle diplomové práce:

Set-up of the computational model for wingtip blowing jets interaction with induced vortex. Basic optimization of positions of jets, number of jets, blowing parameters with respect to induced drag minimalization. Evaluation of possible fuel savings for selected aircarft.

Seznam odborné literatury:

[1] P. Margaris, I. Gursul, Vortex topology of wing tip blowing, Aerospace Science and Technology, 2010.
[2] P. Margaris, I. Gursul, Wing tip vortex control using synthetic jets, Aero. J. 110 (1112) (2006) 673–683.
[3] R.E. Mineck, Study of the potential aerodynamic benefits from span-wise blowing at wingtip, NASA TP-3515, 1995.
[4] D.A. Tavella, N.J. Wood, C.S. Lee, L. Roberts, Lift modulation with lateral wingtip blowing, J. Aircraft 25 (4) (1988) 311–316
[5] John Anderson, Computational Fluid Dynamics, 1995.

Vedoucí diplomové práce: Ing. Stavros Karampelas, Ph.D.

Termín odevzdání diplomové práce je stanoven časovým plánem akademického roku 2011/2012.

V Brně, dne 21.11.2011

L.S.

doc. Ing. Jaroslav Juračka, Ph.D.
Ředitel ústavu

prof. RNDr. Miroslav Doupovec, CSc., dr. h. c.
Děkan fakulty

Abstract:

In the present thesis, series of RANS calculations of the flow past a NACA 0015 wing at different angles of attack with active flow control have been performed. Active flow control configurations are applied on the wing's surface at a Mach number of $M = 0.21$ and $Re = 2.5 \times 10^6$. Several types and placements are examined in order to find the most powerful control configuration and energy efficient. The proposed concept in this study does not follow the conventional active control methods past wings. Large blowing surfaces and low velocity magnitudes at the slots' exits are considered and the energy efficiency is examined for a number of variants. Strategies for drag reduction and lift increase of the wing are demonstrated thoroughly by varying some of the actuation parameters. The active control when operating under some specific conditions could reach very high energy efficiency ratios at all angles of attack, while in the same time could be able to reduce significantly the total drag of the wing, increase the total lift or combine effectively those favorable effects for better flight performance. Maximum drag decrease could exceed 40% of the total drag at low angles of attack, with still positive energy income.

KEYWORDS:

active flow control; jets; wingtip vortex; high Reynolds; blowing; drag reduction

ABSTRAKT:

V této diplomové práci byla provedena série numerických výpočtů proudění kolem křídla s aktivním řízením proudu. Výpočty jsou provedeny pro různé úhly náběhu křídla s profilem NACA 0015. Křídlo s zařízením pro aktivní řízení proudu bylo testováno v podmínkách s Machovým číslem $M = 0,21$ a $Re = 2,5 \times 10^6$. Bylo zkoušeno více možných konfigurací s cílem nalézt nejúčinější variantu, která bude zároveň stále energeticky efektivní. Vybraný přístup k aplikaci aktivního řízení na křídle se od ostatních liší. Použito je velkých ploch pro vyfukování vzduchu o nízké rychlosti a zároveň v souvislosti s tím je studována energetická účinnost. Snížení odporu a zvýšení vztlaku je dosaženo změnou řídících veličin. Při určitých specifických podmínkách je zařízení schopno při velmi vysoké energetické účinnosti dosáhnout pro všechny úhly náběhu výrazného snížení odporu, zvýšení vztlaku křídla, nebo obojího zároveň. Maximální pokles odporu křídla na malých úhlech náběhu přesahuje 40% z celkového odporu křídla a stále s dodržením energetické účinnosti.

KLÍČOVÁ SLOVA:

aktivní řízení proudu; trysky; koncový vír; vysoké Reynoldsovo číslo; vyfukování; snížení odporu

SKAROLEK,V. *A computational study on the effects of active flow control to the evolution of the wingtip vortices of a three dimensional wing.* Brno: Brno University of Technology, Faculty of mechanical engineering, Institute of aerospace engineering, 2012. 92 p. Supervisor Ing. Stavros Karampelas, Ph.D.

SKAROLEK,V. *Výpočetní studie možností využití aktivního řízení proudu k snížení intenzity koncových vírů na křídle.* Brno: Vysoké učení technické v Brně, Fakulta strojního inženýrství, Letecký ústav, 2012. 92 s. Vedoucí diplomové práce Ing. Stavros Karampelas, Ph.D.

DECLARATION

I declare that I have prepared this dissertation independently, under the supervision of the master's thesis supervisor. I have used no sources other than those quoted and the literature I have used has been clearly cited in the text.

Brno, 22/05/2012 . . . .

(author's signature)

ACKNOWLEDGEMENT

I would like to express my sincere gratitude to my supervisor Ing. Stavros Karampelas, Ph.D. I would like to thank him specially for his great support, encouragement and guidance during this work. I would finally like to thank my family and friends for their support during my studies.

Brno, 22/05/2012 . . . .

(author's signature)

Contents

List of Figures

List of symbols:

α	$[^\circ]$	Angle of attack
λ, A	$[1]$	Aspect ratio
η	$[1]$	Propeller efficiency
η	$[1]$	Effectiveness ratio
Φ	$[1]$	Flow variable
Γ	$[m^2/s]$	Circulation
ω	$[1/s]$	Vorticity
μ	$[kg/ms]$	Dynamic viscosity
ν	$[m^2/s]$	Kinematic viscosity
τ	$[1]$	Reynolds stresses
ρ	$[kg/m^3]$	Density
L	$[N]$	Lift force
D, F_x	$[N]$	Drag force
D_i	$[N]$	Induced drag
T	$[N]$	Thrust
P	$[W]$	Power
C_L	$[1]$	Lift coefficient
C_D	$[1]$	Drag coefficient
C_{Di}	$[1]$	Induced drag coefficient
C_{D0}	$[1]$	Zero-lift drag coefficient
C_m	$[1]$	Pitching moment coefficient
C_p	$[1]$	Pressure coefficient
C_μ	$[1]$	Momentum coefficient
C_{LKmax}	$[1]$	Lift coefficient at K_{max}
C_{DKmax}	$[1]$	Drag coefficient at K_{max}
C_{L1}	$[1]$	Lift coefficient at at current speed
C_{LK}	$[1]$	Lift coefficient at speed of K_{max}
ΔC_L	$[\%]$	percentage change
ΔC_D	$[\%]$	percentage change

x	$[m]$	x-coordinate
y	$[m]$	y-coordinate
z	$[m]$	z-coordinate
u	$[m/s]$	x-axis velocity component
v	$[m/s]$	y-axis velocity component
w	$[m/s]$	z-axis velocity component
V	$[m/s]$	Fluid velocity
e	$[1]$	Oswald’s efficiency factor
K_{max}	$[1]$	Max. lift-drag ratio
V_{Global}	$[1]$	Global velocity ratio
V_{Local}	$[1]$	Local velocity ratio
V_{mD}	$[m/s]$	Minimum drag speed
V_{max}	$[m/s]$	Maximum horizontal speed
V_{S1}	$[m/s]$	Stall speed without flaps
V_{S0}	$[m/s]$	Stall speed with flaps
u_{bl}	$[m/s]$	Blowing velocity
A_{bl}	$[m^2]$	Surface area of the blowing slot
S	$[m^2]$	Surface area of the wing
S	$[m^2]$	Surface of the slice
b	$[m]$	Span length
$b/2$	$[m]$	Semispan length
C	$[m]$	Curve length
c	$[m]$	Chord length
L	$[m]$	Length
W	$[m]$	Width
H	$[m]$	Height
H	$[m]$	Height of flight
R	$[km]$	Range
m_{fuel}	$[kg]$	Fuel capacity
m_{Tow}	$[kg]$	Max. take-off weight
K	$[1]$	Factor of blowing losses
$y+$	$[1]$	Wall y plus

Subscripts:

$\overline{u_i}$	mean component
$u^{'}$	fluctuating component
∞	freestream
bl_{upper}	blowing from the upper surface
bl_{bottom}	blowing from the bottom surface
w	wing
re	required
av	available
sh	shaft

Abbreviations:

AFC	Active flow control
CPU	Central process unit
CFD	Computational fluid dynamics
DES	Detached eddy simulation
DNS	Direct numerical simulation
FDM	Finite difference method
FEM	Finite element method
FVM	Finite volume method
RANS	Reynold averaged Navier-Stokes
RE	Reynold’s number
S-A	Spallart-Allmaras

1 Introduction

Modern aircraft development has become more attentive in financial and environmental requirements, thus attaining the lowest possible fuel consumption and noise levels is necessary. From aerodynamic point of view, one possible area for improvement is reduction of the induced drag, which is caused by the formation of the tip vortex. Induced drag at high speeds (cruising flight) constitutes about 30 % [39] of the total drag. However, at lower speeds (takeoff or landing), induced drag accounts for up to 50 % [39] of the total drag, thus its reducing is favourable in operating costs. Corresponding fuel savings would lead to reduced environmental impact.

Trailing vortex is also a source of wake vortex problem and causes higher level of noise. The wake vortex is formed from the tip vortices. Tip vortices caused by large airplanes can be powerful enough to cause light airplanes following too closely to go out of control. This is one reason for mandatory spacings between aircrafts during take off or landing at airports.

1.1 Methods for induced drag reduction

The true understanding of finite-wing did not come until 1907. In that year, Frederick W. Lancester published his book titled “Aerodynamics” [17]. In this book it is possible to find the first mention of vortices that trail downstream of the wing tips. In the past, several principles have been used to reduce harmful effects of the trail vortices. It is well known that the value of the induced drag strongly depends upon the aspect ratio of the wing. [1] Another options could be the reshaping of the tip [12], [13], the use of winglets [35] or non-planar wings concepts [16]. Concept of the winglets was established in 1897. In that year, Frederick W. Lanchester patented endplate concept. More thorough research of winglet concept was performed by researcher Richard T. Whitcomb in 1970s, who led the foundations in this field. Mentioned devices are passive means of flow control and they are truly effective only in one selected flight condition, therefore active means of flow control started to become imperative. The basic principle of active flow control is the possibility to adapt the control operating conditions when the flight mode is changed. Configurations employing active control devices allow adjustments to be made as the flight condition changes. For instance wingtip blowing device makes adjustments regarding the blowing intensity. The progress in the system integration, miniaturization, actuators, sensors and computational techniques enables their possible utilization in the future. At this stage,

---

[1] the wing with two time longer span has 1/4 of induced drag in comparison to the wing with one span long.

comprehensive experiments are required to bridge the gaps between theory, computations, and real-world applications.

1.2 Overview of resources

Various experimental studies involving wind-tunnels measurements and full-scale flight testing have been conducted to clarify the trailing vortex phenomenon in the 1970s [23], [10], [26]. A more recent comprehensive experimental study was performed by McAlister and Takahashi [20] in 1991. At the same time in the 1970s, there has been put an effort on finding means to weaken the hazard associated with the wake [2], [4].

Active flow control by blowing or suction near the wing tip is possible to divide into three main groups: for the drag reduction, for the wake vortex diffusion or for the reduction of aerodynamically generated noise. Blowing has been used very often in recent studies by researchers. Suction, probably due to its higher complexity has not been investigated so frequently. The AFC device can be constituted by one continuous sheet or by several smaller, discrete jets. In former case, the slots with larger dimensions cover larger area and lower speeds of blowing are used. They are called “high aspect ratio” jets. The latter option needs to be sufficient in terms of the flow momentum,which is secured by high speeds of blowing (see figure 1.1). Another classification could be that blowing might be continuous or pulsing. Pulsed blowing could be also towards different directions in time.

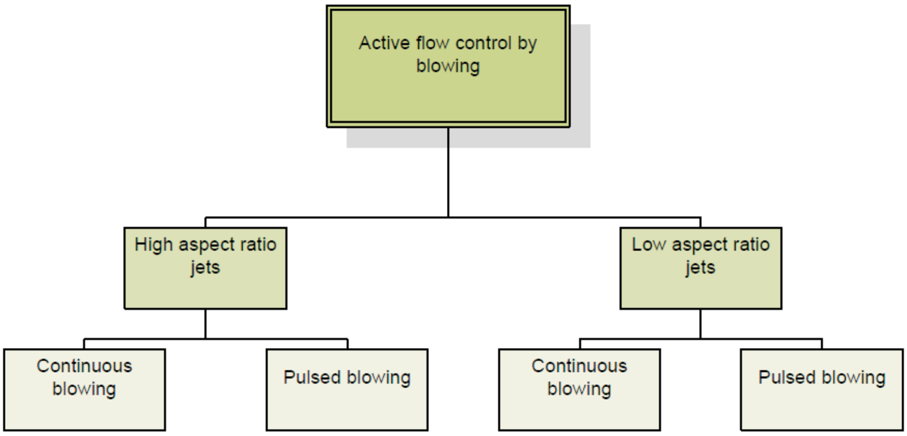

Figure 1.1: Active flow control.

Experimental investigations have been carried out to study the effects of axial wing-tip blowing [7]. Numerical study of a wing with axial wing-tip blowing has been solved by Lim [18]. Conclusions of those studies revealed that the axial wing tip blowing has an effect on the flowfield only in the near downstream region. It has been found that axial blowing has marginal effect on the increase of lift. Dunham [7] classified the axial wing-tip blowing as an unsuccessful concept for aircraft wake vortex decay.

Spanwise wing-tip blowing has been also investigated by many researchers. One approach was the use of spanwise blowing to increase the effective span by implementing high aspect ratio jets [31]. Alternative approach was the use of low aspect ratio jets in order to affect the flowfield instead of extending the span. Analytical and experimental studies using spanwise blowing at the tip of a moderate-aspect-ratio swept wing is performed by Mineck [21]. It is found that blowing from jets with short length have a little effect on lift and drag, but blowing from longer jets simultaneously increased lift and reduced drag. The jets which are placed at the rear part of the wingtip give higher drag reduction than the jets at the front. Energy consumed by the jet flow is typically greater than the energy savings coming from the wing drag reduction. This fact combined to the small increase of lift showed that the spanwise blowing at the wingtip does not appear to be a practical mean of improving the aerodynamic efficiency of wings.

Coimbra and Catalano [3] have performed wind tunnel measurements of system consisting of three independent "Coanda" jets. Those jets can be vectored in different directions (see figure 1.2). It is found that the jets at the rear part of the chord are more effective in lift enhancement. The drag polar diagram revealed large improvement for all jets especially at high incidences.

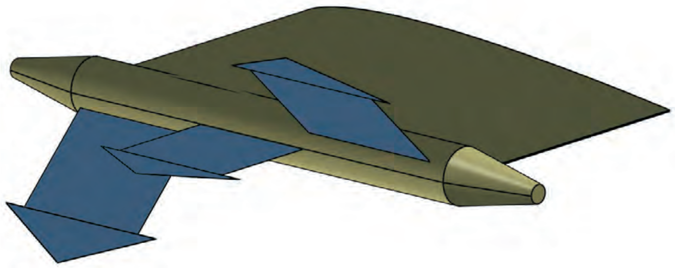

Figure 1.2: Coanda jets [3].

Margaris and Gursul [19] have published an extensive parametric study in order to examine the effect of continuous blowing from high aspect ratio jets on the tip vortex in the near wake (see figure 1.3). Different vertical and longitudinal positions are examined. Blowing from the slot 1 showed two diffused visible trailing vortices. In comparison with slot 1, it is observed that the slot 2 produces trailing vortices with higher degree of diffusion. In the case of the rear slot, lower maximum cross flow velocity and lower vorticity has been found compared with the front positioned slot. The case with slot 3 have visible single diffused trailing vortex and the case with slot 4 showed no visible change in comparison with blowing-off case. Effect on the induced drag reduction is not examined, but it is mentioned that the examined configurations are energy inefficient. Spanwise blowing has been studied also as a mean of changing the vortex position on one side of the wing, thus producing a rolling moment through asymmetric wing lift [32] and [33].

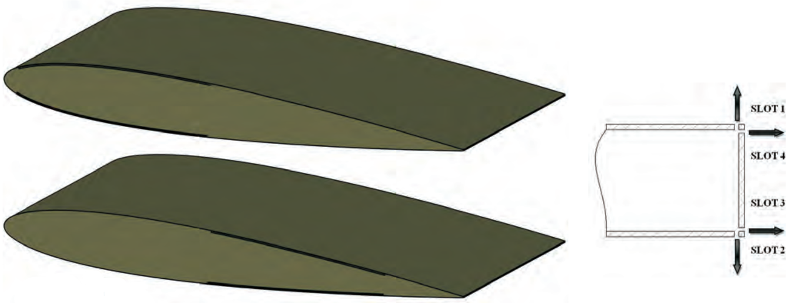

Figure 1.3: Slots and position used by Margaris et al. [19].

Some studies are also focused on pulse blowing. The use of pulsed span-wise air jets at the wing tip to perturb a single tip vortex in close proximity has been examined by Heyes and Smith [11]. Heyes and Smith introduced cyclic spatial perturbation in the trailing vortex trajectory using high aspect ratio jets (see figure 1.4). It was shown that blowing towards the tip vortex leads to an increase of its core radius and decrease in peak rotational velocities. This process diffuses and displaces the vortex. Promising effects on the induced drag are anticipated, nevertheless they are not examined.

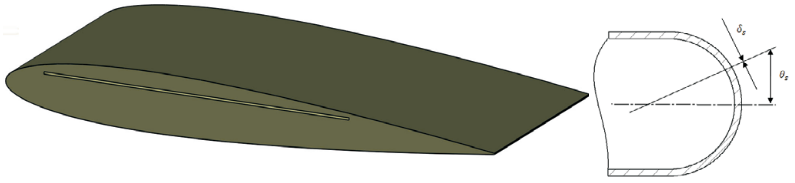

Figure 1.4: Set-up used by Heyes et al. [11].

Recently, pulsed blowing has been studied by Yadlin and Shmilovic [36]. It is shown that the vortex instabilities generated at low or high frequencies lead to the vortex disintegration. Several trajectories used in the aforementioned study are shown in fig.1.5.

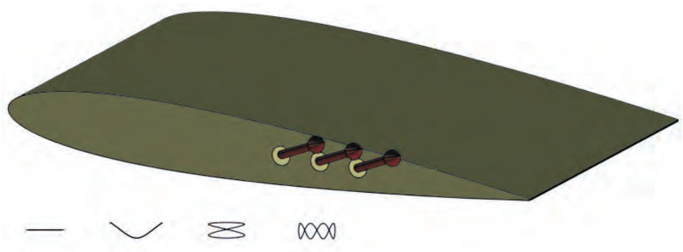

Figure 1.5: Pulsed wing tip blowing [36].

Wingtip blowing has been studied also as a mean of noise reduction. Lateral tip jet flow has been examined by Yang et al. [37]. Comprehensive numerical and experimental investigations of the tip vortex were performed and it was shown that the jet flow can effectively reduce aerodynamically generated noise by the vortex. The forward blowing was identified the most effective in terms of maximum vortex core. Downward blowing showed almost the same effect (see figure 1.6).

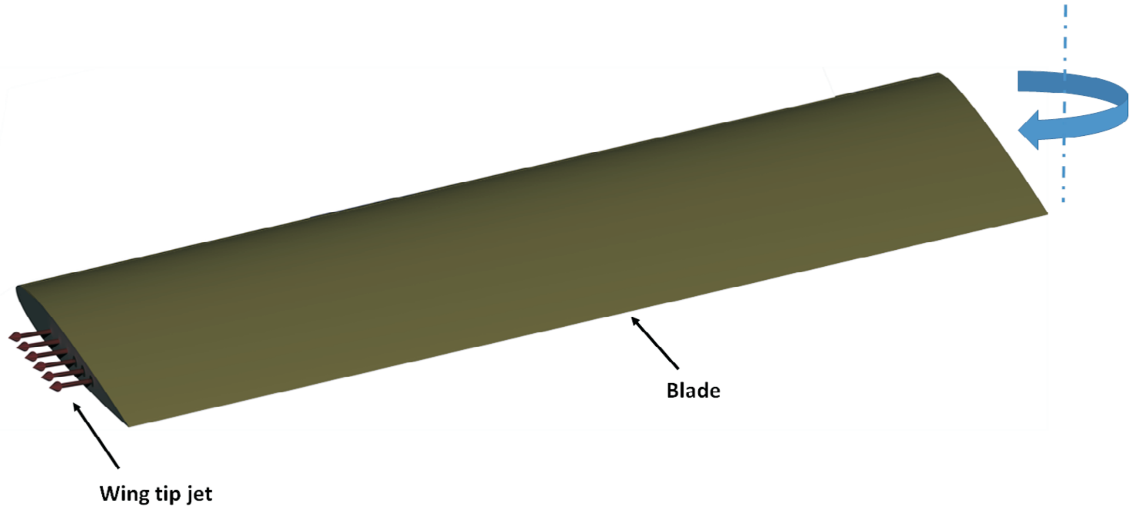

Figure 1.6: Diagram of wing-tip blowing jet of rotor [37].

1.3 Evaluation of research study

Based on the results of literature research it appears that the best position of the AFC device is close to the trailing edge. Also, it appears that the longer slot is more effective than the short one. In the present study, steady blowing is applied. Pulsed blowing could be effective but it is not examined.

1.4 Research outline and overview

Recently, many research studies were focused on affecting the trail vortex, which might lead to instability of the trail vortex. The vortex is diffused and its decay is higher and therefore hazardous wake behind a plane is weakened. However, there is a lack of research efforts focused on the reduction of drag and its relation with energy efficiency. Already tested wing tip devices exhibit low efficiency and despite some reduction in drag the gained benefits are insignificant. Main goal of this thesis is to introduce such a device that will be effective in energy balance.

Another important task is to reveal and describe mechanisms of functionality of proposed device, including the factors that influence its function. For instance, it is intensity of blowing, angle of blowing and position of the slots on the wing. The present research study is based on numerical computations (CFD) of the flow past the wing.

2 Theory and Methodology

Fluid mechanics is research area which investigates the physics of fluids at all flow regimes. Field of fluid mechanics is branched into fluid statics (fluids at rest), fluid kinematics (fluids in motion) and fluid dynamics (study of external forces on fluid in motion). Theoretical background is complex and simplification is often necessary. The needful assumptions are made in accordance with the principles of conservation of mass, conservation of energy and conservation of momentum. Fluids motion is governed by the “Navier-Stokes” equations. Those equations are derived from the basic principles of conservation of mass, momentum and energy. They were derived independently by G.G. Stokes (1819-1903) in England, and M. Navier (1785-1836) in France, in the early 1800’s. Those equations describe how the velocity, pressure, temperature, and density of moving fluid are related. The Navier–Stokes equations are nonlinear partial differential equations. Supplementary equations (conservation of mass) and well formulated boundary conditions are required. Due to its complexity it is not usually possible to get exact solution. In some cases, aproximations and simplifications of the equations can be implemented for the derivation of analytical solutions. The modern capacity of CPU offers the opportunity to solve the discretized version of the equations. A new area called CFD was arizen in the last decades and it is mainly related to the development of numerical algorithms to solve the fluid flow problems.

2.1 Structure of a CFD code

Modern CFD packages contain three main parts:

- pre-processor
- solver
- post-processor.

At the pre-processing stage, the modeling of the flow is being set-up and prepared for use by the solver. The region of interest is defined and the computational domain is subdivided into smaller non-overlapping sub-domains by process called a mesh generation. The accuracy of the computations strongly depends on the number of cells in the grid. In general, the larger the number of cells, the longer the necessary calculation time. This is the reason why meshes are often non-uniform. Finer in the regions where large variations occur and coarser in the regions with little change. Important step in the pre-processing stage is the consideration of the physical phenomena that need to be modeled and the definition of the appropriate boundary conditions. Solver performs an approximation of the unknown flow variables. Various discretization methods can be applied to the equations. Among those techniques belongs finite difference, finite volume, finite element, and spectral methods etc. Last step for solver is to perform solution of the algebraic equations. Post-processor allows to the user to process the results. It includes the domain and geometry display, vector plots, contour plots, particle tracking etc.

2.2 Incompressible Navier-Stokes equations

Governing flow equations used in the modern CFD codes are the Navier-Stokes equations. Simplified equations are obtained when considering an incompressible flow of a Newtonian fluid. Incompressible flow assumption is accurate for flow speeds lower than Mach number 0.3. Assumptions of incompressibility are that molecular viscosity is constant and the second viscosity effect

$$\lambda = 0. \tag{2.1}$$

Then the simplified continuity equation could be expressed as

$$\mathrm{div}\mathbf{u} = 0, \tag{2.2}$$

and x-momentum equation

$$\frac{\partial u}{\partial t} + u\frac{\partial u}{\partial x} + v\frac{\partial u}{\partial y} + w\frac{\partial u}{\partial z} = -\frac{1}{\rho}\frac{\partial p}{\partial x} + \nu\nabla^2 u + f \tag{2.3}$$

or, in compact vector form as follows:

$$\frac{\partial u}{\partial t} + \mathrm{div}(u\mathbf{u}) = -\frac{1}{\rho}\frac{\partial p}{\partial x} + \nu \text{ div grad } u + f \tag{2.4}$$

Symbols:
v-speed, p-pressure, t-time, ρ-density, ν-kinematic viscosity, f-body forces (often just gravitational acceleration)
the meaning of terms:
local acceleration + convective acceleration = acceleration caused by pressure gradient + acceleration for overcoming viscosity forces + acceleration caused by body forces

2.3 Discretization methods

2.3.1 Finite difference method

Finite difference method (FDM) replace the derivatives appearing in the differential equation by finite differences. The algebraic equation is obtained for the value Φ at each grid point. One possibility of approximating derivatives of Φ at a grid point is to fit function (polynomial) through that grid point and its neighbors and differentiate that function. The simplest method is piecewise linear function. The assumptions are that variable Φ varies linearly from node to node.
We obtain at the grid point identified by an index i:

$$\left(\frac{\partial \Phi}{\partial x}\right)_i \approx \frac{\Phi_i - \Phi_{i-1}}{x_i - x_{i-1}}, \tag{2.5}$$

which is called backward differencing scheme, or:

$$\left(\frac{\partial \Phi}{\partial x}\right)_i \approx \frac{\Phi_{i+1} - \Phi_i}{x_{i+1} - x_i}, \tag{2.6}$$

which is called forward differencing scheme.
Using schemes mentioned above leads to inaccurate results for nonlinear variation of Φ. Assuming a parabolic profile passed through three points, the following scheme is obtained:

$$\left(\frac{\partial \Phi}{\partial x}\right)_i \approx \frac{\Phi_{i+1} - \Phi_{i-1}}{x_{i+1} - x_{i-1}}, \tag{2.7}$$

which is called central differencing scheme.

Another possibility is to use Taylor series expansion around Φ. FDM is a well-established and conceptually simple method, but for irregular geometries or an unusual specification of boundary conditions become difficult to use. Details and comprehensive description of the finite difference method can be found in literature [29] and [24].

2.3.2 Finite element method

The backgrounds of the finite element method was set in 1940's. It has been developed initially for structural stress analysis. The finite element discretization divides the region into a number of smaller elements (linear, triangles, quadrilaterals etc.) and gives a piecewise approximation to the governing equations.
The solution by the finite element method can be described as:

- Discretize the continuum (grid generation)
  Element shapes can be linear, triangles, quadrilaterals etc. Each element is formed by the connection of nodes.

- Shape functions (linear, polynomial basis functions etc.)
  Interpolation function represents the variation of the field variable over an element.

- Form the element equations - local matrices

- Assemble the element equations to the global matrix
  Resulting matrix represents the behaviour of the entire region of the problem.
  Boundary conditions are implemented in proper way into global matrix.

- Solve the system of equation
  Variety of matrix solution techniques can be used.

Important feature of the FEM is its ability to handle complicated geometries with relative ease. The quality of a FEM approximation is often higher than in the corresponding FDM approach. Details and comprehensive analytical description of the finite element method can be found in literature [38] and [1].

2.3.3 Finite volume method

The finite volume method (FVM) is similar to the finite difference method and was originally developed as a special finite difference formulation. It is widely used and thoroughly validated. FVM has some of the important features similar to the FEM method. One important feature is its clear physical interpretation. In the finite volume method, volume integrals in a partial differential equation that contain a divergence term are converted to surface integrals, using the divergence theorem. Those terms are then evaluated as fluxes at the surfaces of each finite volume. Control volume integration of the governing equations of fluid express balance of Φ over the control volume. It states clear relation between the numerical algorithm and physical conservation principle.
For flow variable Φ, for example a velocity component, is according to [34] possible to express balance as:

$$\begin{bmatrix} \text{Rate of change of } \phi \\ \text{in the control volume} \\ \text{with respect to time} \end{bmatrix} = \begin{bmatrix} \text{Net flux of } \phi \\ \text{due to convection into} \\ \text{the control volume} \end{bmatrix} + \begin{bmatrix} \text{Net flux of } \phi \\ \text{due to diffusion} \\ \text{into the control volume} \end{bmatrix} + \begin{bmatrix} \text{Net rate of creation} \\ \text{of } \phi \text{ inside the} \\ \text{control volume} \end{bmatrix}$$

The solution by the finite volume method can be described as:

- Discretization of the continuum (grid generation - control volumes)
- Integration of the governing equations over all control volumes
- Discretization - interpolation of the distribution of properties between nodal points to calculate fluxes at the control volume faces.
- Set up discretised equations at each nodal points
  Boundary conditions implementation in proper way to adjacent control volumes of the domain boundaries.
- Solve the system of algebraic equation
  Variety of matrix solution techniques can be used.

Important feature of the FVM is its consistency with mass, momentum and energy conservation. FVM can handle discontinuities in solutions and it provides an easy formulation for unstructured meshes. Also, there exist theory for convergence, accuracy and stability. Details and description of the finite volume method can be found in literature [34] and [24].

2.4 Turbulence modeling

The random nature of a turbulent flow prevents computations based on a deterministic description of the motion of all the fluid particles. Turbulence is a three-dimensional unsteady viscous phenomenon that occurs at high Reynolds number and it has the following properties:

- Irregularity and randomness
- Diffusivity
- Large Re
- Dissipation

  Although there was recently a massive progress in computational power of the modern computers, it is still impossible to resolve the time-dependent Navier-Stokes equations of turbulent flows at high Reynolds number and for smallest scales of the motion by Direct Numerical Simulation (DNS). Alternative methods are introduced where the small scale turbulent fluctuations are not directly simulated. For example, it is RANS-based turbulence modeling, Large eddy simulation (LES), Detached eddy simulation (DES) etc.

2.4.1 Reynolds Averaged Navier-Stokes equations

Reynolds Averaged Navier-Stokes equations (RANS) formulation is referred as the Reynolds decomposition form. This approach was presented by Reynolds in 1895. The approach is based on rewriting the terms in the equations as time-averaged and fluctuating. (see figure 2.1)

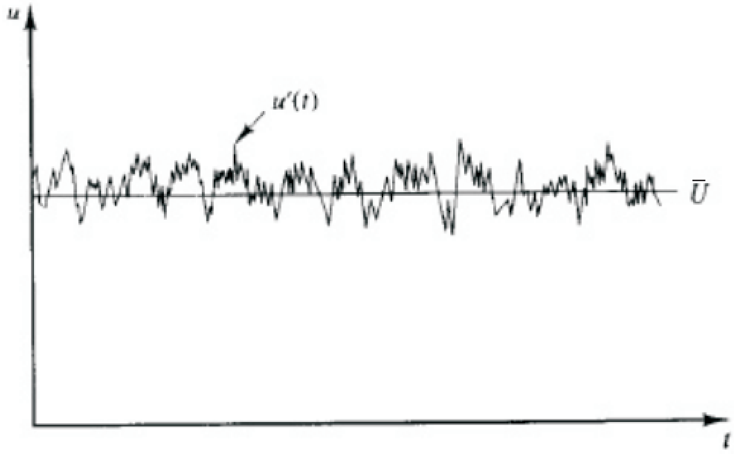

Figure 2.1: Typical point velocity measurement in turbulent flow [34].

The mean Φ of a flow property ϕ is defined as:

$$\Phi = \frac{1}{\Delta t}\int_{0}^{\Delta t} \phi(t)\, dt \tag{2.8}$$

For the velocity components:

$$u_i = \overline{u_i} + u^{'} \tag{2.9}$$

where $\overline{u_i}$ is mean component , $u^{'}$ is fluctuating component.

Likewise, for the others:

$$v_i = \overline{v_i} + v^{'} \tag{2.10}$$

$$w_i = \overline{w_i} + w^{'} \tag{2.11}$$

$$p_i = \overline{p_i} + p^{'} \tag{2.12}$$

Substituting expressions of this form for the flow variables into the continuity equation (2.2) and momentum equations (2.3) and taking the time average of each equation yield the Reynolds Averaged Navier-Stokes equations (RANS):

continuity equation :

$$\text{div}\,\overline{\mathbf{u}} = 0. \tag{2.13}$$

x-momentum equation:

$$\frac{\partial \overline{u}}{\partial t} + \text{div}\,(\overline{u}\,\overline{\mathbf{u}}) = -\frac{1}{\rho}\frac{\partial \overline{p}}{\partial x} + \nu\ \text{div grad}\ \overline{u} + \left[-\frac{\partial \overline{u'^2}}{\partial x} - \frac{\partial \overline{u'v'}}{\partial y} - \frac{\partial \overline{u'w'}}{\partial z}\right] + f \tag{2.14}$$

y-momentum equation:

$$\frac{\partial \overline{v}}{\partial t} + \text{div}\,(\overline{v}\,\overline{\mathbf{u}}) = -\frac{1}{\rho}\frac{\partial \overline{p}}{\partial y} + \nu\ \text{div grad}\ \overline{v} + \left[-\frac{\partial \overline{u'v'}}{\partial x} - \frac{\partial \overline{v'^2}}{\partial y} - \frac{\partial \overline{v'w'}}{\partial z}\right] + f \tag{2.15}$$

z-momentum equation:

$$\frac{\partial \overline{w}}{\partial t} + \text{div}\,(\overline{w}\,\overline{\mathbf{u}}) = -\frac{1}{\rho}\frac{\partial \overline{p}}{\partial z} + \nu\ \text{div grad}\ \overline{w} + \left[-\frac{\partial \overline{u'w'}}{\partial x} - \frac{\partial \overline{v'w'}}{\partial y} - \frac{\partial \overline{w'^2}}{\partial z}\right] + f \tag{2.16}$$

Variables now represent time-averaged values. Additional terms represent the effects of turbulence. Those extra terms are called the Reynolds stresses:

$$\tau_{xx} = -\rho\overline{u'^2} \tag{2.17}$$

$$\tau_{yy} = -\rho\overline{v'^2} \tag{2.18}$$

$$\tau_{zz} = -\rho\overline{w'^2} \tag{2.19}$$

$$\tau_{xy} = \tau_{yx} = -\rho\overline{u'v'} \tag{2.20}$$

$$\tau_{xz} = \tau_{zx} = -\rho\overline{u'w'} \tag{2.21}$$

$$\tau_{yz} = \tau_{zy} = -\rho\overline{v'w'} \tag{2.22}$$

As we obtained additional unknowns, the Reynold stresses, it is necessary to model it in appropriate way in order to close equation 2.14, 2.15 and 2.16. This requires use of turbulence models such as k-ε, k-ω, Spalart-Allmaras etc. Further information regarding RANS could be found in [34] and [25].

2.4.2 Turbulence model Spalart-Allmaras

Spalart and Allmaras described one equation model in 1994. The Spalart-Allmaras turbulence model (S-A) was developed and successfully validated for aerodynamic applications, such as flow over airfoils. This turbulence model was derived using empirical relationships, dimensional analysis. The S-A turbulence model solve a single transport equation for the kinematic turbulent viscosity ν_t. It is relative simple one equation turbulence model and it is well known that for some specific flows it is not very accurate. For example it is incapable to predict the decay of homogeneous, isotropic turbulence or it has inability to rapidly accommodate changes in length scale. The Spalart-Allmaras turbulence model proved good accuracy for attached boundary layers and flows with mild separation.

Transport equation for $\bar{\nu}$:

$$\frac{\partial\tilde{\nu}}{\partial t} + \tilde{u}_j \frac{\partial\tilde{\nu}}{\partial x_j} = \overbrace{c_{b1}\tilde{S}\tilde{\nu}}^{Production} + \underbrace{\frac{1}{\sigma}\left[\frac{\partial}{\partial x_j}\left((\nu+\tilde{\nu})\frac{\partial\tilde{\nu}}{\partial x_j}\right) + c_{b2}\frac{\partial\tilde{\nu}}{\partial x_j}\frac{\partial\tilde{\nu}}{\partial x_j}\right]}_{Diffusion} - \overbrace{c_{w1} f_w \left(\frac{\tilde{\nu}}{d}\right)^2}^{Destruction} \tag{2.23}$$

Kinematic turbulent viscosity ν_T:

$$\nu_T = \tilde{\nu} f_{v1}, \tag{2.24}$$

where f_{v1} is given by

$$f_{v1} = \frac{\chi^3}{\chi^3 + {C_{v1}}^3}, \tag{2.25}$$

and

$$\chi = \frac{\tilde{\nu}}{\nu}, \tag{2.26}$$

Turbulent production:

$$G_\nu = C_{b1}\rho\tilde{S}\tilde{\nu}, \tag{2.27}$$

and

$$f_{v2} = 1 - \frac{\chi}{1 + \chi f_{v1}}, \tag{2.28}$$

where S is based on the magnitude of the vorticity:

$$S = \sqrt{2\Omega_{ij}\Omega_{ij}}, \tag{2.29}$$

and Ω_{ij} is the mean rate of rotation tensor:

$$\Omega_{ij} = \frac{1}{2}\left(\frac{\partial u_i}{\partial x_j} - \frac{\partial u_j}{\partial x_i}\right) \tag{2.30}$$

.

Turbulent destruction:

$$Y_\nu = C_{w1}\rho f_w \left(\frac{\tilde{\nu}}{d}\right)^2, \tag{2.31}$$

where

$$f_w = g\left[\frac{1+{C_{w3}}^6}{g^6+{C_{w3}}^6}\right]^{1/6}, \tag{2.32}$$

$$g = r + C_{w2}\left(r^6 - r\right), \tag{2.33}$$

$$r = \frac{\tilde{\nu}}{\tilde{S}\kappa^2 d^2}. \tag{2.34}$$

Model constants:

$$C_{b1} = 0.1355, C_{b2} = 0.622, \sigma_\nu = \frac{2}{3}, C_{v1} = 7.1 \tag{2.35}$$

$$C_{w1} = \frac{C_{b1}}{\kappa^2} + \frac{(1+C_{b2})}{\sigma_\nu}, C_{w2} = 0.3, C_{w3} = 2.0, \kappa = 0.4187 \tag{2.36}$$

Further information regarding S-A could be found in [30] and [40].

3 Set-up and code validation

Simulations in the present thesis are performed with licensed software at our department. A geometric model of the domain is created in Catia V5 from Dassault Systemes. Grid generation is done in ANSYS ICEM CFD mesh generation software and computations are performed within the framework of the commercial flow solver ANSYS FLUENT 12.1 from Ansys, Inc.

3.1 Limits and boundary

Limits are defined by accessible hardware and software for this research study. Simulations are performed on a modern personal computer. Maximum number of cells should not be more than 3 millions. Regarding the maximum number of cells, the finer mesh is constructed in the field of interest (close to the wing and close to the wingtip). Due to the coarseness of the mesh at some distance behind the wing, it is possible to capture accurately the vortex decay only close to the wing section. Simulation is based on the steady-state approach and there is inability to catch the vortex wandering. Error in the measured core radii and peak tangential velocity might be expected.

3.2 Computational grid

Dimensions of the wing are derived from the experimental study performed by McAlister and Takahashi [20]. Further informations about this experimental study will be discussed in section 3.5. The wing with NACA 0015 profile has chord's length c=0.52 m and semispan (b/2= 1.7 m). The examined wing has aspect ratio $AR = 6.6$. The wing is rectangular and it has untwisted NACA 0015 profile along the entire span. The Reynolds number of the flow based on the wing's chord is 2.5 x 10^6. The computational domain is created as a rectangular wind tunnel test section. Its length is 5 chord lengths upstream the wing and 10 chord lengths downstream. The test section is 7.5 chord lengths wide and around 5 chord lengths high. That gives a test section with the outer dimensions LxWxH=7.8 m x 3.96 m x 2.64 m. The origin of the coordinate system is located in the middle of height of the trailing edge at the wing tip (see fig. 3.1). The computational domain can be seen in figure 3.2.

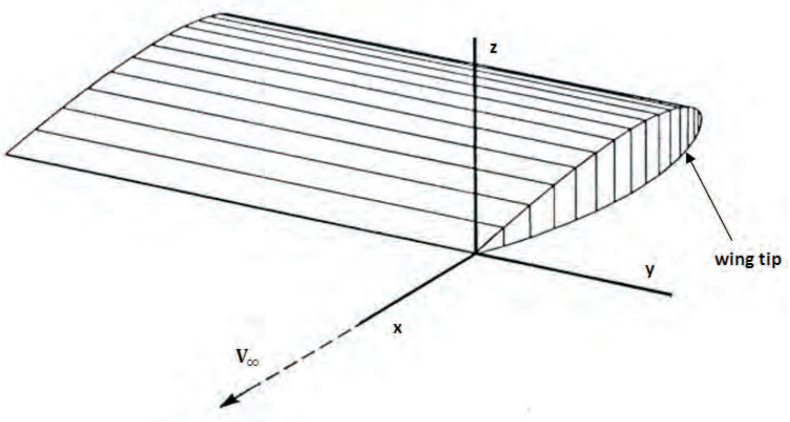

Figure 3.1: Origin and axis system.

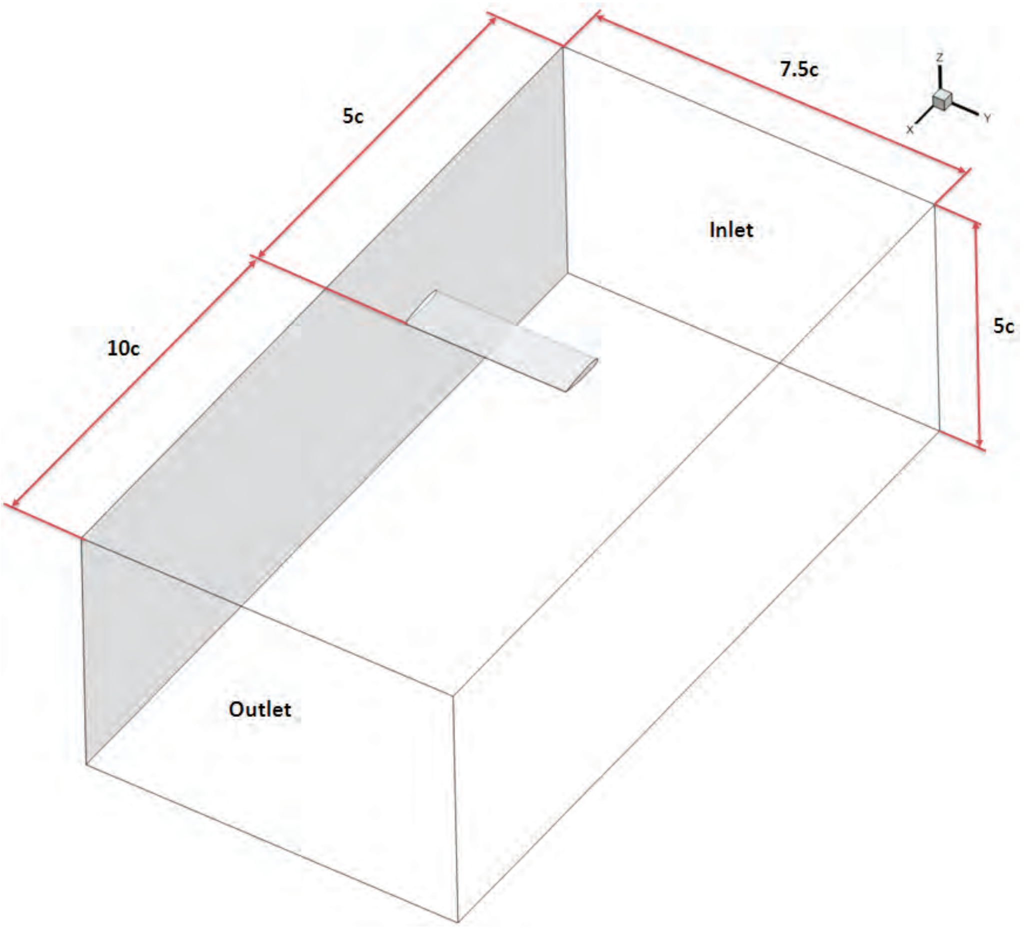

Figure 3.2: Dimension of the computational domain.

3.3 Grid generation

Grid generation is performed in ANSYS ICEM CFD mesh generation software. Grid generation process is processed as follows:

- Import of the model from CATIA V5 in STEP file format
- Preparation of the model, assignment of the names to the surfaces and curves
- Element size assignment to the surfaces
- Volume grid computation
- Checking and smoothing of the mesh
- Computation of the prismatic layers
- Checking and smoothing of the prismatic layers
- Final smoothing
- Final check
- Boundary conditions assignment
- Mesh export

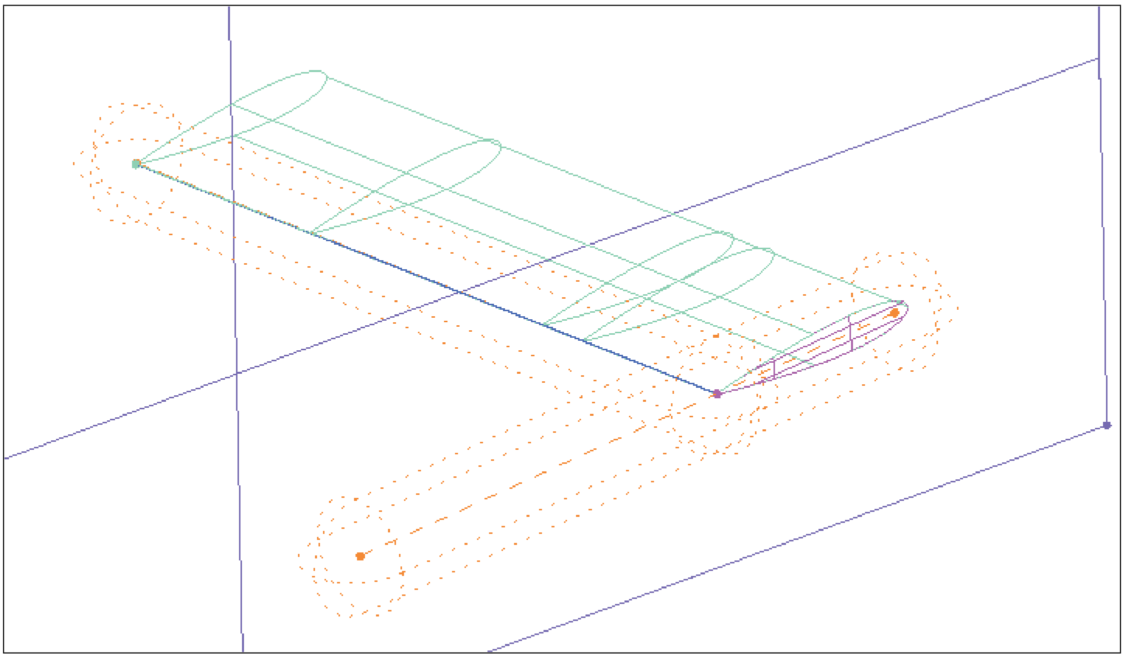

Figure 3.3: Side view of the refinement zones around the profile.

The topology of the mesh is unstructured and it contains tetrahedral elements. Due to the limited hardware resources, it was necessary to refine the mesh locally. The refinement zones are mainly situated around the regions where are expected high variations of the variables. It is close to the trailing edge and tip of the wing. The regions of the refinement can be seen in fig. 3.4 and 3.3. Close-up view of the mesh on the wing's surface can be seen in fig. 3.5.

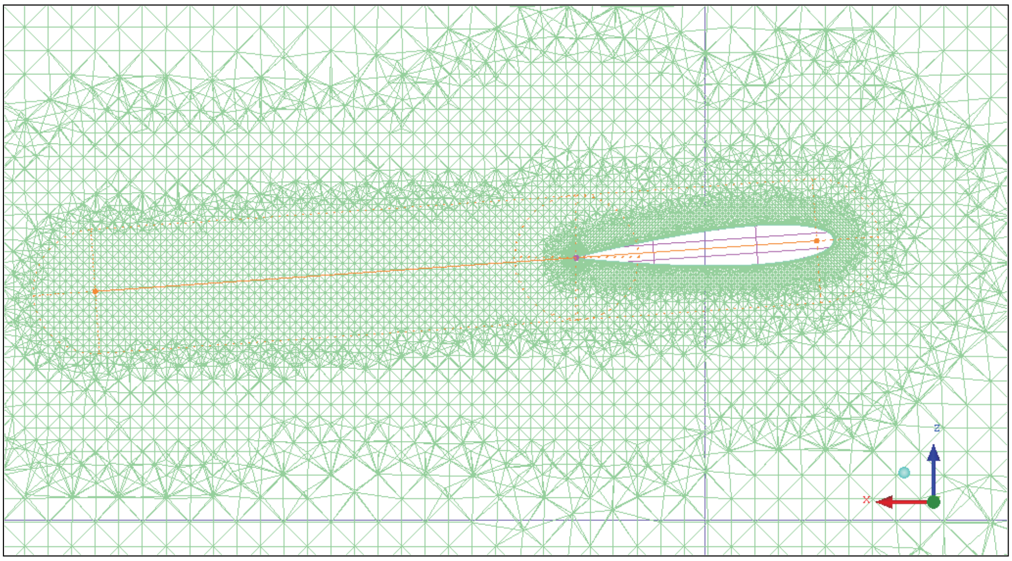

Figure 3.4: Refinement zones.

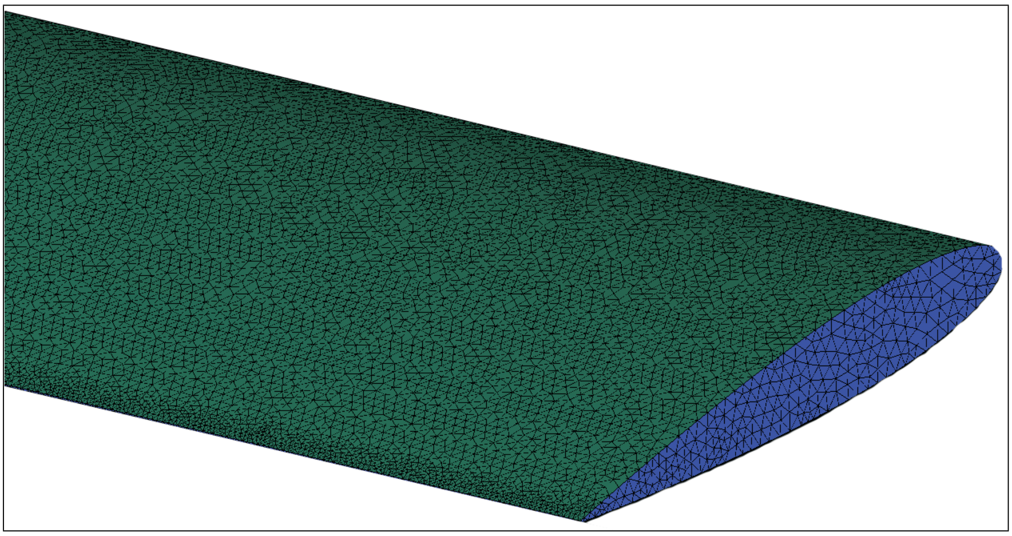

Figure 3.5: Close-up view of the mesh on the wing surface.

In order to successfully resolve the boundary layer region, the prismatic layers are implemented on the wing surface. Initial size of the first layer is 0.003 *mm*. The following layers are grown with a geometric growth rate of 1.5. Twelve layers are implemented on all surfaces along the wing. The prismatic layers can be seen in fig. 3.6.

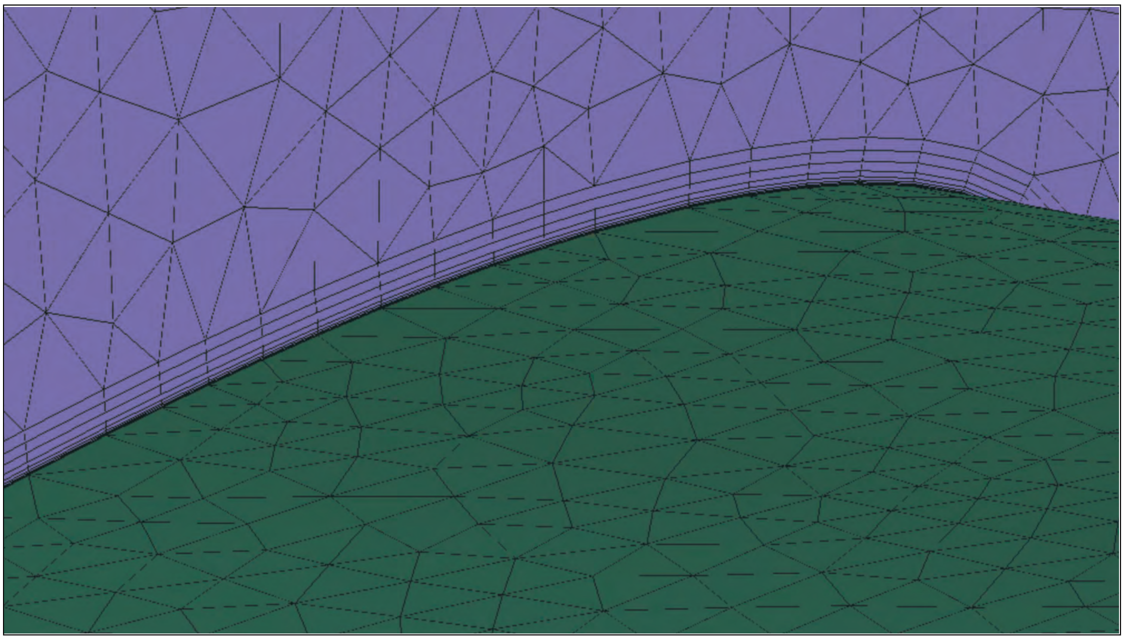

Figure 3.6: Detail of the prismatic layers.

The meshes were optimized not to exceed 2.5 million of cells. However to verify our results, another mesh is tested. It contains 5 million of cells and results could be found in section 3.6.

3.4 Solver set-up

Computational software used in this study is Fluent 12.1. All simulation runs have been solved using RANS methodology. Turbulence is computed by the Spallart-Almaras model. The viscosity-affected region is resolved by the near-wall modeling approach. However, it requires sufficient mesh resolution close to the wall and that's why prismatic layers are created. The solver is pressure based and the steady-state equations are solved. The pressure velocity coupling scheme is SIMPLEC. Turbulence model, as previously mentioned, is Spallart-Almaras one equation model. Flowing medium is air with density set to $\rho = 1.225 kg/m^3$ and dynamic viscosity $\mu = 1.7894x10^{-5} kg/ms$. Velocity inlet is set as an inlet with absolute flow velocity of 70 m/s normal to the boundary. An outlet is set as pressure outlet which is boundary condition with fix pressure. The boundary conditions on the side walls of the wind tunnel are "symmetry", which is boundary condition with normal gradient of variables set to zero. The top and bottom walls, as well as the wing surfaces are set as walls, which implements the no-slip condition. Since the flow velocity is 70 m/s, the flow can be assumed to be incompressible. The wing set at $\alpha = 12°$ showed that the flow exceed Mach number 0.3 only in a small region close to the leading edge. However, it is stated that assumption of the incompressibility could be used.

Tab1: Ansys Fluent 12.1 set up:

Solver	pressure-based	
Model	incompressible	
Time	steady approach	
Turbulence model	Spallart-Almaras	
Material	air	density $\rho = 1.225 kg/m^3$ dyn. viscosity $\mu = 1.7894x10^{-5} kg/ms$
Pressure-velocity	Simplec	
Inlet	velocity inlet	70 m/s
Outlet	pressure outlet	(condition with fixed pressure)
Side walls	symmetry	(gradients normal to the boundary are zero)
Top, bottom walls	wall	(no-slip condition)

3.5 Reference tunnel measurement

For the purpose of evaluation and comparison of the computed results, the settings and dimensions of the wing are derived from the experimental study performed by McAlister and Takahashi [20]. This report delivers a comprehensive set of experimental measurements. It is focused on NACA 0015 wing pressure and trailing vortex measurements. In a separate section of the study, a wake vortex analysis follows, which indicate the trajectory, the vortex size and the spatial circulation and vorticity evolution of the tip vortex. In this study three wings were tested with the same aspect ratio 6.6 and with chord lengths of 12.0, 16.2 and 20.4 inches ($\sim$ 0.3 m, 0.41 m, 0.52 m). The experiment was performed in the NASA Ames 7-by 10-Foot a closed-circuit subsonic wind tunnel with a maximum speed of 375 fps (114 m/s). Pressure and velocity measurements were conducted for angles of attack of $4^\circ \leq \alpha \leq 12^\circ$ and for Reynolds numbers of $1 \times 10^6 \leq Re \leq 3 \times 10^6$. An arrangement of the test area used by McAllister/Takahashi can be seen in fig. 3.7.

Figure 3.7: An arrangement of the test area.

3.6 Mesh independence

Maximum mesh size is limited due to the hardware limitations. The final mesh size is restricted not over exceed 2.2 millions of cells. In order to support the premise that the mesh size is sufficient, an other computational run is performed with finer mesh containing 4.9 millions of cells. Necessary computational time is 6 times higher. Comparison with experimental measurement or mesh which contains 2.2 million cells could be found in fig. 3.8 and 3.9. It is observed that at $\alpha = 4^\circ$ the drag prediction is worse in comparison to a domain with 2.2 million cells. Nevertheless, gain from the finer mesh is not significant and the computational time is too high. Based on this results, conclusion could be made that coarser mesh is sufficient. Lift and drag deviations could be seen in table 2.

Tab2: C_L, C_D deviations:

reference experiment	C_L		C_D			
CFD (mesh 4.9 millions)		C_L		C_D	ΔC_L	ΔC_D
$\alpha = 4^\circ$	0.325	0.346	0.009	0.022	$+6.46\%$	$+144\%$
$\alpha = 12^\circ$	1.037	0.953	0.061	0.061	-8.1%	$+0\%$

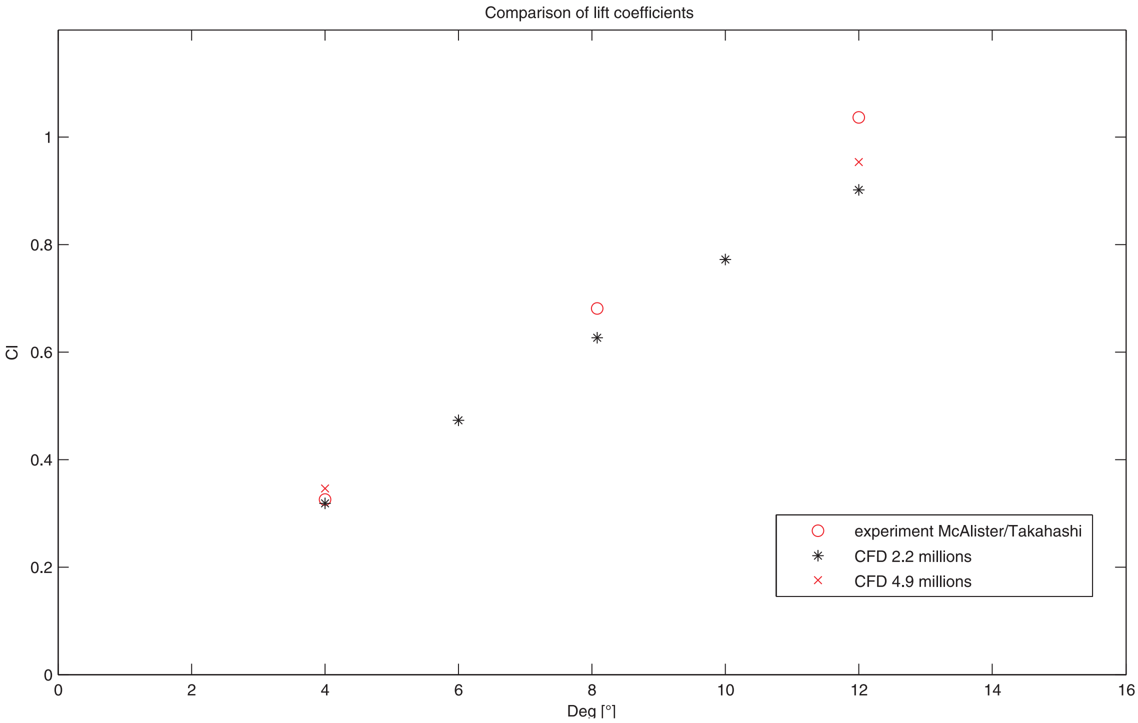

Figure 3.8: Comparison of lift coefficients.

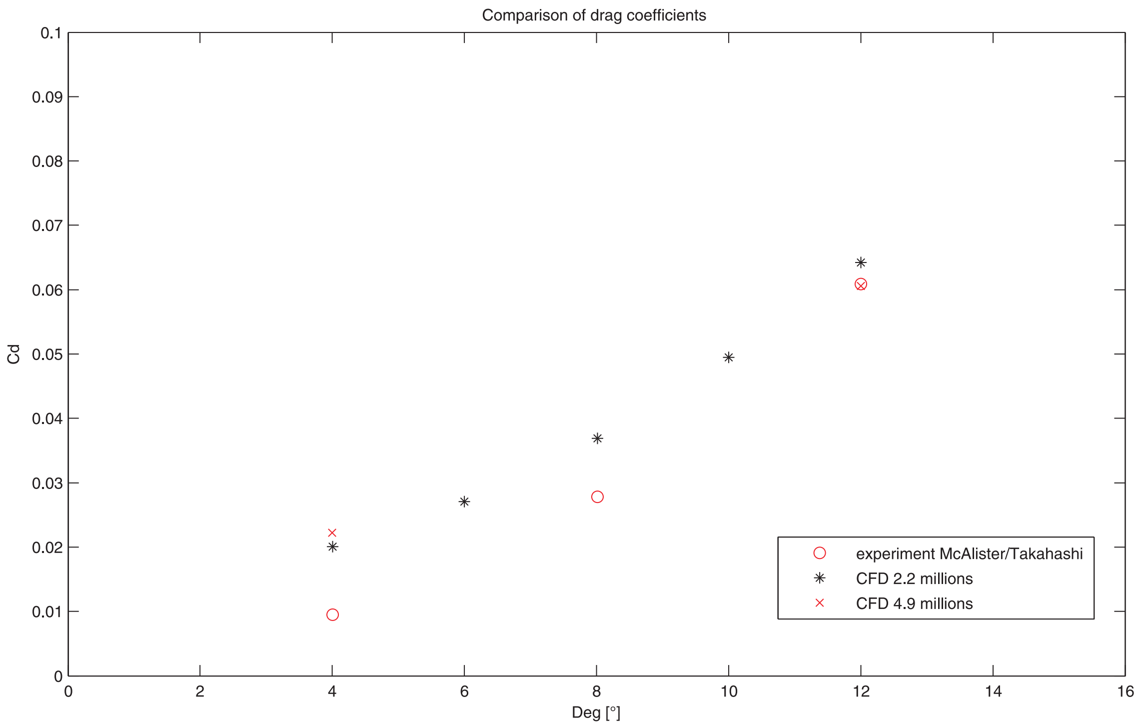

Figure 3.9: Comparison of drag coefficients.

Numerous experiments have shown that the near-wall region can be subdivided into three layers. Close to the wall is the viscous sub-layer where viscous damping reduce the tangential velocity fluctuations. After the viscous sub-layer comes the buffer layer and the fully turbulent log-law region. For the modeling of the turbulence is selected, so called, the near-wall model approach. This method is based on that strong gradients in the boundary layer are resolved with a very fine mesh. The other possible way would be to employ wall functions and resolve the region near the wall by using prescribed function (see fig. 3.10). In order to capture the laminar and transitional boundary layers correctly, the mesh must have the viscous length-scale values $y+$ approximately 1 for the near-wall model approach and $30 \leq y+ \leq 300$ for the wall functions. In any case, it is necessary to avoid to lie in the buffer region $5 \leq y+ \leq 30$ where both methods are not accurate. In the present study $y+ \sim 1$ is along the whole surfaces of the wing. It could be viewed in fig. 3.11.

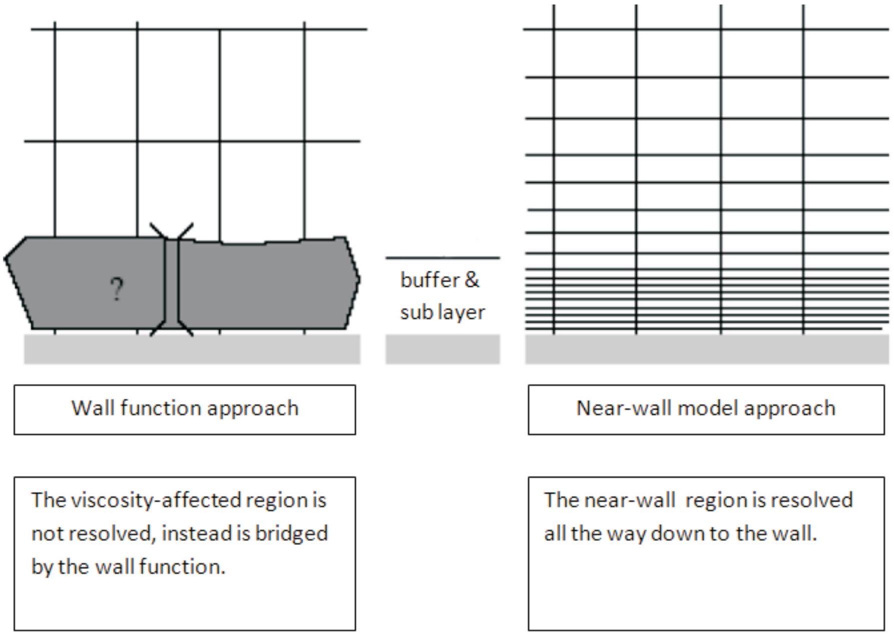

Figure 3.10: Different modeling approaches.

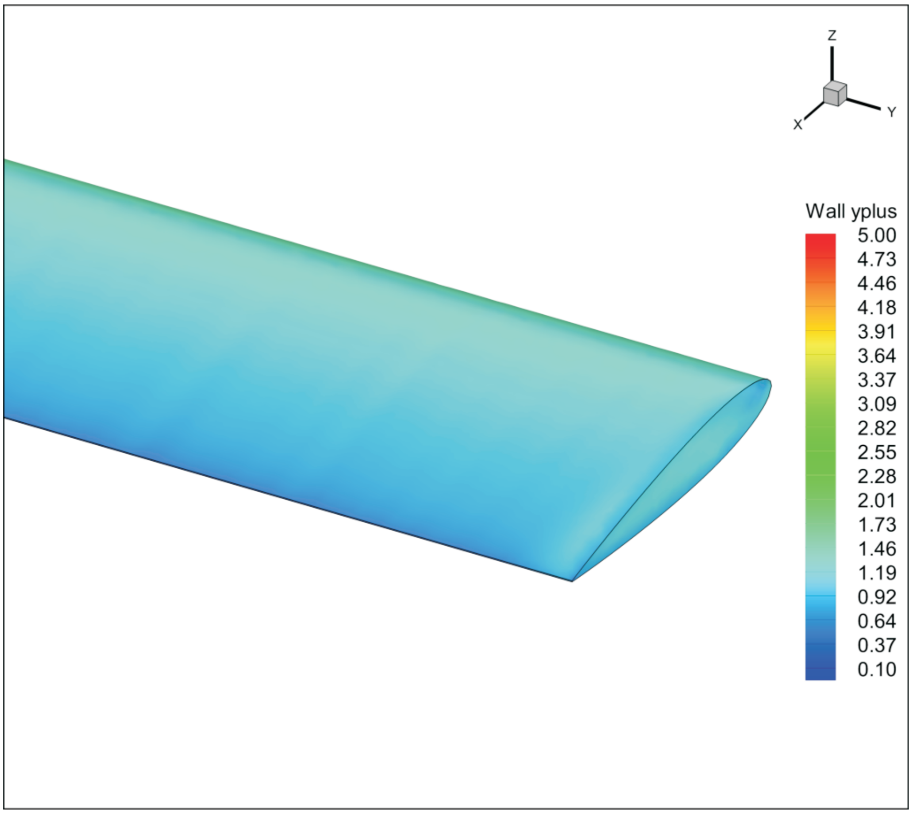

Figure 3.11: Contours of the wall $y+$ on the wing.

3.7 Code validation

It is a common practice in CFD to validate the code with experimental measurements. After successful validation, it is possible to proceed to further computations. Validation process is necessary because accuracy depends on the mesh topology, the chosen turbulent model, the operating conditions etc. The initial step is comparison of lift and drag at $\alpha = 4^\circ$, $\alpha = 8^\circ$ and $\alpha = 12^\circ$. Those reference values are derived from the detailed experimental study of McAllister/Takahashi as mentioned before. Lift converge quite well with deviations lower than 13%, as it could be seen in fig. 3.12. At lower angles of attack good agreement is reached. As the angle of attack is increasing, the discrepancy between measured and experimental values of lift is higher. Possible reasons for this disagreement, could be the local compressibility effects in the leading edge region, which has not been accounted for within the incompressible version of the present code. Also it was found that mesh resolution close to the leading edge is a little bit coarse. Effect of this lack will be discussed later in this chapter. In drag terms, the computations over-predict the axial force and results become to converge as the angle of attack increases (see fig. 3.13). As it was mentioned in the previous section, the one-equation turbulence model Spalart-Allmaras could not account for any transition effects and resolve the flow as fully turbulent from the upstream regions of the airfoil. However, at $\alpha = 12^\circ$ agreement of computation with measurement is satisfactory. At $\alpha = 4^\circ$ the drag is highly over predicted. Deviations in lift and drag could be seen in table 3. By testing other more complete models, such as the Shear Stress Transport Transition model, slight drag reductions are observed, but good agreements are reached only at $\alpha = 8^\circ$and $\alpha = 12^\circ$. However, those models are not implemented because they deviated more in lift terms.

Tab3: C_L, C_D deviations:

reference experiment	C_L		C_D			
CFD (mesh 2.2 millions)		C_L		C_D	ΔC_L	ΔC_D
$\alpha = 4^\circ$	0.325	0.318	0.009	0.020	-2.15%	$+122\%$
$\alpha = 8^\circ$	0.681	0.626	0.028	0.036	-8.07%	$+28.57\%$
$\alpha = 12^\circ$	1.037	0.902	0.061	0.064	-13.01%	$+4.91\%$

Pressure coefficients are compared at three span locations for three angles of attack. At all angles (4°, 8°, 12°) the agreement is quite good through the whole length of the wing's section apart from the leading edge area. Deviations in this region could be caused by coarse mesh. Amount of the elements on the surface is not enough to preserve smooth transition at radius of the leading edge. This leads to slight change of the profile shape. Consequently in all cases, the measured values of the suction pressures at the leading edge are higher in modulus to the computed ones, and this difference explains the deviation in the total lift. The pressure coefficients plots could be seen in figures from 3.14 to 3.22.

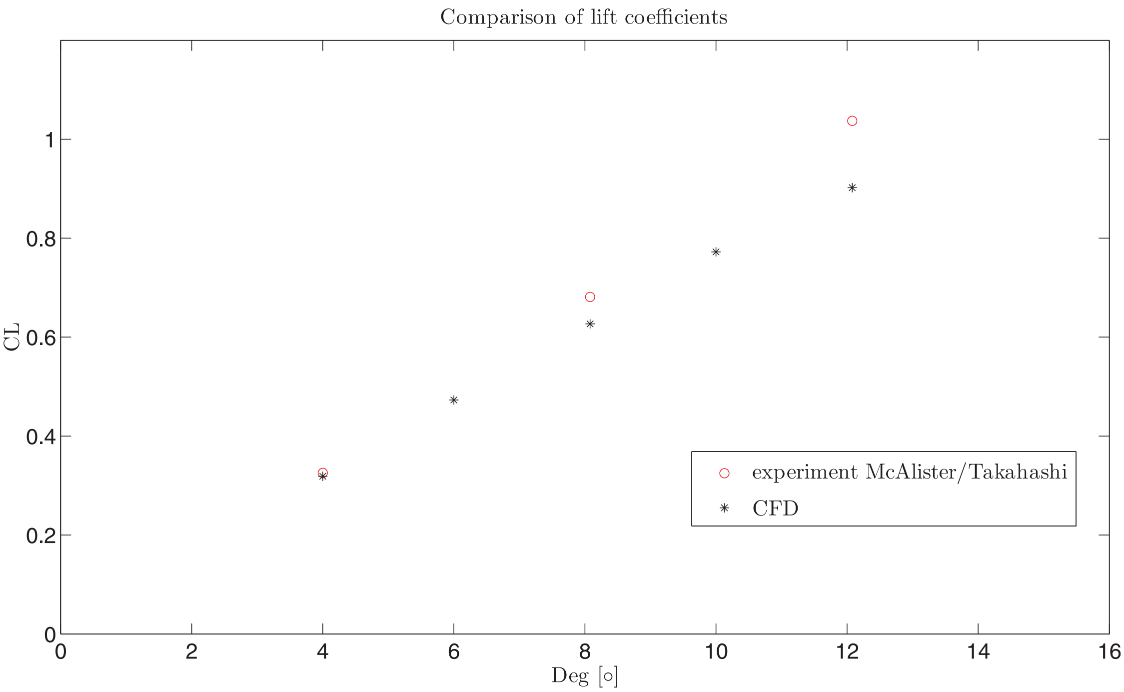

Figure 3.12: Comparison of lift coefficients.

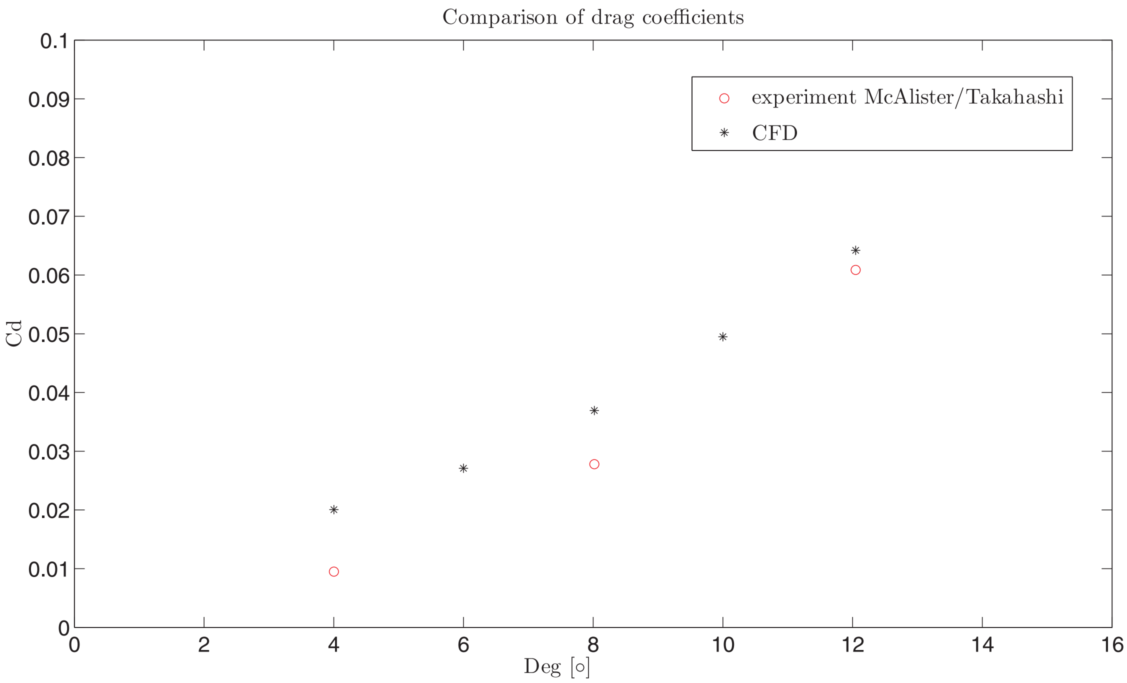

Figure 3.13: Comparison of drag coefficients.

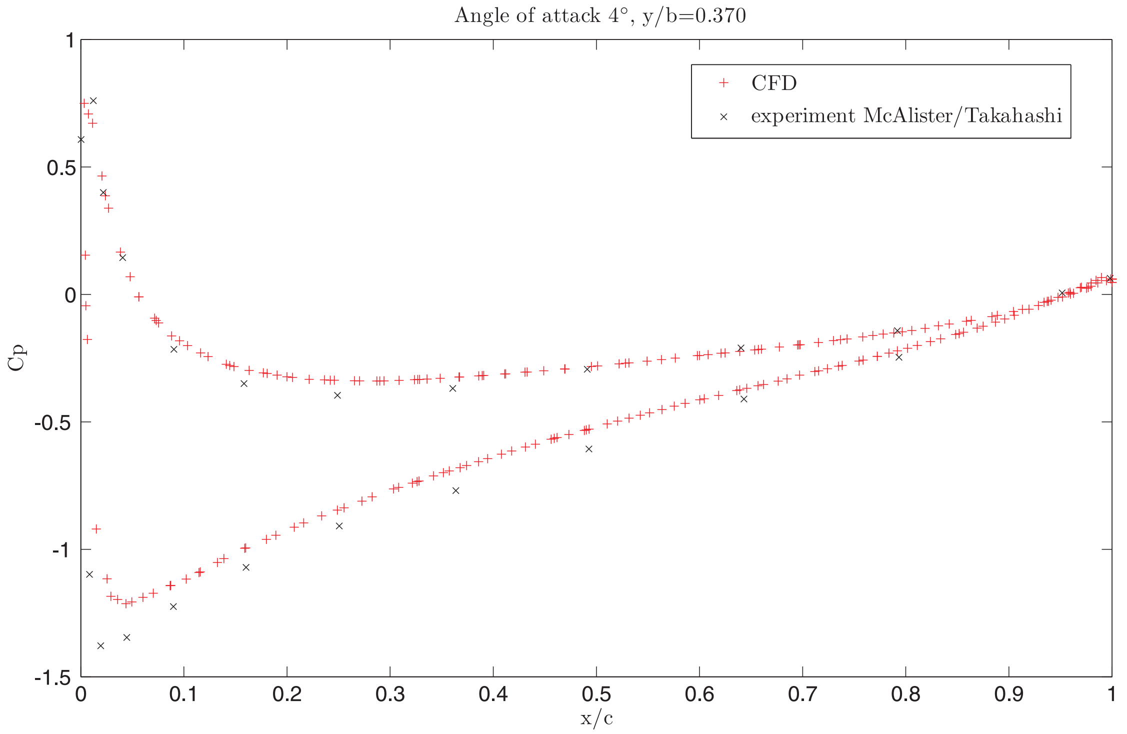

Figure 3.14: Pressure coefficient plot [$\alpha = 4°$, y/b=0.370].

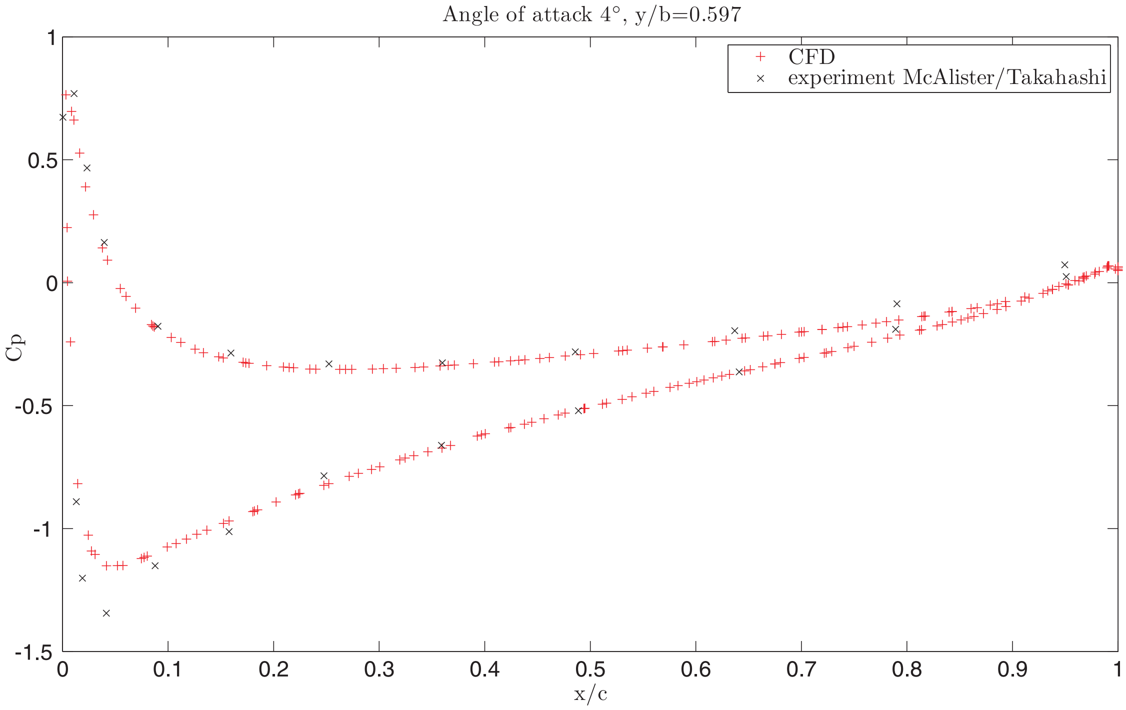

Figure 3.15: Pressure coefficient plot [$\alpha = 4°$, y/b=0.597].

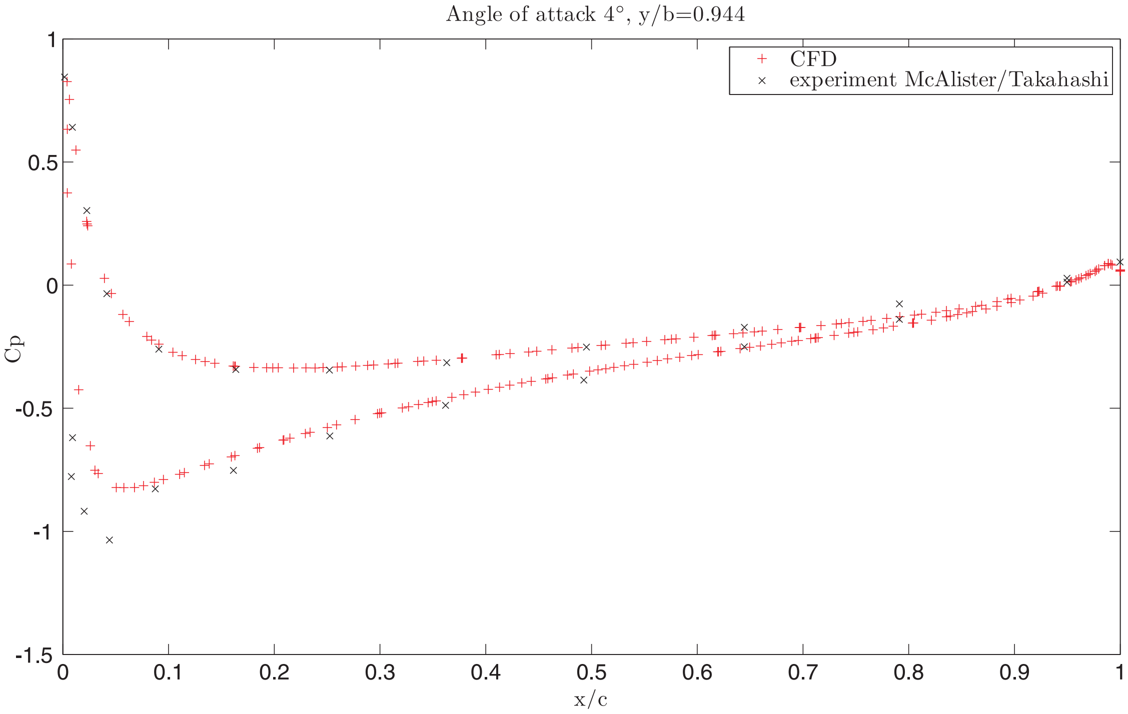

Figure 3.16: Pressure coefficient plot [$\alpha = 4°$, y/b=0.944].

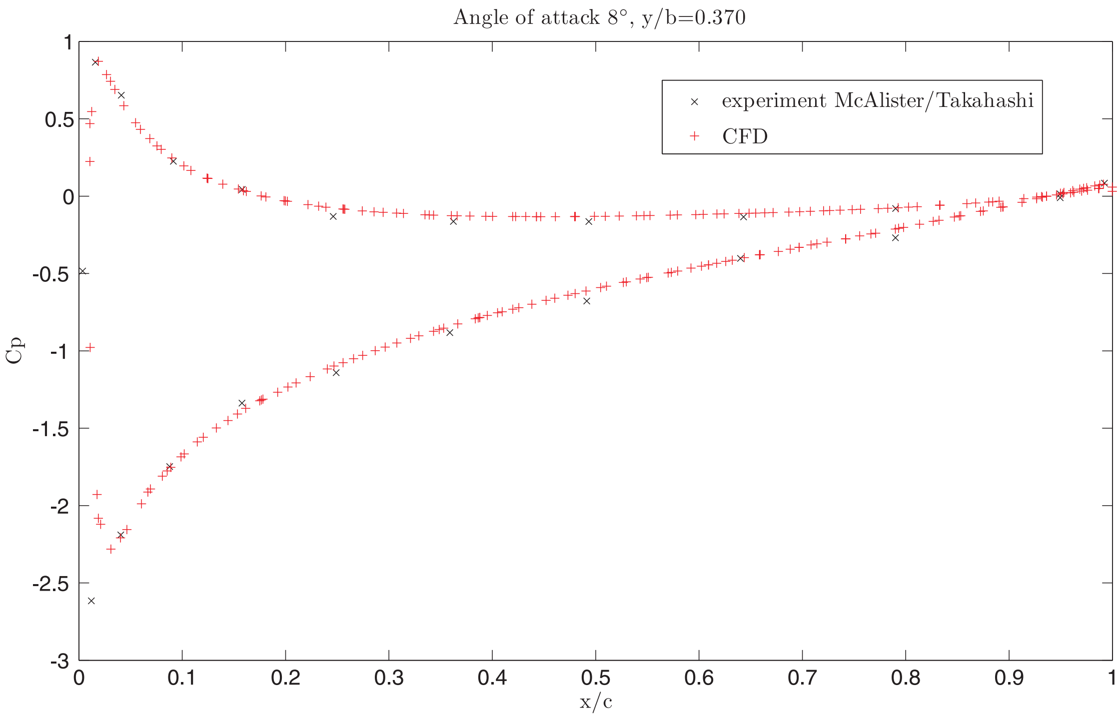

Figure 3.17: Pressure coefficient plot [$\alpha = 8°$, y/b=0.370].

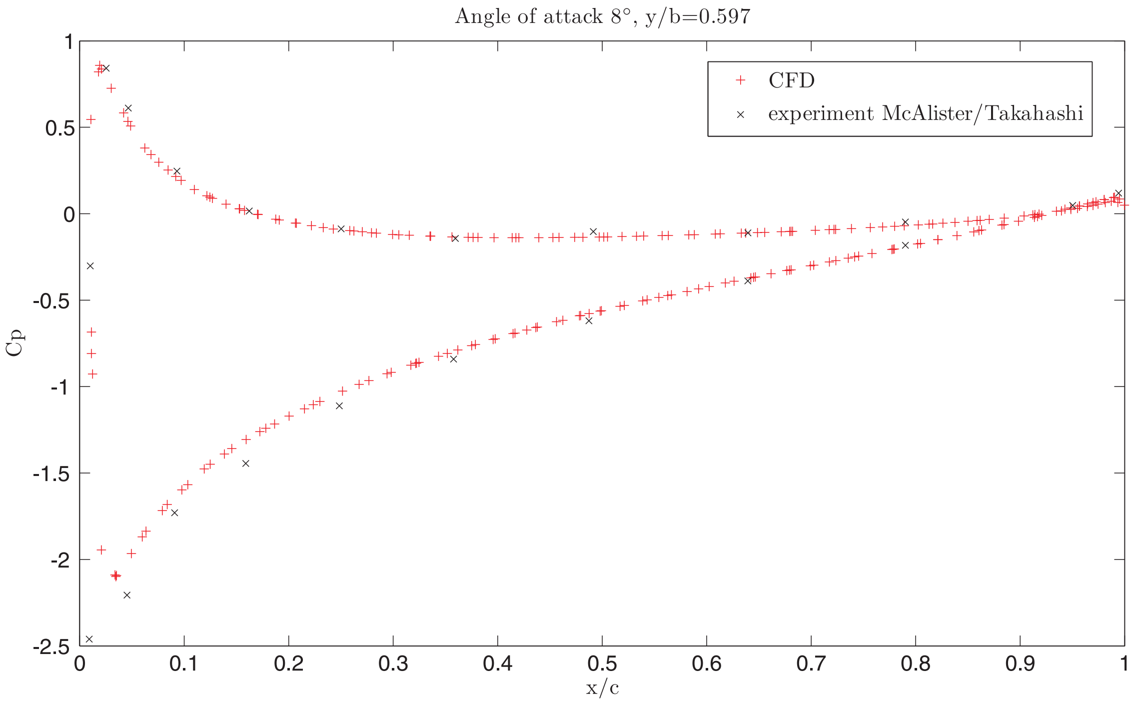

Figure 3.18: Pressure coefficient plot[$\alpha = 8°$, y/b=0.597].

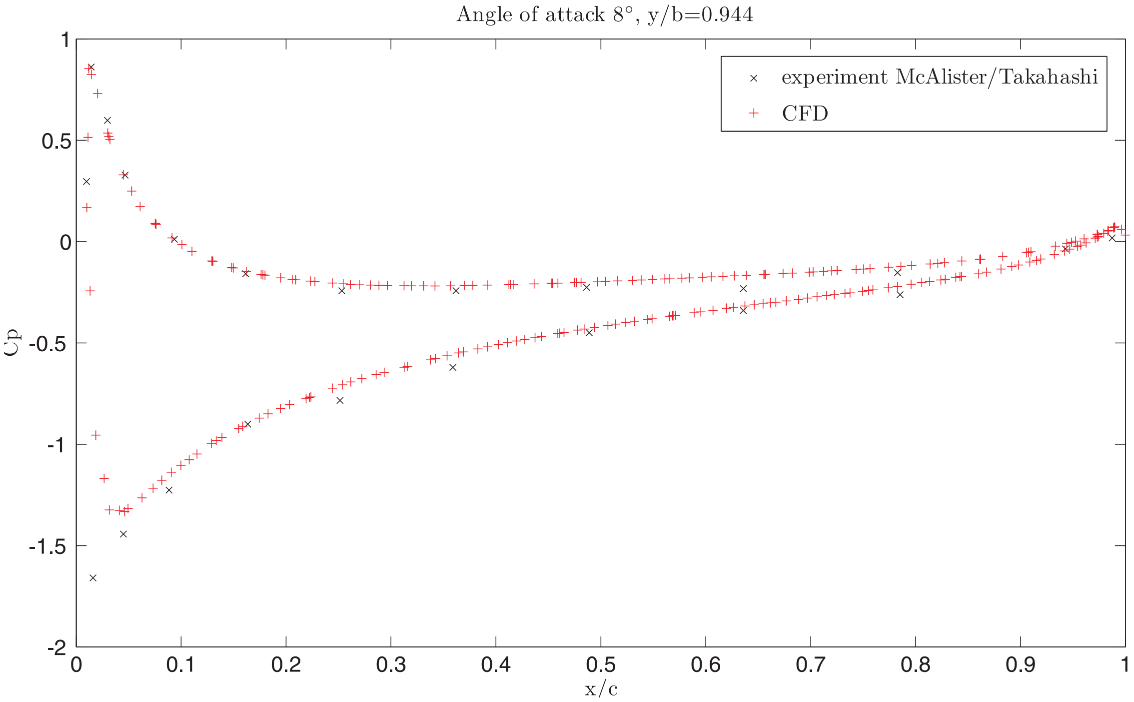

Figure 3.19: Pressure coefficient plot[$\alpha = 8°$, y/b=0.944].

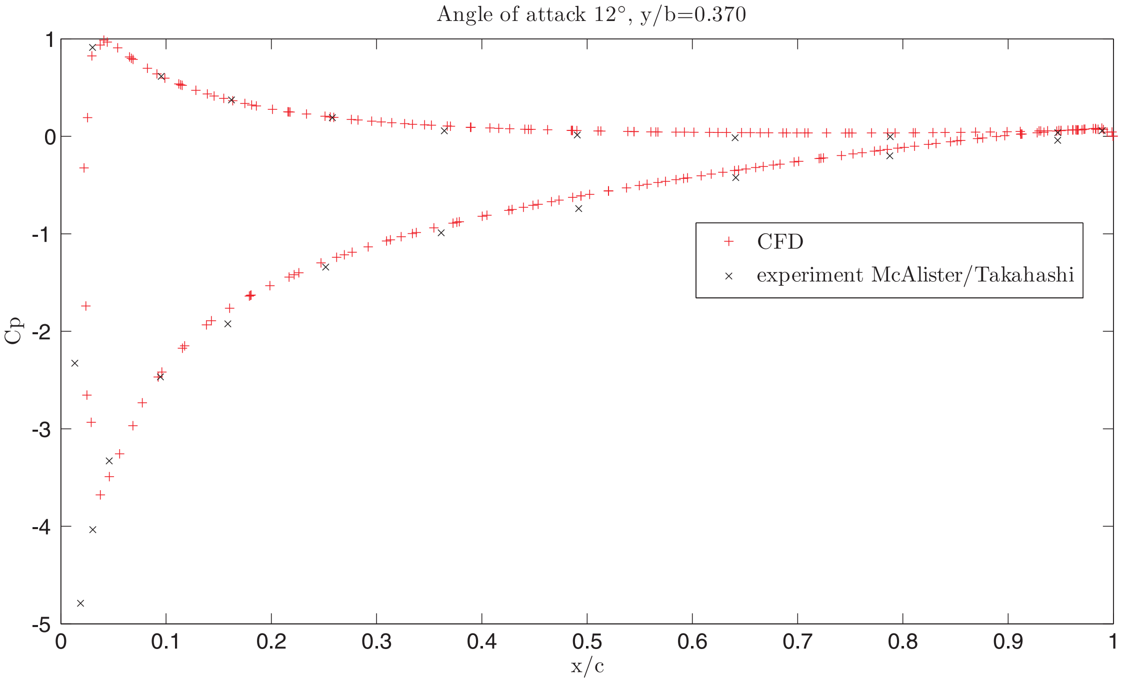

Figure 3.20: Pressure coefficient plot[$\alpha = 12°$, y/b=0.370].

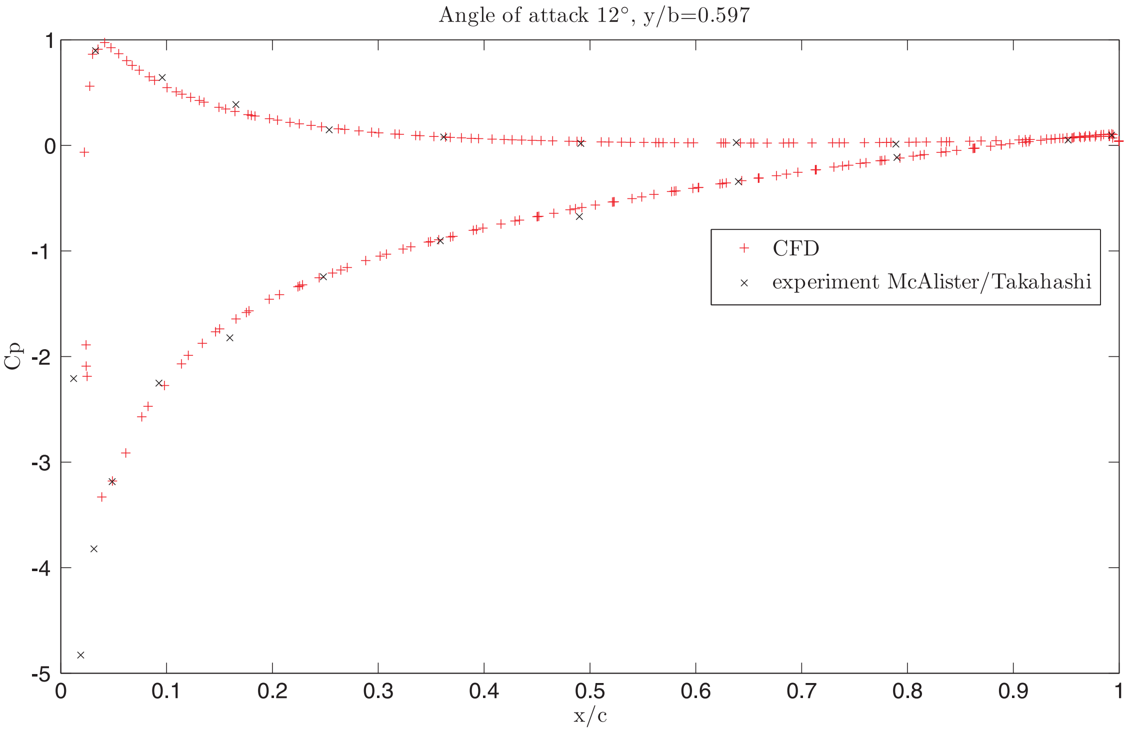

Figure 3.21: Pressure coefficient plot[$\alpha = 12°$, y/b=0.597].

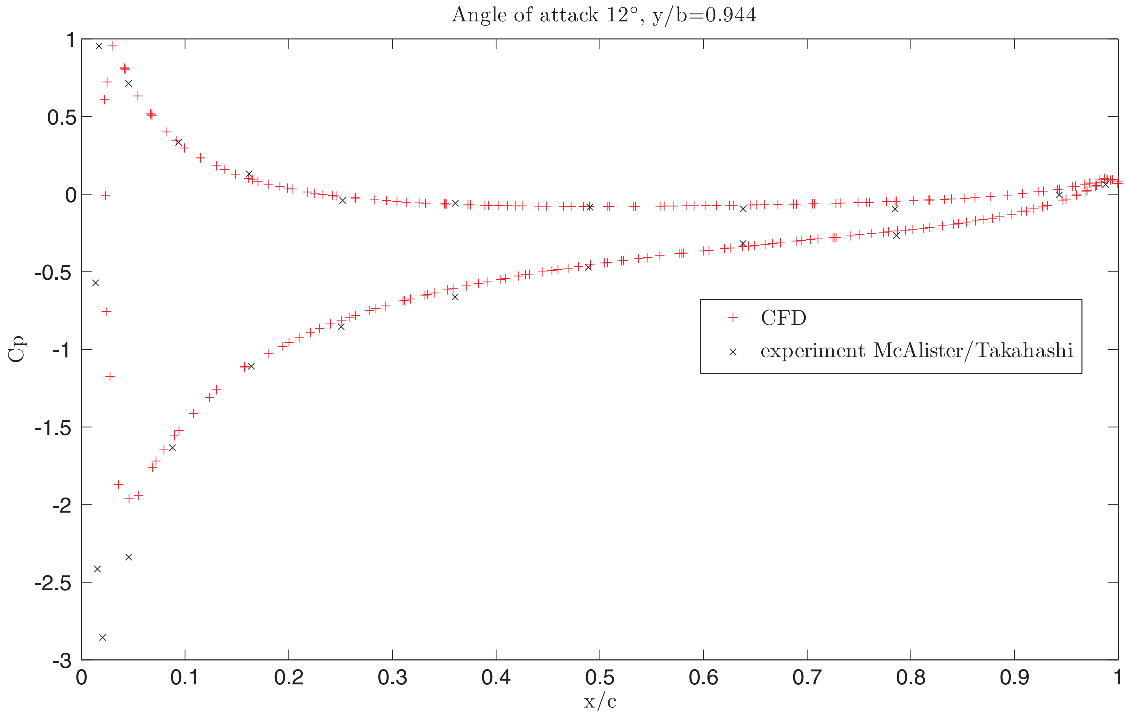

Figure 3.22: Pressure coefficient plot [$\alpha = 12°$, y/b=0.944].

4 Description of the AFC configuration

In this chapter will be discussed implementation of the AFC devices on the wing will be discussed. Set-up of the active flow control device, placement of the device on the wing, dimensions of the slots, actuation parameters and operating conditions are main tasks of consideration. Several configurations and setups are used in order to reveal the trends and to find the best possible configuration. From the various cases one appears to be the most effective and it will be discussed more thoroughly.

4.1 Actuation parameters

Before proceeding to the discussion of the physics of the controlled and natural flow, some further description of the actuation setup should be stated. In the present study all referenced parameters are dimensionless.

The flow from the blowing surfaces is assumed to have a constant velocity and turbulent viscosity profile following the classical top hat velocity boundary condition [8]. The global velocity ratio V_{Global} is defined as the ratio between the blowing velocity of the upper surface to the free stream speed:

$$V_{Global} = \frac{u_{bl\_upper}}{u_{\infty}}. \tag{4.1}$$

The momentum coefficient of the blowing device is defined as follows:

$$C_{\mu} = 2\frac{u_{bl}^2}{u_{\infty}^2}\frac{A_{bl}}{S} \tag{4.2}$$

where u_{bl} denotes the blowing velocity of the surface, u_{∞} the free-stream velocity, A_{bl} the total surface of the blowing slot and S denotes the reference area of the wing. The momentum coefficient for this configuration ranges from $C_{\mu} = 0.0003$ up to $C_{\mu} = 0.03$.

It will be shown that the efficiency of the AFC is affected by the ratio between the blowing velocity onto the upper surface and the blowing velocity onto the bottom surface. This ratio will be referenced here as the local velocity ratio and it is formulated as follows:

$$V_{local} = \frac{u_{bl\_upper}}{u_{bl\_bottom}} \tag{4.3}$$

In the examined cases it ranges between 0.8 and 1.25, which means that in some configurations the blowing is more intense on the upper surface and in some others it is more intense on the bottom one.

For the purpose of evaluations of the savings from every flow control configuration the effectiveness ratio η is formulated as follows:

$$\eta = \frac{P_{Drag\ reduction} - P_{Blowing}}{P_{Drag\ reduction}} \times 100 = \frac{P_{net}}{P_{saved}} \times 100\ [\%] \tag{4.4}$$

It is defined as the ratio of the net power which is saved from the active control divided by the total saved energy.

4.2 AFC configurations

As mentioned before, blowing slots are more effective close to the trailing edge than close to the leading edge. Configurations are designed with respect to this fact. In recent studies spanwise blowing configuration is often investigated. Spanwise blowing means that blowing slot is positioned on the side of the wingtip and direction of blowing is along y-axis. Advantage of the spanwise blowing devices is an easy implementation on the ordinary wings. It can decrease amount of drag but often it is not efficient in energy term. Due to this fact, spanwise blowing is not tested. Decision is based on the results from literature review [19], [21], [11], [32]. In the present study, nine layouts are investigated (see fig. 4.1, 4.2, 4.3).

Highest beneficial interaction of the jets with the wing tip vortex can be expected close to the tip. This is reason why all AFC devices are placed in the same region close to the wing tip. Slots are designed as parts of the wing surface and velocity boundary conditions are then assigned to this surfaces. In the present study, the blowing velocity vector acts always in the vertical direction (normal to the free-stream speed). Suction is not tested in this study. For comparison purpose, computations are performed with fixed mass flow rate from the blowing surfaces. In the present study, the mass flow rate is 0.03 kg/s. Inputs and results can be found in table 4.

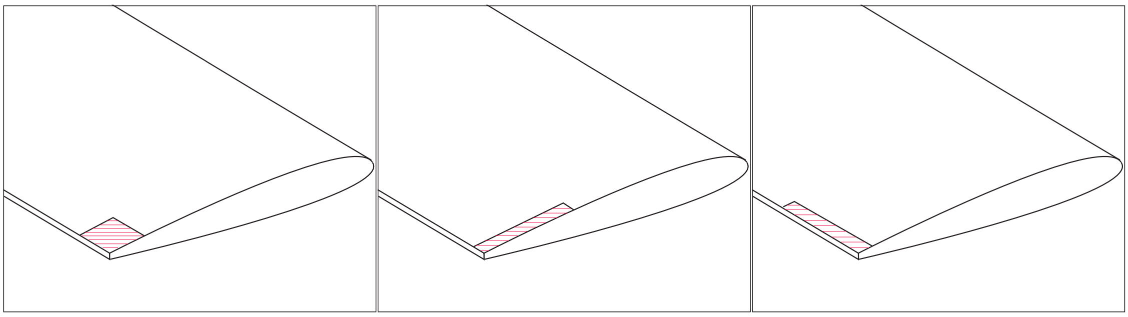
(a) Case 01 (b) Case 02 (c) Case 03

Figure 4.1: Tested configurations.

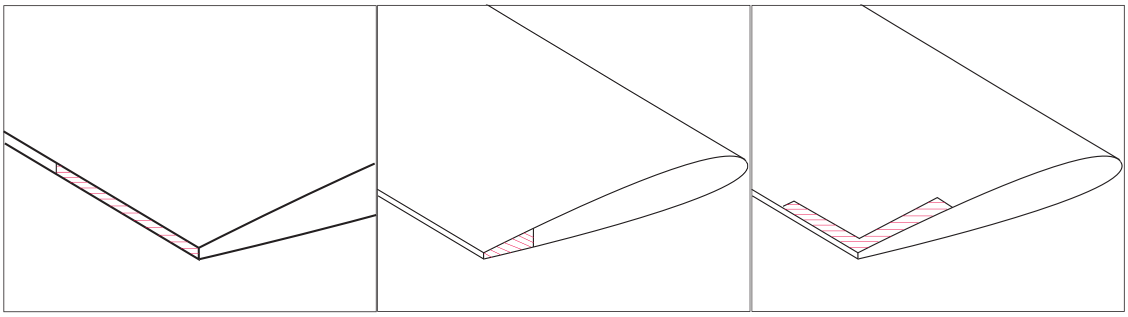

(a) Case 04 (b) Case 05 (c) Case 06

Figure 4.2: Tested configurations.

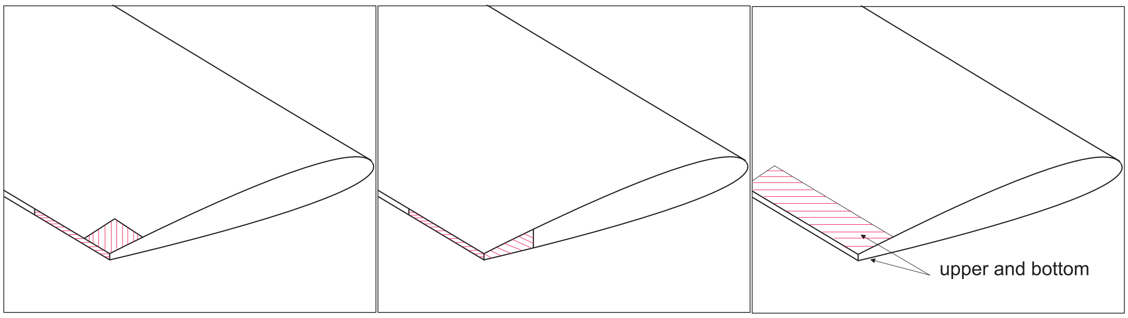

(a) Case 07 (b) Case 08 (c) Case 09

Figure 4.3: Tested configurations.

Drag reduction occurs almost at all cases as it could be seen from the results summarized in tab.4. Unfortunately, lift is negatively affected as well. The lift coefficient has higher magnitude than the drag coefficient. This means that the same percentage change of the coefficients means much higher impact on the lift than on the drag force. Due to this fact, same or higher lift coefficient is important criterion and successful case has to fulfill it. Only in case number 9 is found that drag and lift forces are simultaneously and favourably affected. It is case with two blowing surfaces (fig. 4.3c and 4.4). One lies on the upper surface and second on the bottom surface. Based on the results, configuration 9 is selected for more thorough investigation. Other cases are classified as unsuccessful and they will not be investigated. Position of the slots according to the configuration 9 brings some difficulties. Position of the slots coincide with ailerons. The ailerons are used to control the aircraft in roll. Reasons why presented configuration is investigated despite of this fact is an idea that AFC device could replace all common control devices on the wing in the future. Height of the trailing edge is another difficulty. It could be complicated to place the equipments as pipes and jets into relative small space. The discussion will

Tab4: **Comparison of configurations:**

case	Total area m^2	Mass flow rate kg/s	Volume flow rate m^3/s	Blowing speed m/s	C_L [-]	C_D [-]	ΔC_L [%]	ΔC_D [%]
ref.	×	×	×	×	0.902	0.064	×	×
1	0.00089	0.03	0.0245	27.6	0.898	0.0636	-0.37	-0.87
2	0.00116	0.03	0.0245	21.1	0.899	0.0637	-0.27	-0.74
3	0.00074	0.03	0.0245	33.3	0.894	0.0631	-0.85	-1.67
4	0.00018	0.03	0.0245	135.7	0.900	0.0639	-0.19	-0.41
5	0.00071	0.03	0.0245	34.6	0.903	0.0645	+0.17	+0.5
6	0.00135	0.03	0.0245	18.2	0.896	0.0632	-0.66	-1.48
7	0.00101	0.03	0.0245	24.3	0.899	0.0635	-0.33	-1
8	0.00087	0.03	0.0245	28.2	0.902	0.0643	+0.1	+0.21
9	0.00238	0.03	0.0245	10.3	0.902	0.0636	0	-0.96

take place in the section 6.1.1. Position of the slots on the wing and its effect on the wing performance will be described in the section 6.1.3.

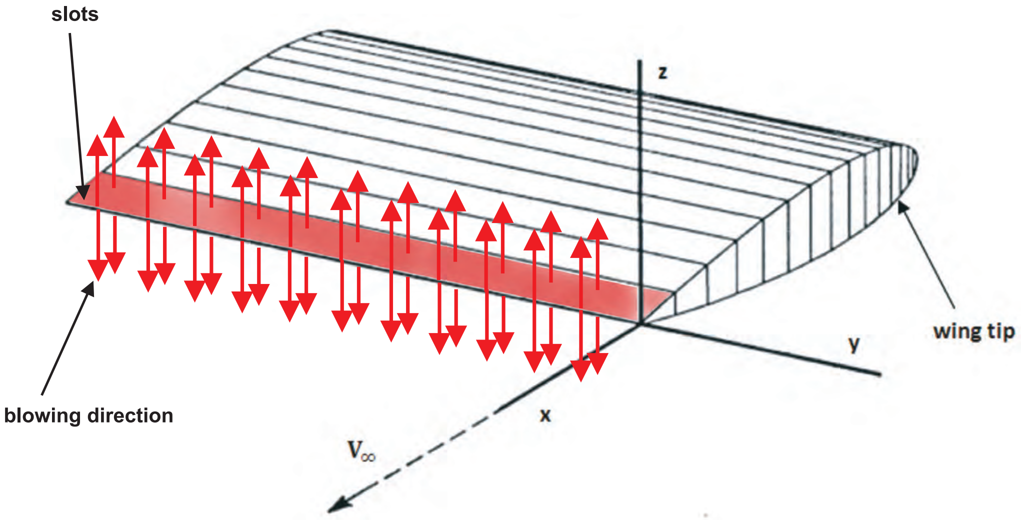

Figure 4.4: Preview of the AFC configuration.

4.3 Description of a successful case

In the previous section, it is discussed the case where drag decreased and lift increased at the same time. During first tests, an initial size of the slot was 0.26% of the total surface area of the wing. It could be reasonable to enlarge the size of the slots in order to obtain better performance. Regarding this fact, length of the slot is changed to 0.8 m and its width to 0.05 m. Then, surface area of both slots is around 9% of the total surface area of the wing (see fig. 4.5).

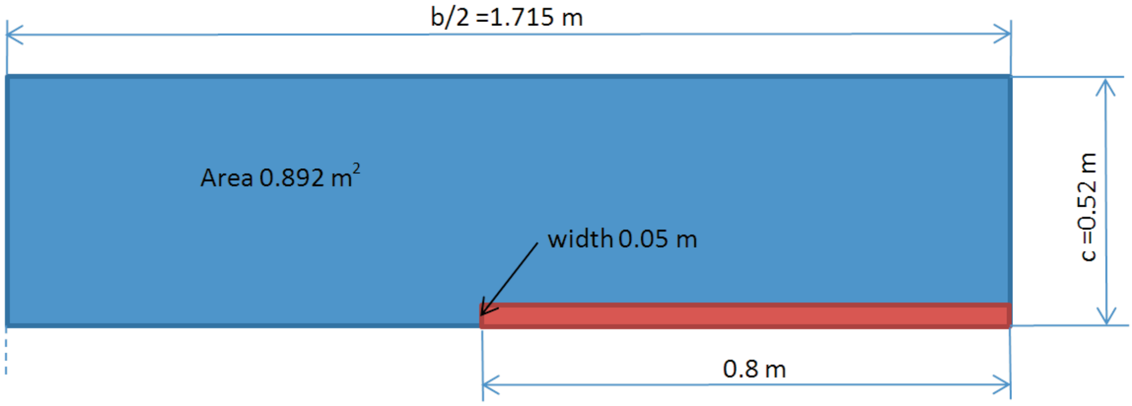

Figure 4.5: Slots arrangement on the wing.

Surface separation was done in Fluent from the original meshes. In Fluent it can be done by the box bounding the mesh inside. Edges of that box are parallel to the axis of the domain. Due to the fact that wing operates at an angle of attack, it is not possible to cut the surface perpendicular to the wing's chord. Slight deviations are obtained for the surface area of the slots. Bottom slot has lower width and its surface area is smaller in comparison to the upper one. Deviations at different angles of attack can be found summarized in tab. 5.

Tab5: **Slight deviations in surface area:**

	Surface area m^2	
	upper slot	bottom slot
Ideal	0.04	0.04
4°	0.0404	0.0397
6°	0.0415	0.04
8°	0.0425	0.0392
10°	0.0436	0.0397
12°	0.0422	0.0385

5 Physics and results

In this chapter the results for the selected configuration will be presented. Results will be thoroughly discussed including physics of the flow, aerodynamic performance, aerodynamic loads and energy efficiency in controlled flow cases. They are mainly presented in graphs and values could be found summarized on the DVD disk enclosed with this thesis.

5.1 Physics of the natural and controlled flow

The flow is controlled by two large slots, which are placed in the rear part of the wing and they extend from the mid-span up to the wing tip area (fig. 4.5). This configuration is tested for the global velocity ratio V_{Global} (eq. 4.1) which ranges from 0.04 up to 0.34. The wing operates at 5 angles of attack, namely 4°,6°,8°,10° and 12° and always at travel speed of 70 m/s. It is found that upper slot has significant effect on the drag reduction even if it works alone (see fig. 5.1). The lift force is not stabilized and in most of the times lift is lower than the computed one in the natural flow regime. The bottom slot has the blowing direction opposite to the direction of the lift force and acts as a counterbalance. The active bottom slot produces an increase of the lift but also it has a negative effect on the drag. It is found that when applying simultaneous blowing to the upper and lower surfaces, the lift could remain the same or increases, while the drag decreases. Single AFC device (upper or bottom) effect on the lift and drag on the wing set at $\alpha = 12^\circ$ could be seen in fig. 5.1 and 5.2.

The effectivity of the device is affected by the ratio between the blowing velocity onto the upper surface and the blowing velocity onto the bottom surface. This ratio is referenced as the local velocity ratio V_{local} (eq. 4.3). At higher values of the V_{local} than 1.25, the bottom slot is not capable to stabilize the lift. If a value of the V_{local} is lower than 0.8, the negative effect on the drag from the bottom slot outweigh the positive effect from the upper slot. In figure 5.3 it could be seen the range of the possible local velocity ratios. It ranges between 0.8 and 1.25 for the lift increase or the lift stabilization and simultaneous drag reduction. However, it is found in many cases that more practical is the range between 0.8 up to 1.1.

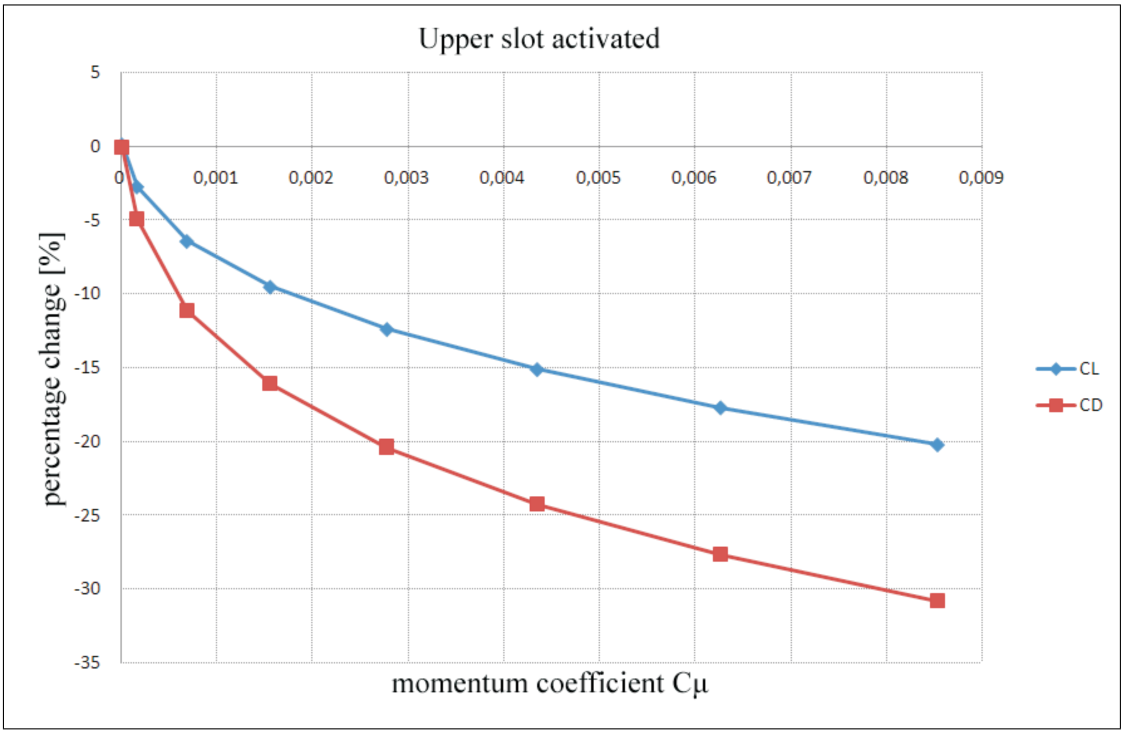

Figure 5.1: Upper slot activated.

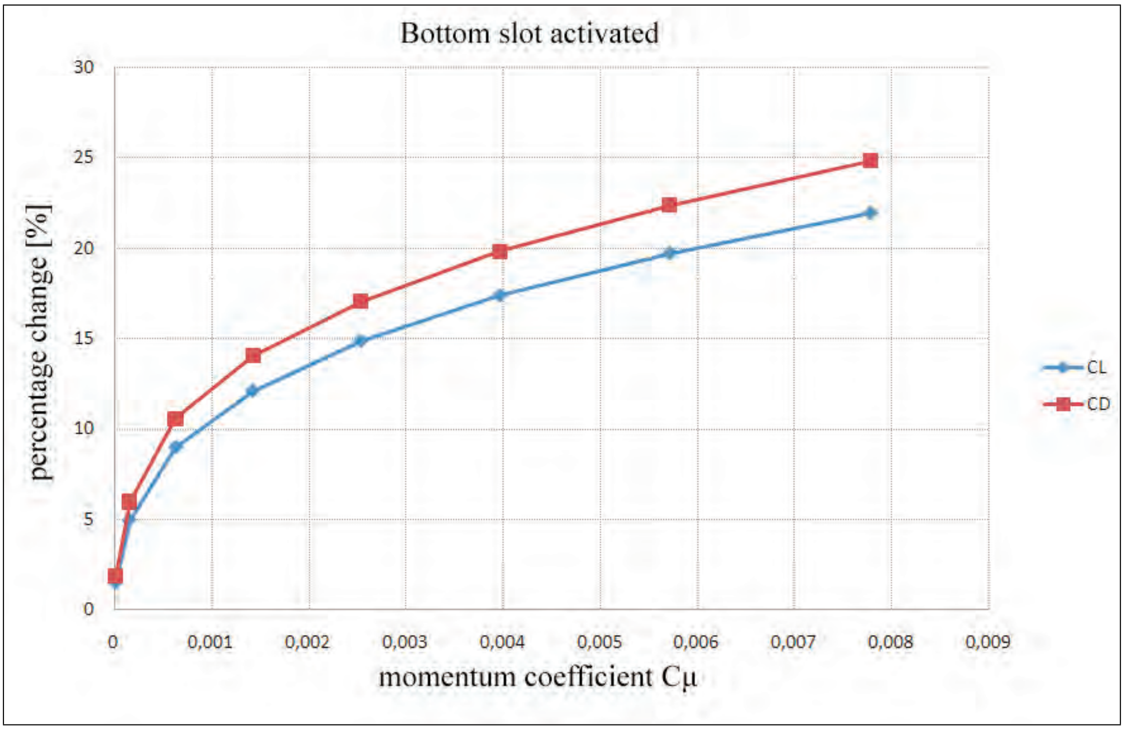

Figure 5.2: Bottom slot activated.

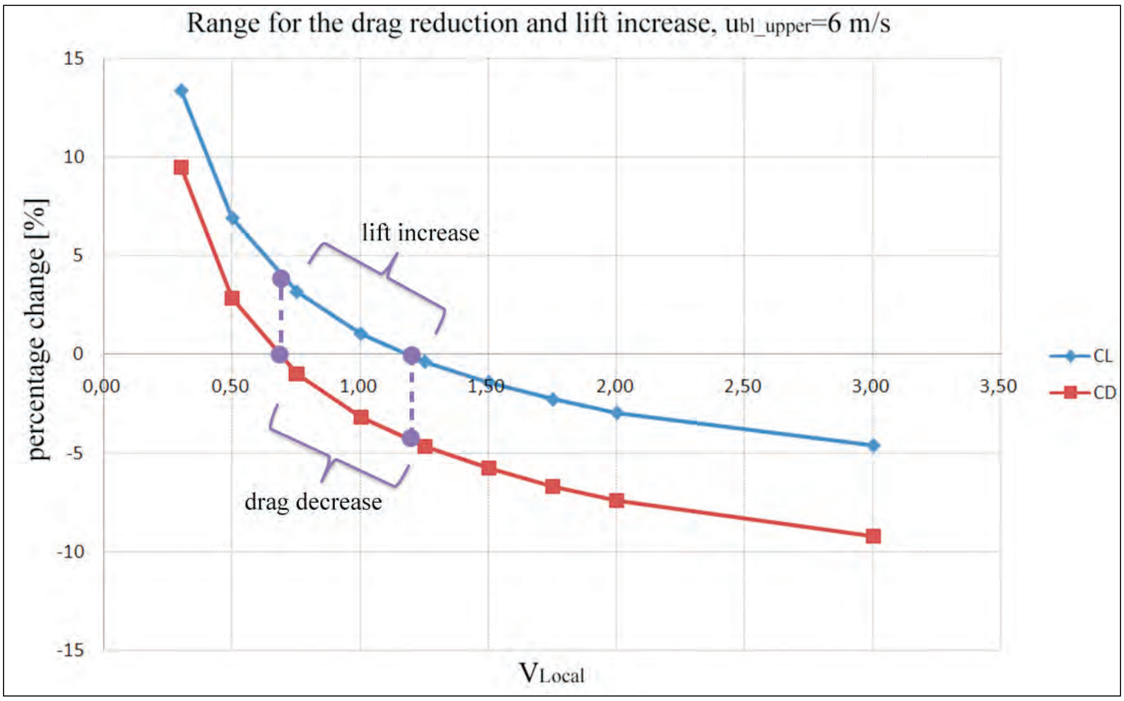

Figure 5.3: Range of the possible local velocity ratios.

Before proceeding to the discussion of the physics, some further description of the selected cases should be stated. For every angle of attack two representative blowing cases are selected and they are compared to the natural flow case. Representative cases are selected from the computed variants which lie in ranges of $V_{local} = 0.8 - 1.25$ and $V_{global} = 0.04 - 0.34$. The first one considers stabilization of the lift and high drag decrease and the second one simultaneous lift increase and drag decrease. Representative cases and their results at different angles of attack can be found summarized in tab.6 and tab.7.

Tab6: **Representative lift stabilized cases:**

α [Deg]	V_{Local} [-]	V_{Global} [-]	C_L [-]	C_D [-]	ΔC_L [%]	ΔC_D [%]
4	1	0.271	0.3194	0.0132	+0.134	-34.108
8	1	0.1714	0.6269	0.0318	+0.01	-13.964
12	1	0.2771	0.9021	0.0564	-0.003	-12.167

Tab7: **Representative lift maximized cases:**

α [Deg]	V_{Local} [-]	V_{Global} [-]	C_L [-]	C_D [-]	ΔC_L [%]	ΔC_D [%]
4	0.8	0.343	0.3581	0.0123	+12.259	-38.781
8	0.8	0.1714	0.6509	0.0326	+3.841	-11.682
12	0.8	0.2571	0.9337	0.0588	+3.505	-8.375

The present active control affects globally and locally the flow field. The dimensionless axial vorticity is plotted in fig. (5.7 up to 5.15) for the natural and selected blowing cases at $\alpha = 4°$, $8°$ and $12°$. When no control is applied (see fig. 5.13), the axial vorticity starts to emanate mainly from the lower surface and then starts to shift towards the wing tip area and the upper area of the wing. As it is expected, intensity of the axial vorticity increase with angle of attack. At lower angles of attack ($\alpha = 4°$) a single core vortex is formed at the trailing edge area. At higher angles of attack ($\alpha = 8°$, $10°$), it is observed a well formed “double core” vortex. Further downstream, the bottom core merge with the upper dominant vorticity structure. This leads to a single core vortex, which moves upward and inwards (towards the root). When blowing is applied, the upper vorticity core is shifted upward and the bottom core is moved downward and outboard. A vorticity region between those two structures is significantly weakened and it is observed that a small layer of negative axial vorticity is formed between the two main vortical structures. This negative axial vorticity structure merge with the other vortices into a single core vortex. At $\alpha = 4°$ patterns are quite similar. Decomposition of the vorticity core into two structures is also observed. An upper part is again shifted upward but the upper vorticity core seems to be weakened. The bottom structure is shifted downward and outboard and the magnitude of the bottom vorticity core is increased. In the plot (see fig. 5.16) which shows axial vorticity along the whole wing span are observed another two areas of high vorticity. Those two areas are close to the mid-span position, where blowing begins to apply. Those vortices with different sign of vorticity are expected to be formed, since the vertical blowing action from upper and lower surfaces impose directly a significant amount of vorticity (positive to the upper and negative to the lower area) to the undisturbed three dimensional cross-flow. Those vortices are diffused quite fast downstream of the wing. Blowing from both surfaces does not appear to significantly alter the vorticity distribution upstream of the control. As it could be seen in the fig. (5.12 and 5.15) the shape of the vorticity structure upstream remains the same but the magnitude is a little bit lower.

The observed vorticity patterns are similar to those ones plotted in the low Reynolds number flow measurements of Margaris [19]. However, in the aforementioned study, the vortex diffusion was much weaker from the present one. Farther from the trailing edge $(x/c > 2)$, based on some relevant experimental studies, vortex diffusion is increased [9]. The diffusion regime is predicted here. However, the rate of diffusion seems to be over predicted. The overestimated diffusion of the vortex in the near-wake of the wing is attributed to the numerical dissipation of the solver, which can't be avoided with the present resolution of the mesh. It is important to remark that the rate of diffusion looks promising for deploying faster decay of the aircraft wake vortices.

Vertical velocity plots are plotted in fig. (5.17 up to 5.25) for the natural and selected blowing cases at $\alpha = 4^\circ$, 8° and 12°. Blowing changes the entire domain close to the trailing edge and downstream of the wing. At $x/c = 0.02$ (just behind the wing) it is observed at $\alpha = 4^\circ$ that negative area of vertical velocity on the upper part of the wing dissapears when blowing is applied. As the angle of attack is increasing, the area with negative vertical velocity is observed, but it is weaker than in the natural flow. This behaviour is expected since from the upper slot is imposed positive vertical flow. At section $x/c = 0.5$ could be seen that at all blowing cases the positive velocity is decreased and the velocity regions are more diffused compared to the respective ones in the natural flow regime. This conclusion is consistent with the previous vorticity plots. At $x/c = -0.25$, it is observed that flow is also affected upstream. Vertical velocity is reduced in the region before the upper slot. This behaviour is clearly visible in the pathlines plot (fig. 5.6). In the inward part of the wing, where blowing is not applied, the flow follows the natural flow distribution. In fig. 5.26 the vertical velocity is plotted along the whole wingspan of the wing and in fig. 5.27 could be found vertical velocity plotted at three sections of the wing's span. At $y/b = 0.37$ where blowing is not applied, the flow fields are almost identical. It is in compliance with previously mentioned velocity plots along the wing span. At $y/b = 0.59$, blowing is applied and the effects are pronounced. The natural downwash is suppressed and stretched towards the leading edge. In fig. 5.27 could be found that the vertical velocity is affected on the upper surface of the wing from location at $x/c = -0.25$. Vertical velocity of the flow increases, since the upper blowing immerses mass flow vertically. This effect could be also seen in fig. 5.6. On the bottom surface the jet flow does not collide to the free-stream flow so strongly and the bottom jet flow is more diffused than the upper one. Close to the tip area at $y/b = 0.94$, the controlled flow is completely different from the natural flow. In the region located on the upper surface, the well-formed downwash is observed in the natural flow regime. In controlled flow cases, the region located downstream has similar magnitude of velocity as in the the natural flow but the region upstream has lower values. Between those areas, the upper jet is immersed into the flow and collides to the already oppositely directed flow.

Pathlines of the flow are plotted in fig. 5.5 and 5.6. The wing operates at $\alpha = 12^\circ$ and the natural flow regime is compared to the case with $V_{Global} = 0.25$ and $V_{Local} = 0.8$. Volume pathlines are colored by dimensionless vertical velocity. In the inner region of the tip vortex, the natural flow rotates faster, thus possesses higher core vorticity. It is observed that in the controlled flow regime the trailing vortex is more displaced and also the tip vortex is weakened and the flow possesses much lower vertical velocity but also rotational energy. This conclusion is consistent with the direct comparisons of vorticity in fig. 5.15. When no control is applied, the flow remains attached to the upper surface. In the controlled flow regime, the flow upstream of the slot leaves the upper surface in advance due to the vertically added mass from the upper slot. Deflected flow creates a well-formed trailing edge vortex behind the trailing edge. This vortex extends through the whole span-wise length of the blowing surface. Similar pattern could be observed in turbulent flow over a backward facing step where region of recirculation is formed behind the step (fig. 5.4 A). The trailing edge vortex could be seen in fig. 5.4 B.

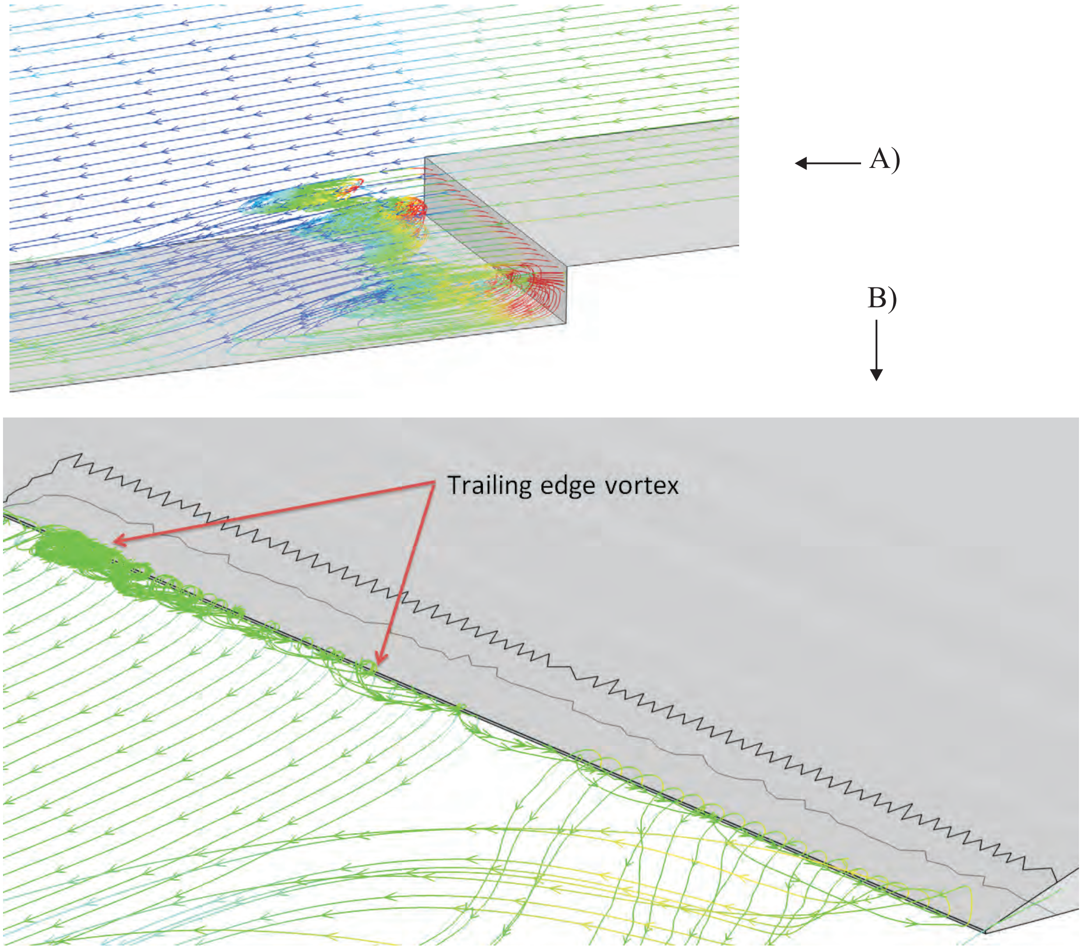

Figure 5.4: Trailing edge vortex.

Pressure distribution is plotted in fig. (5.28 up to 5.36) for controlled and the natural cases. In the controlled flow regimes, it is observed that the pressure upstream and close to the slots position increases, because the outer-flow decelerates, while it approaches the immersed jet. Through the slot, the flow starts accelerating by gaining some momentum in the vertical direction. This leads to the pressure decrease which could be seen close to the trailing edge. This distribution of pressure leads to significant drag reduction, since the increased pressure still acts onto the rear part of the airfoil. It is observed that blowing does not intensively alter the pressure distribution at the inner area of the wing, far away from the tip.

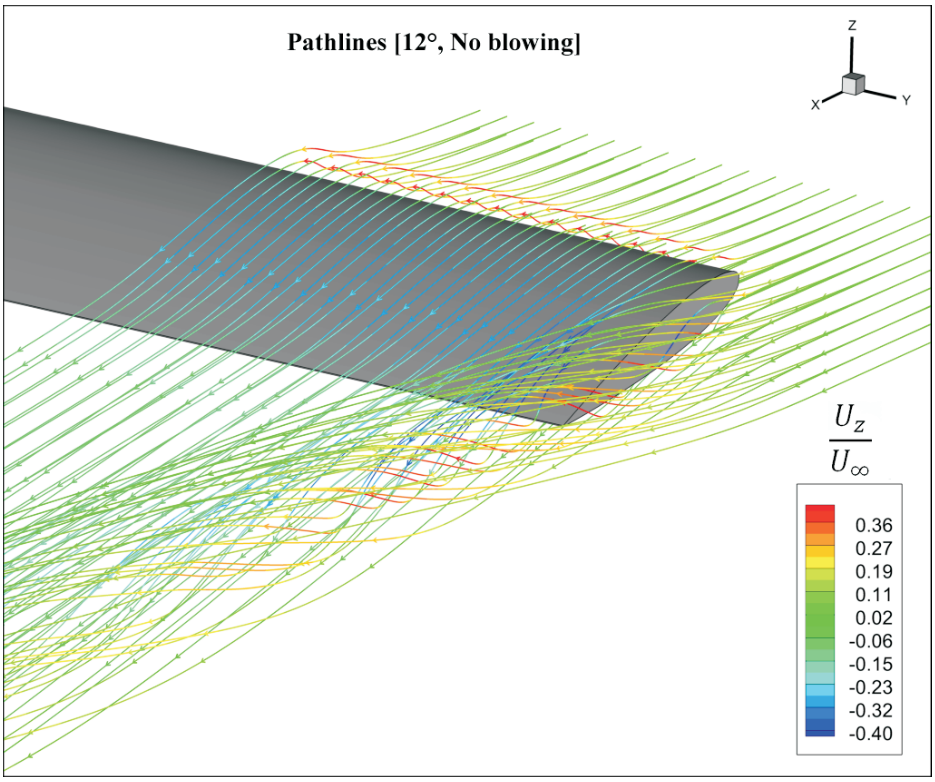

Figure 5.5: Pathlines of natural case

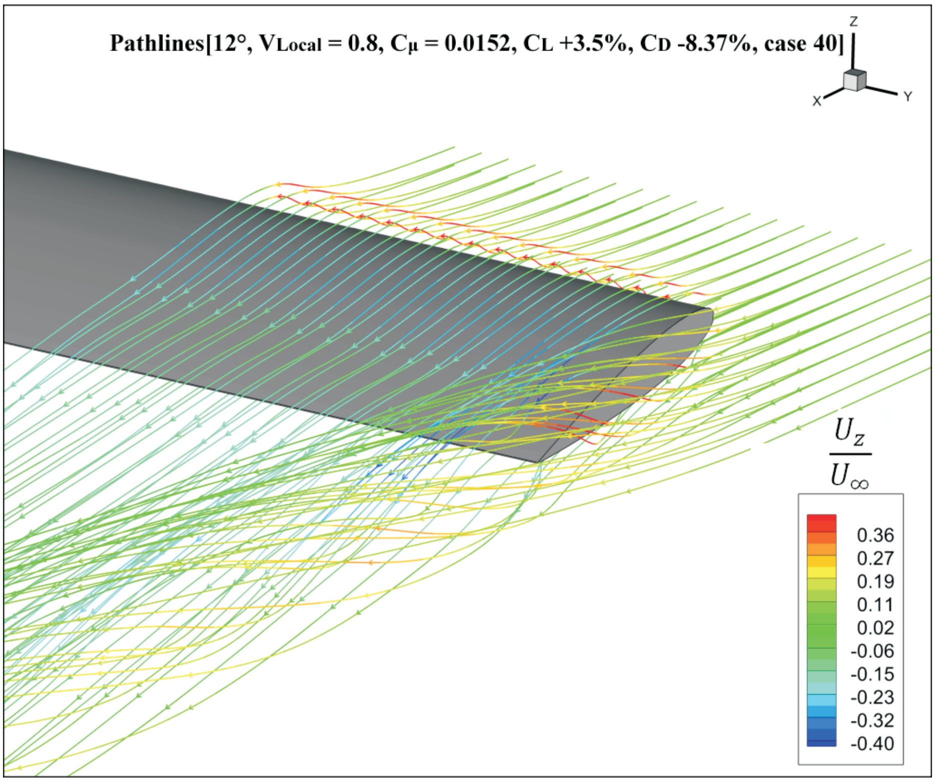

Figure 5.6: Pathlines of blowing case

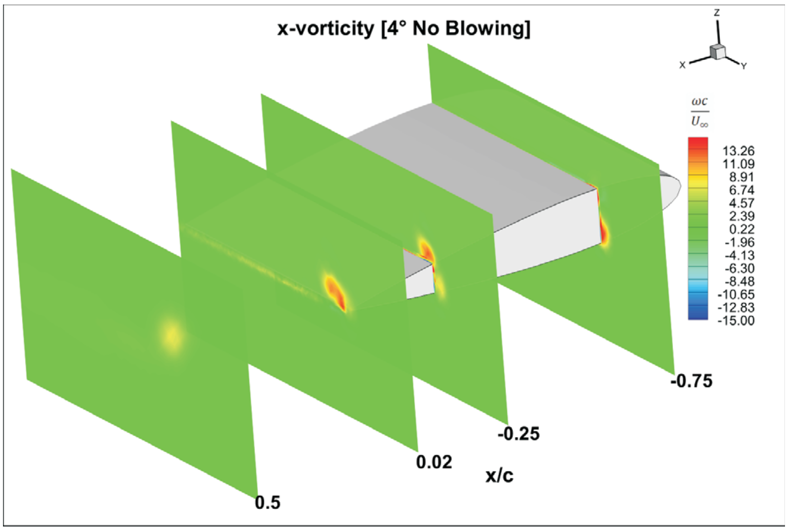

Figure 5.7: x-vorticity plot [$\alpha = 4°$, no blowing].

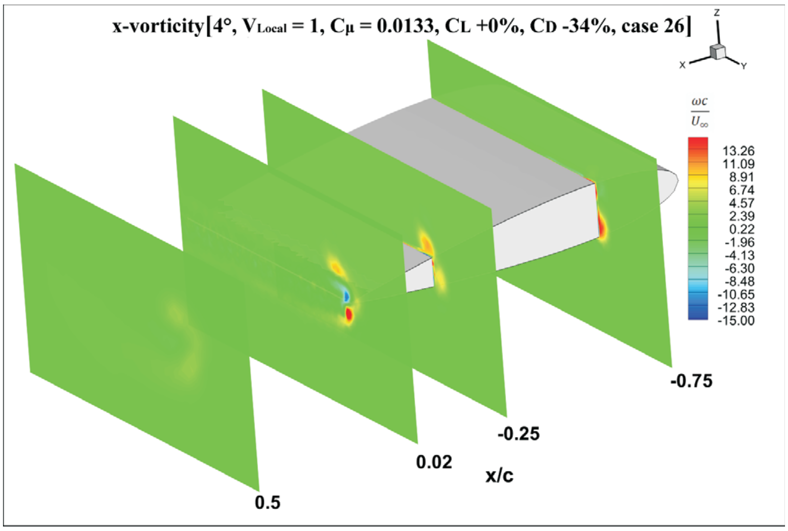

Figure 5.8: x-vorticity plot [$\alpha = 4°$, lift stabilized].

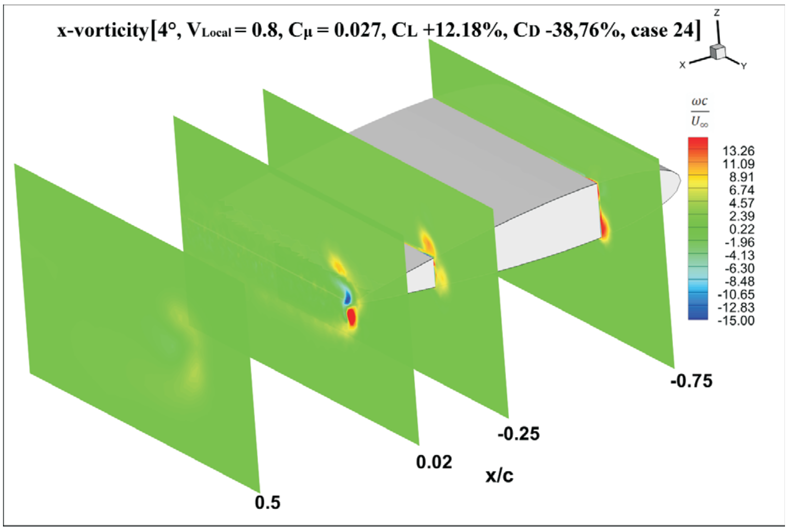

Figure 5.9: x-vorticity plot [$\alpha = 4°$, lift maximized].

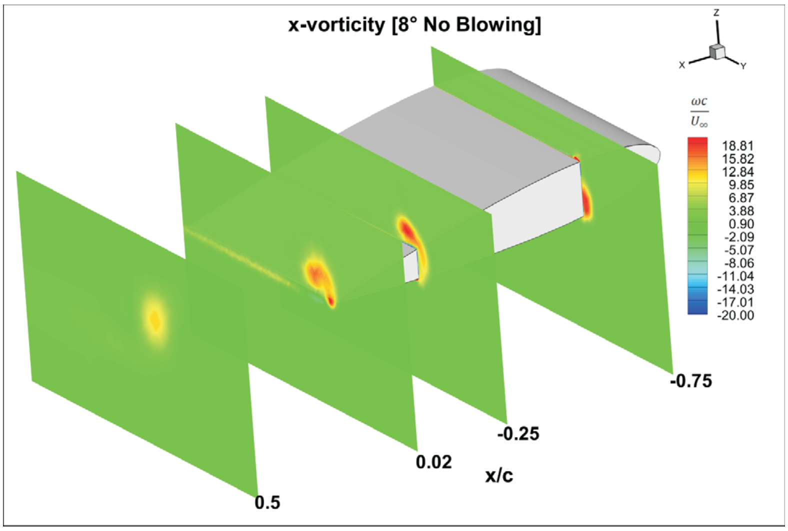

Figure 5.10: x-vorticity plot [$\alpha = 8^{\circ}$, no blowing].

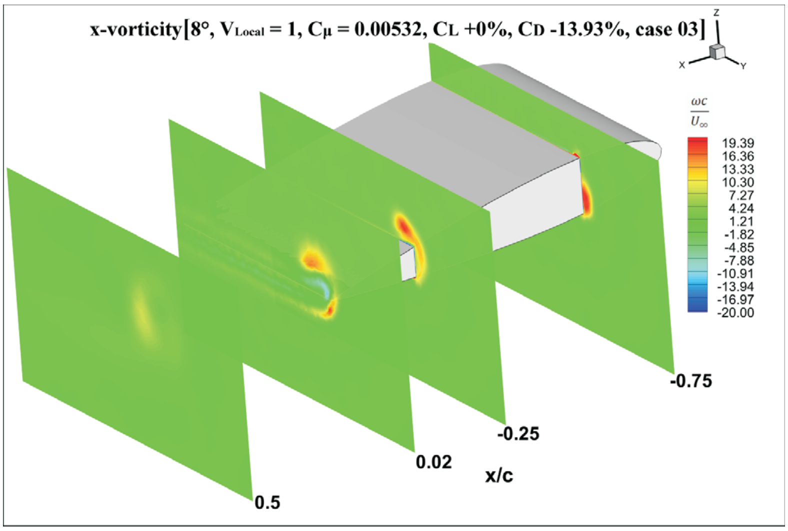

Figure 5.11: x-vorticity plot [$\alpha = 8^{\circ}$, lift stabilized].

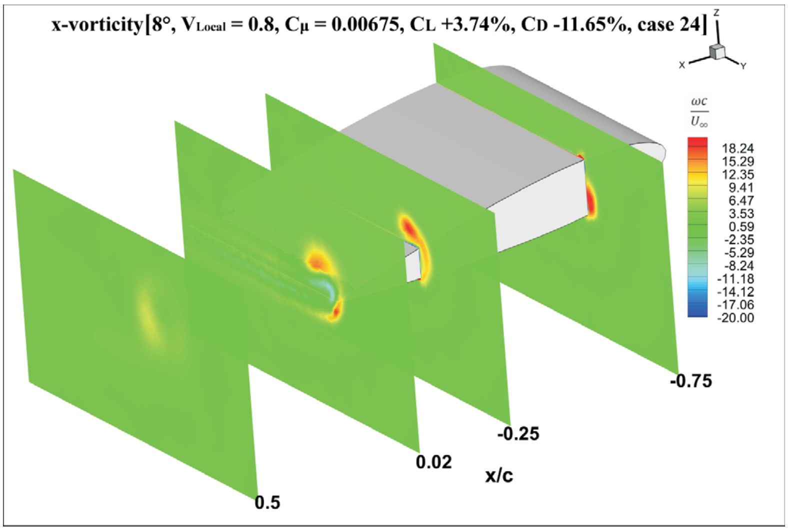

Figure 5.12: x-vorticity plot [$\alpha = 8^{\circ}$, lift maximized].

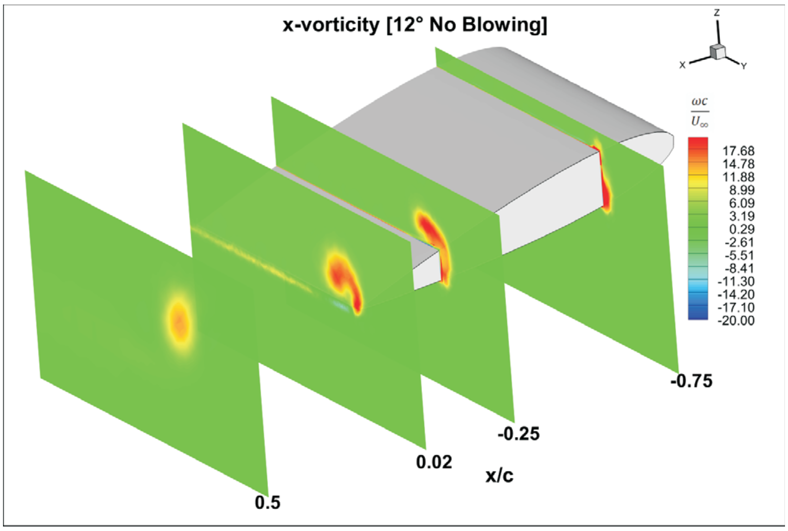

Figure 5.13: x-vorticity plot [$\alpha = 12°$, no blowing].

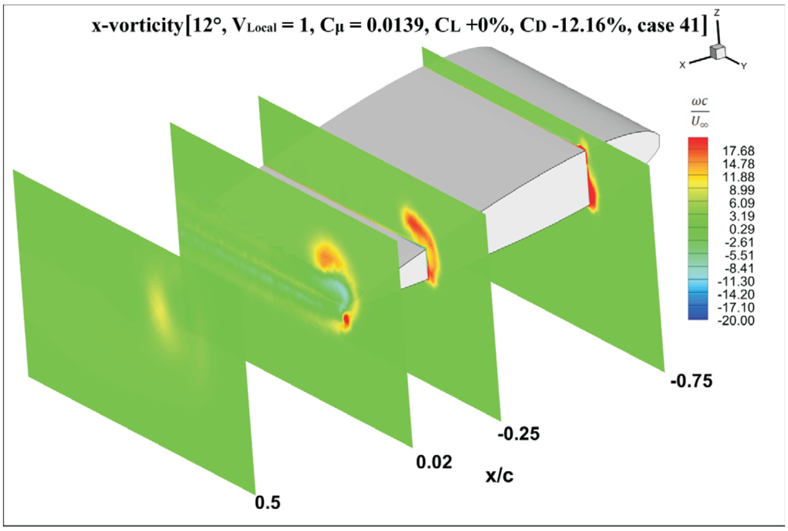

Figure 5.14: x-vorticity plot [$\alpha = 12°$, lift stabilized].

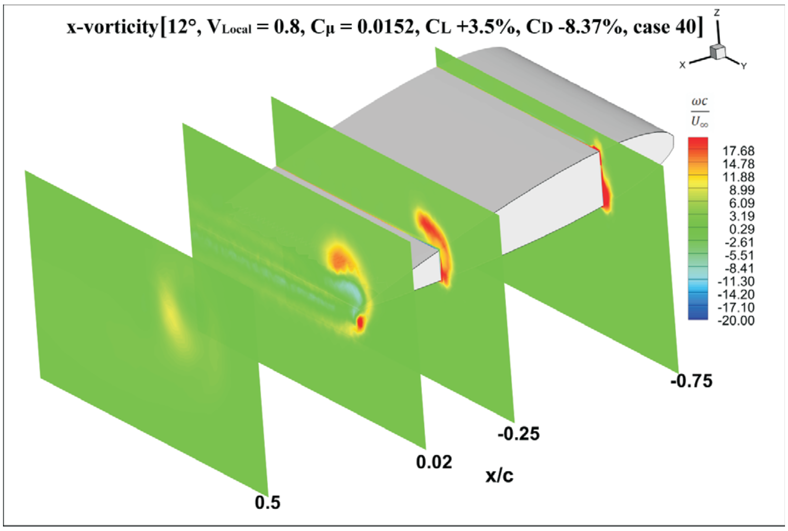

Figure 5.15: x-vorticity plot [$\alpha = 12°$, lift maximized].

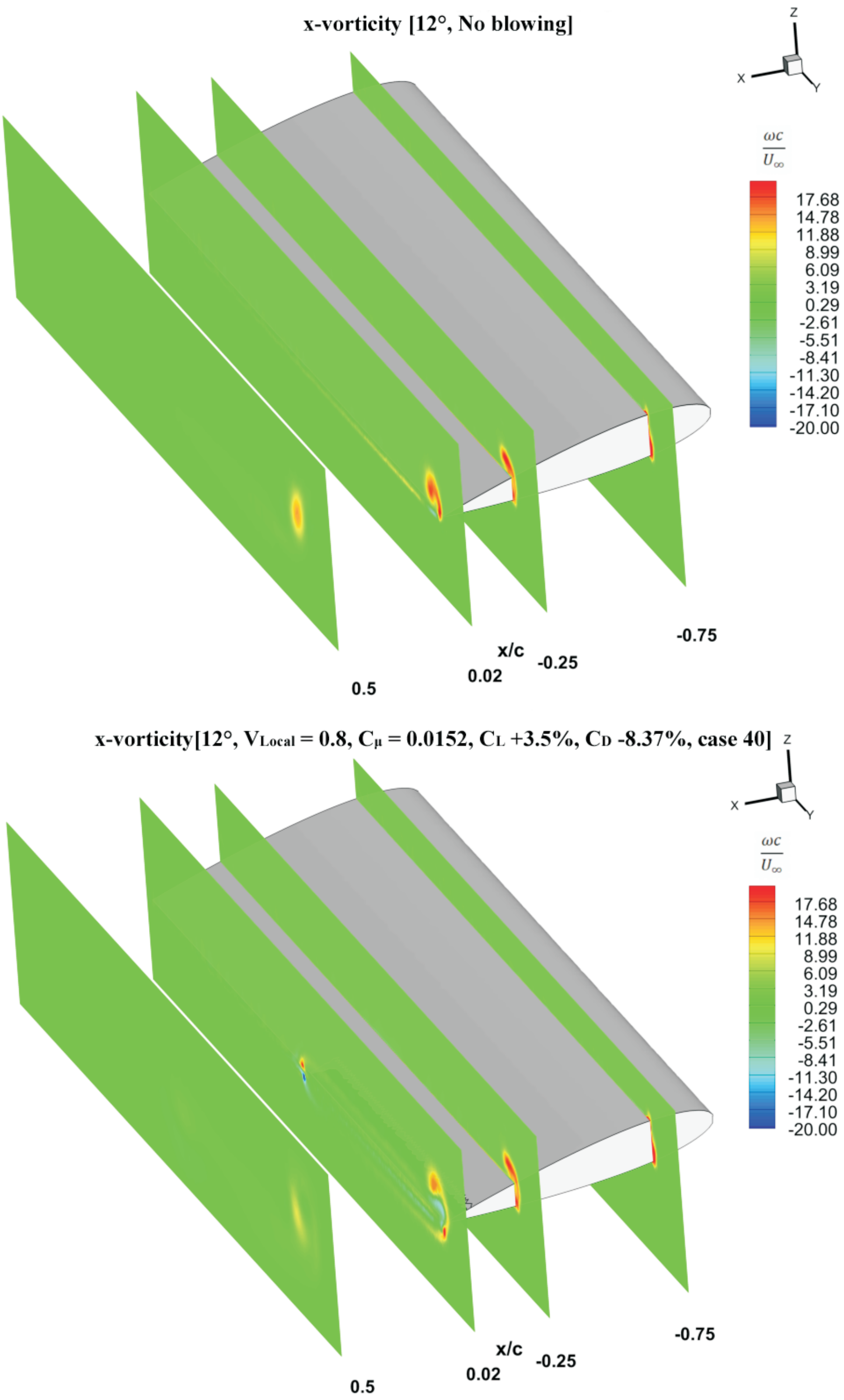

Figure 5.16: x-vorticity along the wing span.

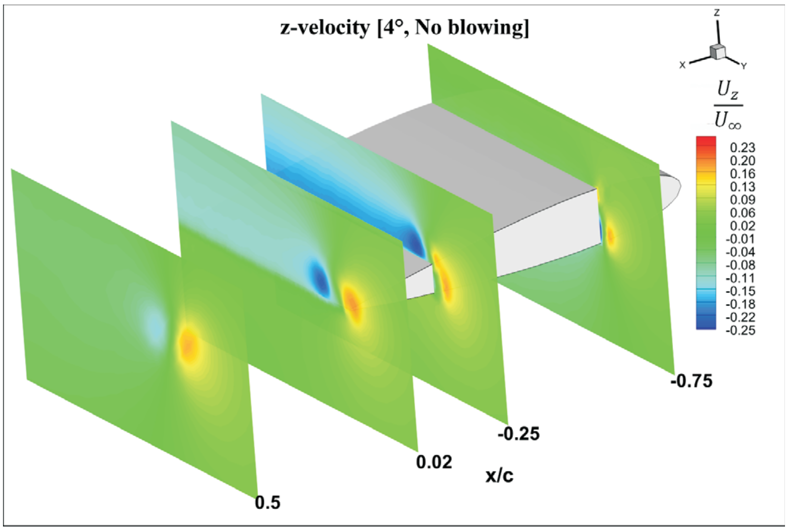

Figure 5.17: z-velocity plot [$\alpha = 4°$, no blowing].

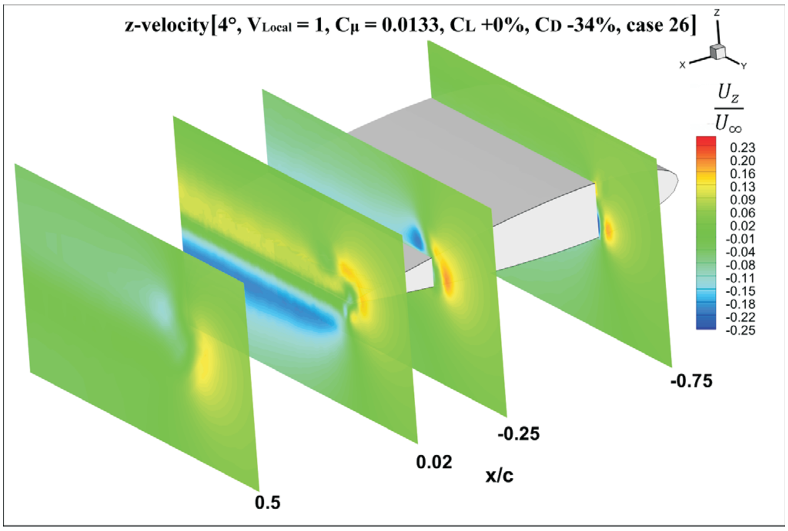

Figure 5.18: z-velocity plot [$\alpha = 4°$, lift stabilized].

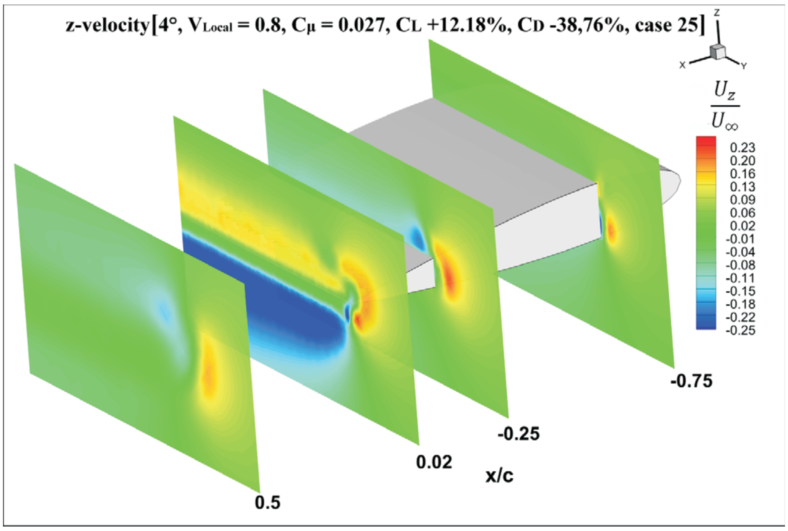

Figure 5.19: z-velocity plot [$\alpha = 4°$, lift maximized].

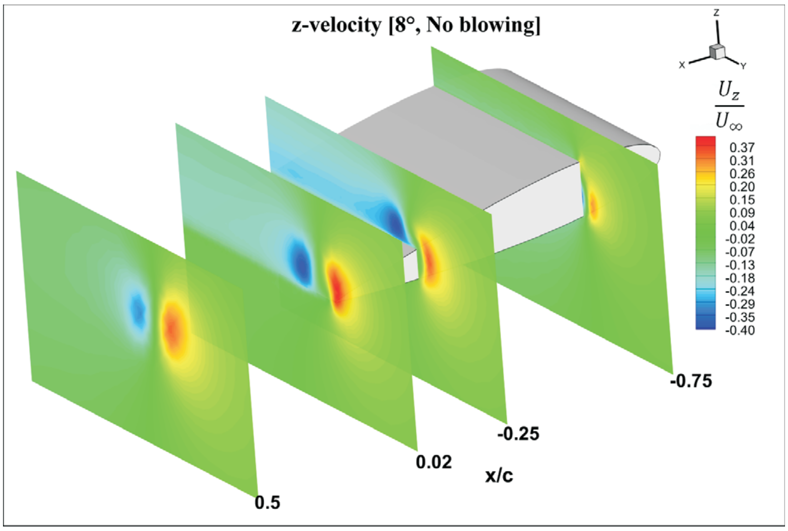

Figure 5.20: z-velocity plot [$\alpha = 8^\circ$, no blowing].

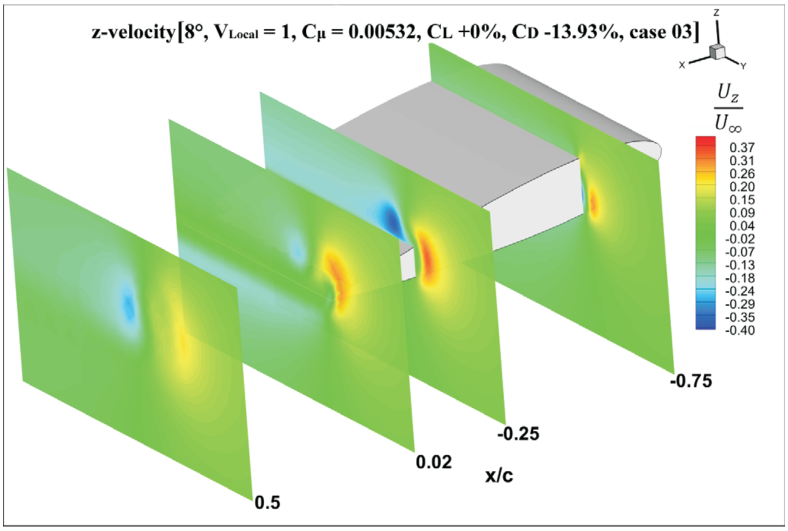

Figure 5.21: z-velocity plot [$\alpha = 8^\circ$, lift stabilized].

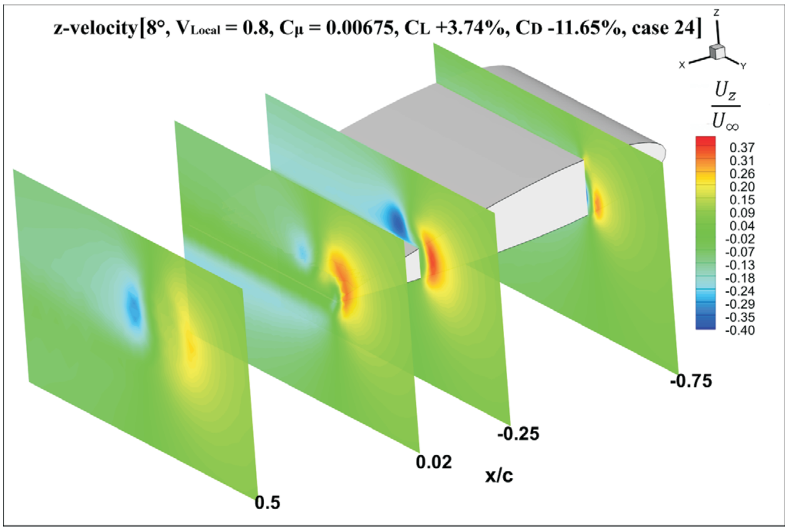

Figure 5.22: z-velocity plot [$\alpha = 8^\circ$, lift maximized].

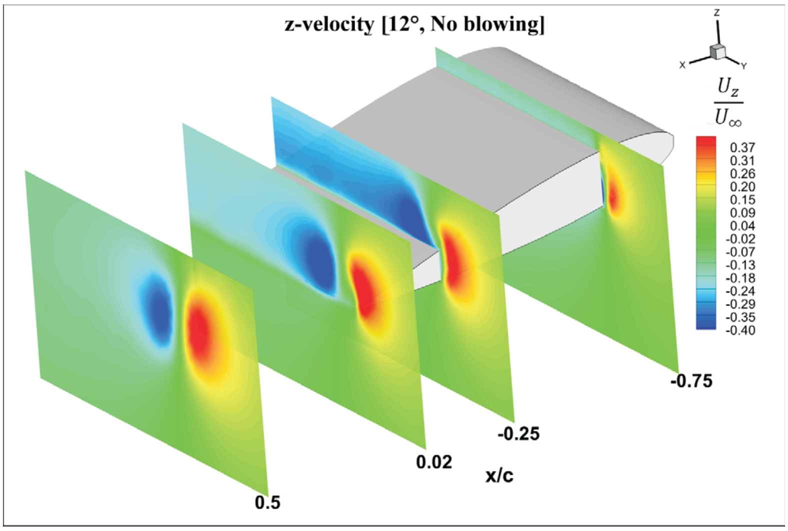

Figure 5.23: z-velocity plot [$\alpha = 12°$, no blowing].

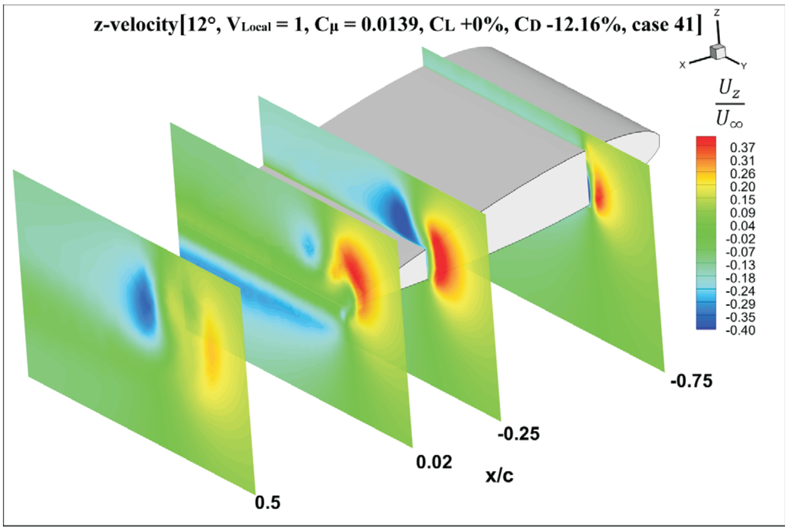

Figure 5.24: z-velocity plot [$\alpha = 12°$, lift stabilized].

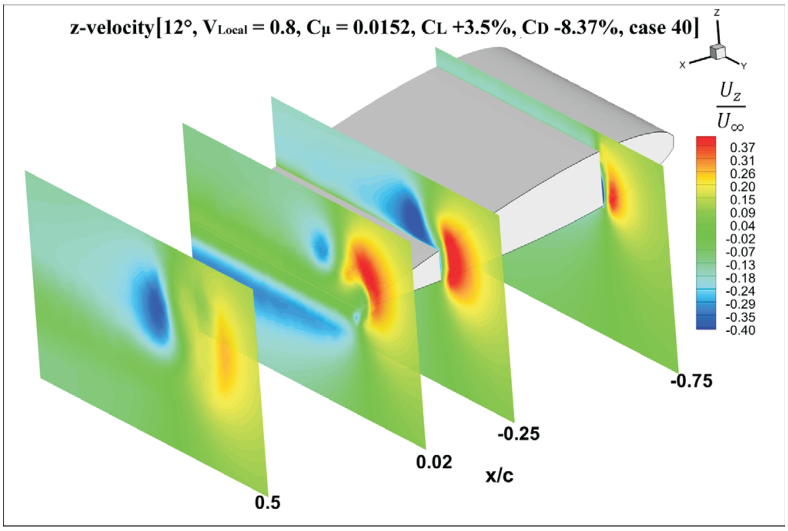

Figure 5.25: z-velocity plot [$\alpha = 12°$, lift maximized].

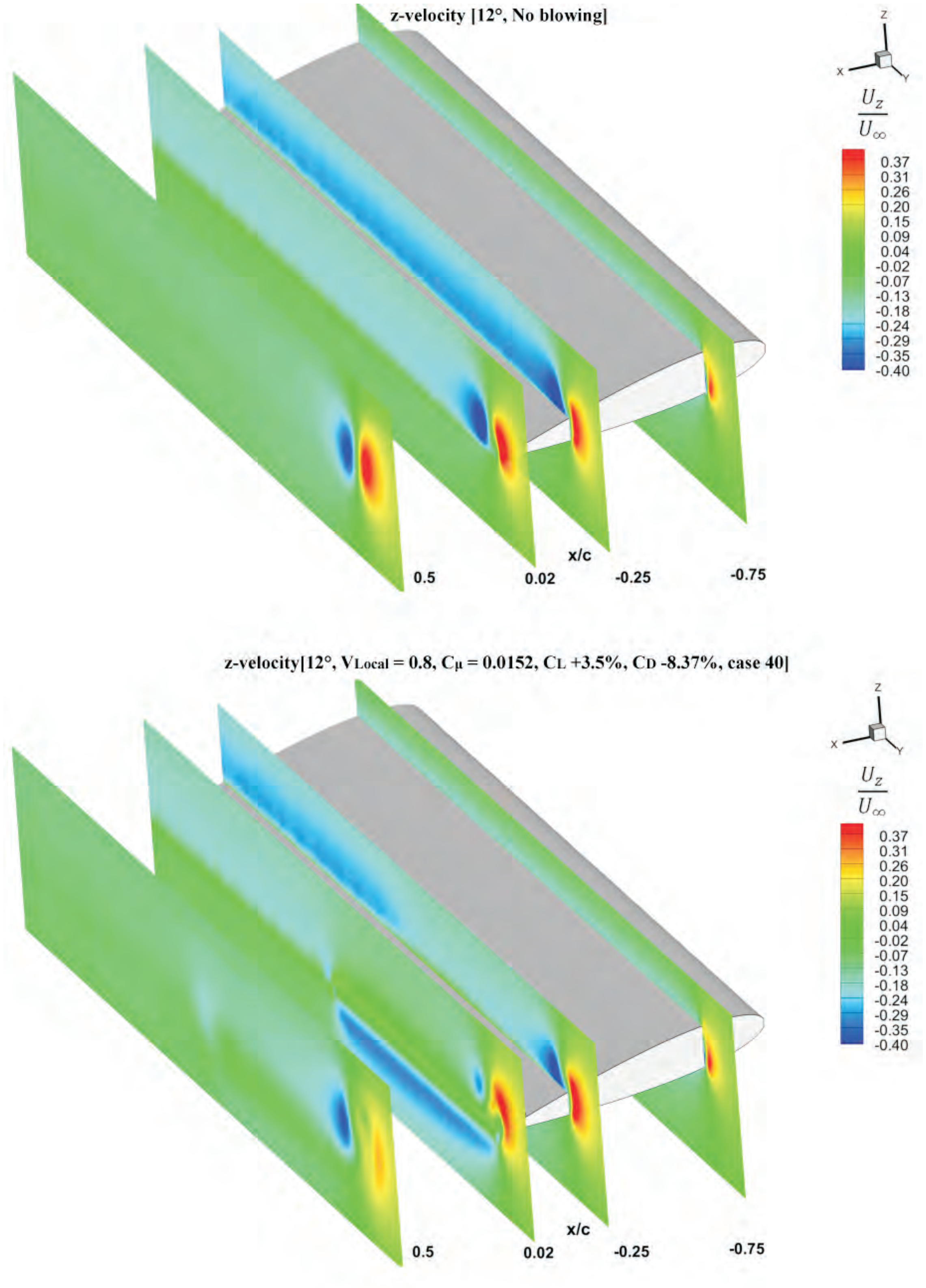

Figure 5.26: z-velocity along the wing span.

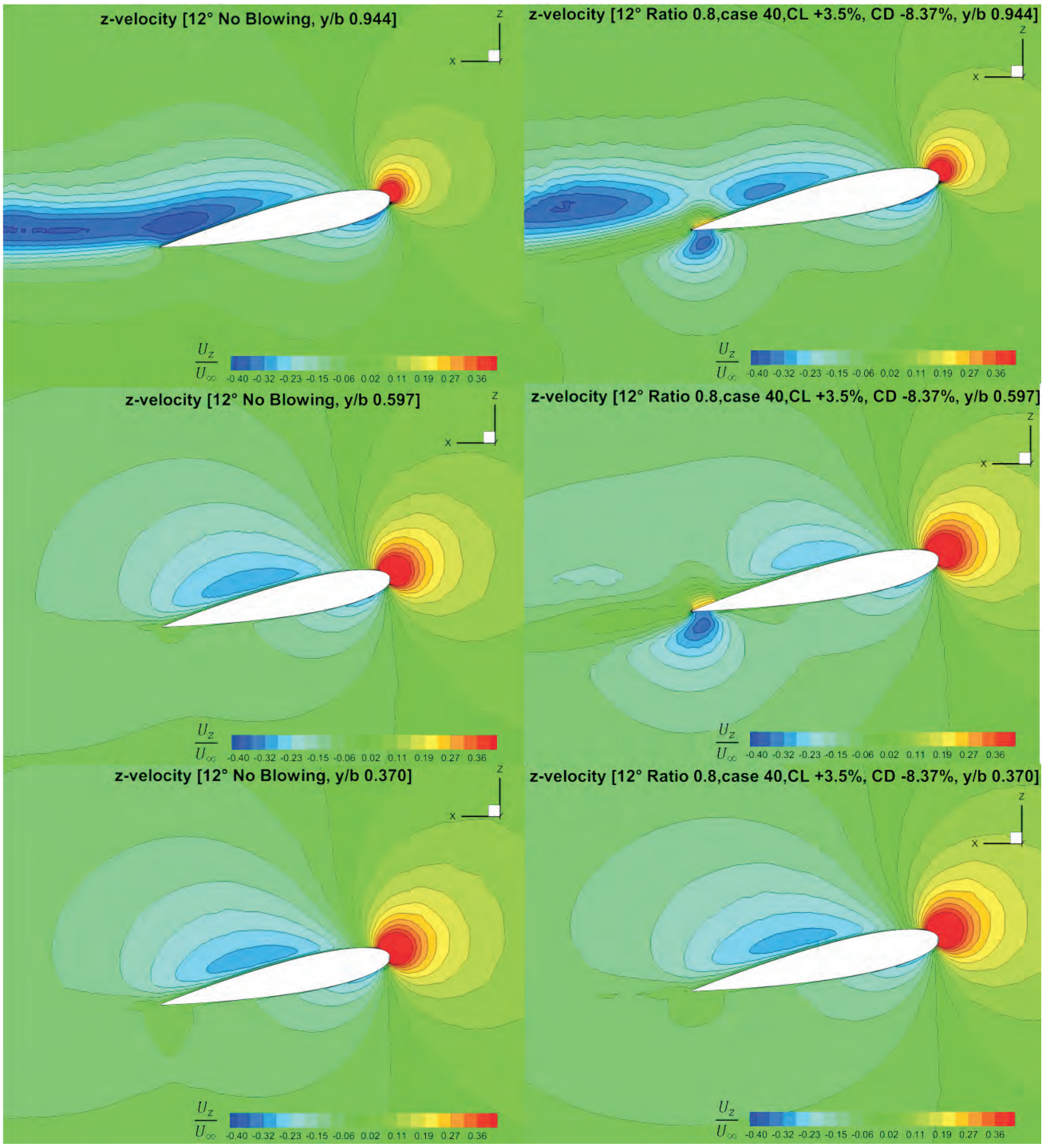

Figure 5.27: z-velocity plot at wing sections.

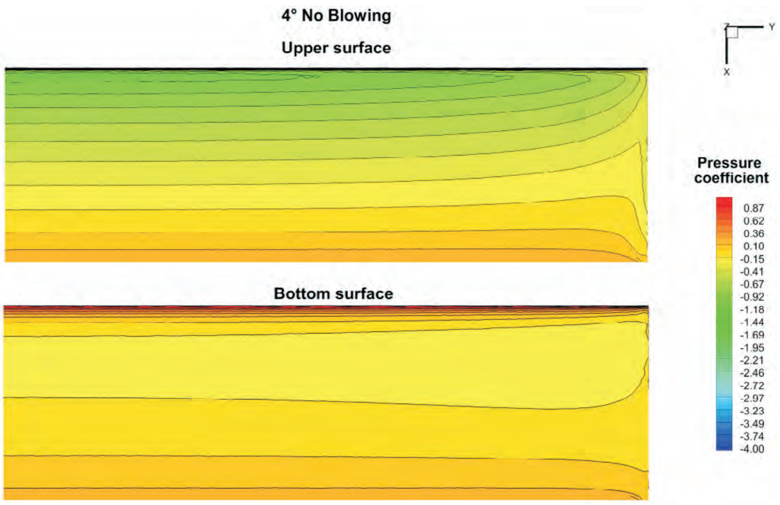

Figure 5.28: Pressure plot [$\alpha = 4^\circ$, no blowing].

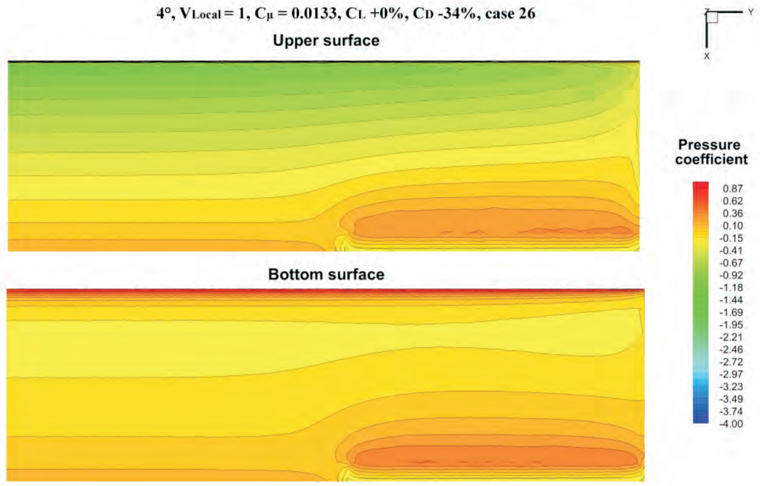

Figure 5.29: Pressure plot [$\alpha = 4^\circ$, lift stabilized].

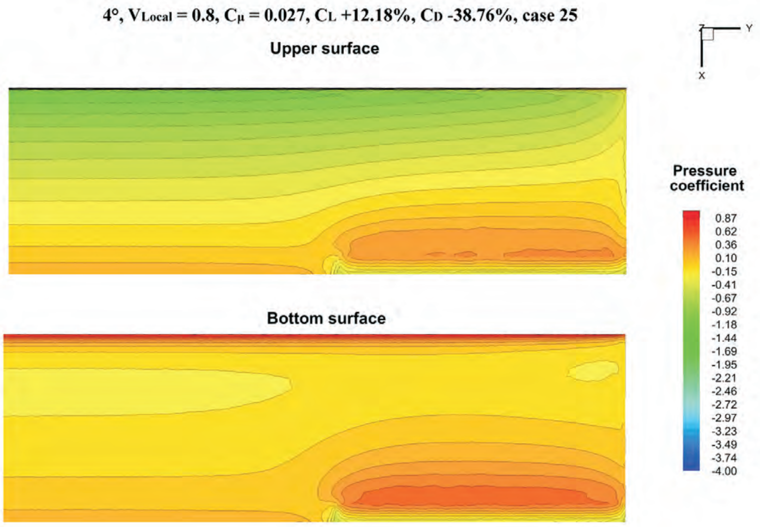

Figure 5.30: Pressure plot [$\alpha = 4^\circ$, lift maximized].

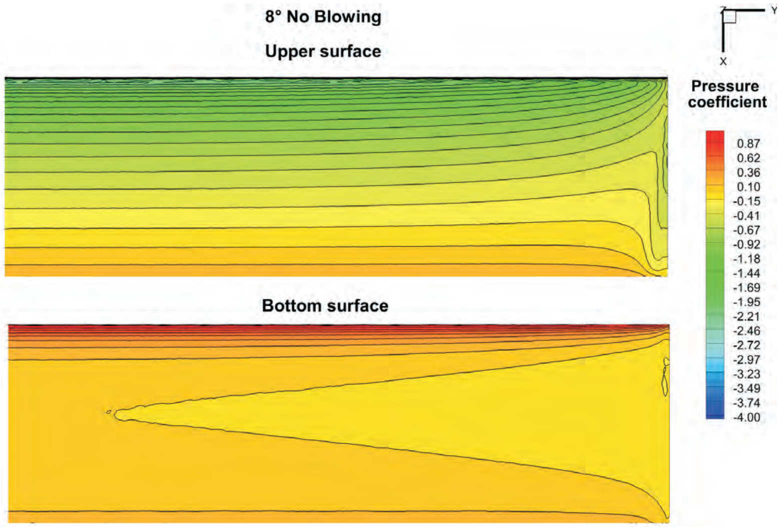

Figure 5.31: Pressure plot [$\alpha = 8^\circ$, no blowing].

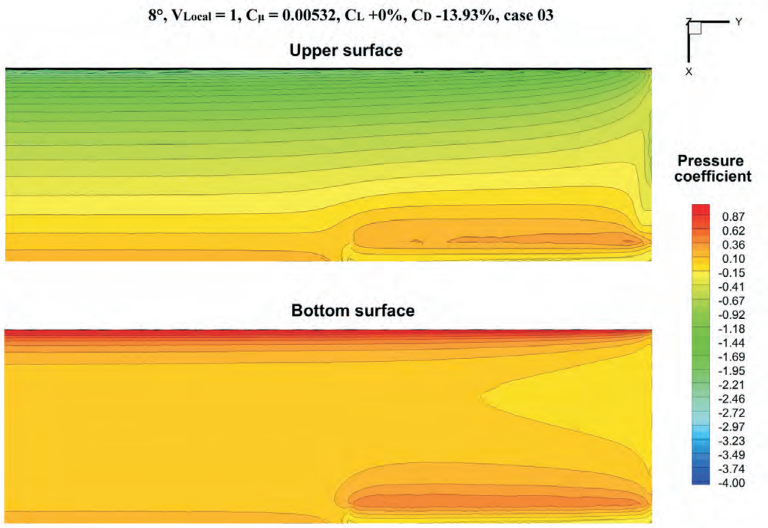

Figure 5.32: Pressure plot [$\alpha = 8^\circ$, lift stabilized].

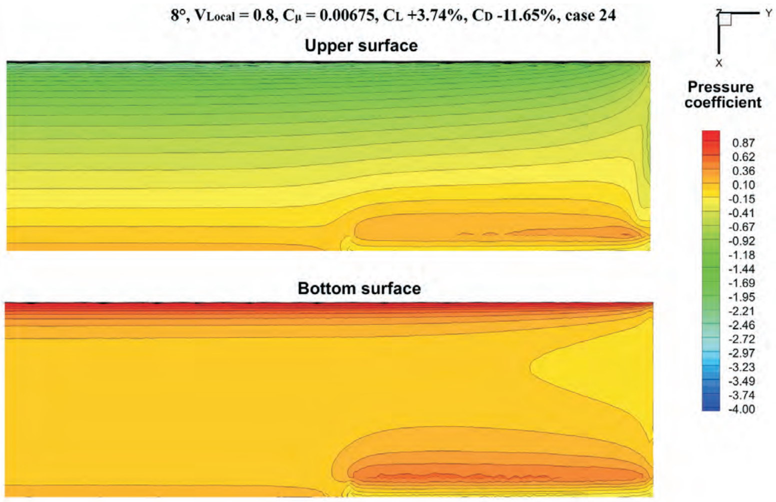

Figure 5.33: Pressure plot [$\alpha = 8^\circ$, lift maximized].

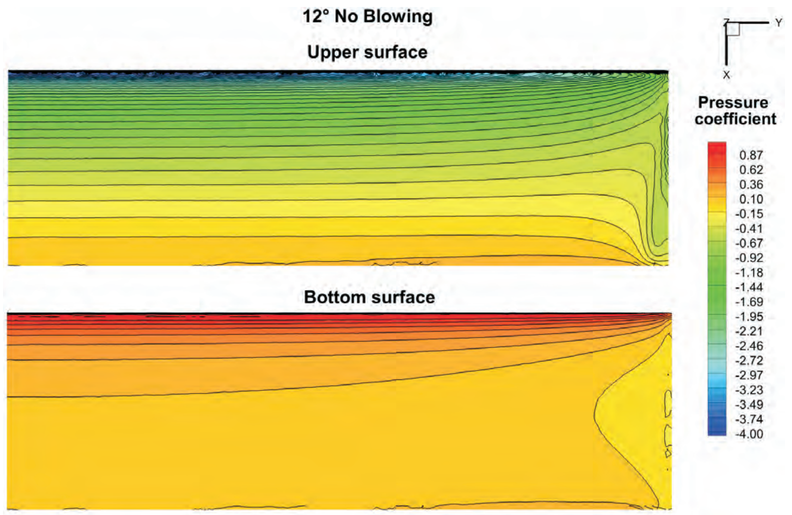

Figure 5.34: Pressure plot [α = 12°, no blowing].

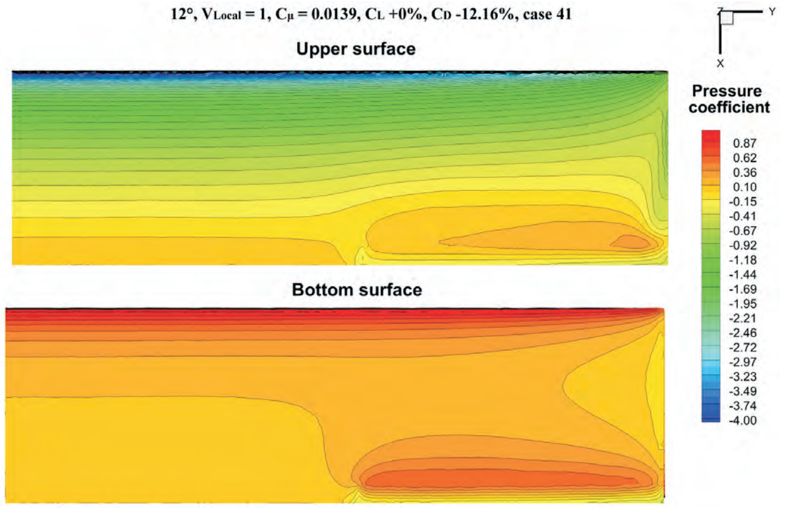

Figure 5.35: Pressure plot [α = 12°, lift stabilized].

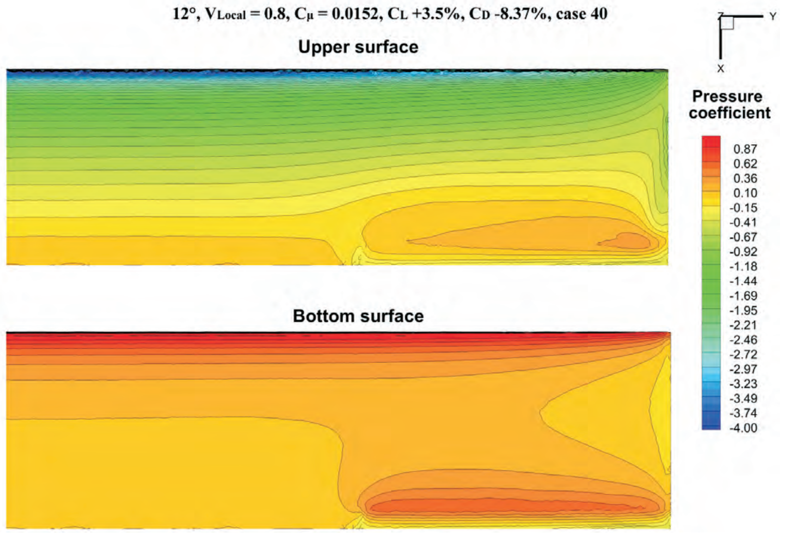

Figure 5.36: Pressure plot [α = 12°, lift maximized].

5.2 Circulation and induced drag

In previous chapters the effects of the AFC device are discussed. It was shown that significant drag reduction is obtained when blowing is applied. However, it is not clear what part of the drag is really reduced. It is well known that the drag is composed from four main parts. Those main parts are form drag, skin friction, lift-induced drag and also interference drag. The observations above could lead directly to the conclusion that a significant part of the drag reduction is due to the reduction of the induced drag or the“tip vortex drag”. This is evident since the vertical velocity at the trailing edge and the peak vorticity close to the tip are significantly reduced. However, at $\alpha = 4^\circ$, it is observed drag decrease close to 38%, which appears to be incredibly high. Therefore, it is important to estimate the induced drag and then evaluate contributions of 2D (skin friction, form drag) and 3D (induced drag) effect on the drag reduction. Generally, there are two methods for calculating the lift-induced drag of a wing, a surface integration method and a wake integration method. In this work the induced drag is computed by the wake integration method. This method, also often referred to as Trefftz-plane analysis [15], quantifies induced drag by extracting flow data from a cut-plane downstream of the wing and perpendicular to the freestream direction. Based on this analysis the induced drag can be estimated as a surface integral:

$$D_i = \int\limits_S \frac{\rho}{2}(v^2 + w^2)dS \tag{5.1}$$

where S is the surface of the slice and v, w the transverse and vertical components of the flow velocity respectively. The induced drag is computed at ten planes in range from 0.5 up to 10 chord’s lengths downstream (see fig. 5.37).

In fig. 5.38 is induced drag plotted at different locations donwstream at $\alpha = 4^\circ$, 8° and 12° natural flow cases. As it can be observed, the induced drag decreases as Trefftz-plane analyses progresses further downstream of the wing. The observed pattern is similar to those ones plotted in the study [22]. Ideally, the induced drag calculation should be independent of the downstream location of the Trefftz-plane. Deviations are caused by several factors. A major effect close to the wing is attributed to the near field. The continued gradual decrease of the drag is due to the numerical dissipation. Also higher-order terms in equations are consequently ignored in many classical Trefftz plane analyses.

For the purpose of comparisons is selected one reference plane at $x/c = 4$ which is far away from the near field and still with low numerical dissipation. Drag computations are conducted in this plane.

In tab. 8 could be found summarized results of Trefftz analysis. It is observed that the induced drag is even higher in the case of lift increase. In fact, the increase in the induced

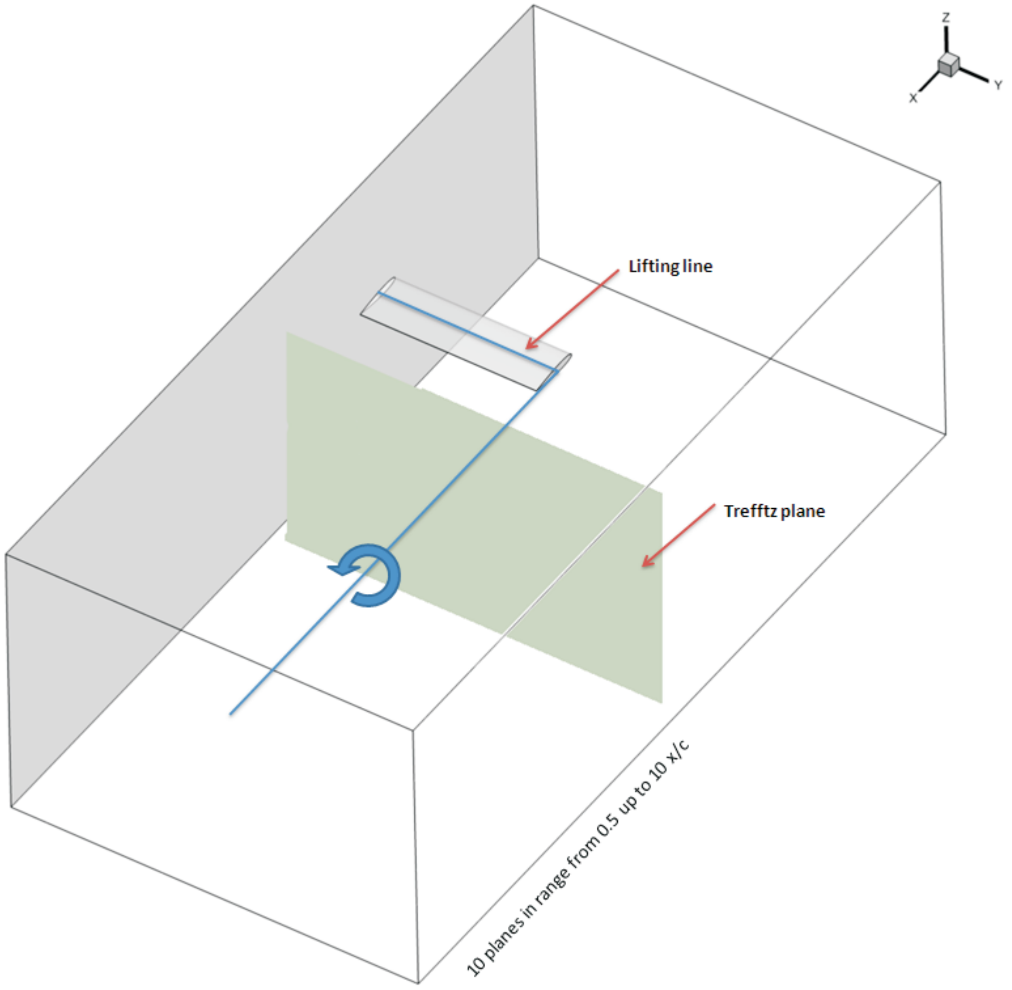

Figure 5.37: Trefftz analysis domain.

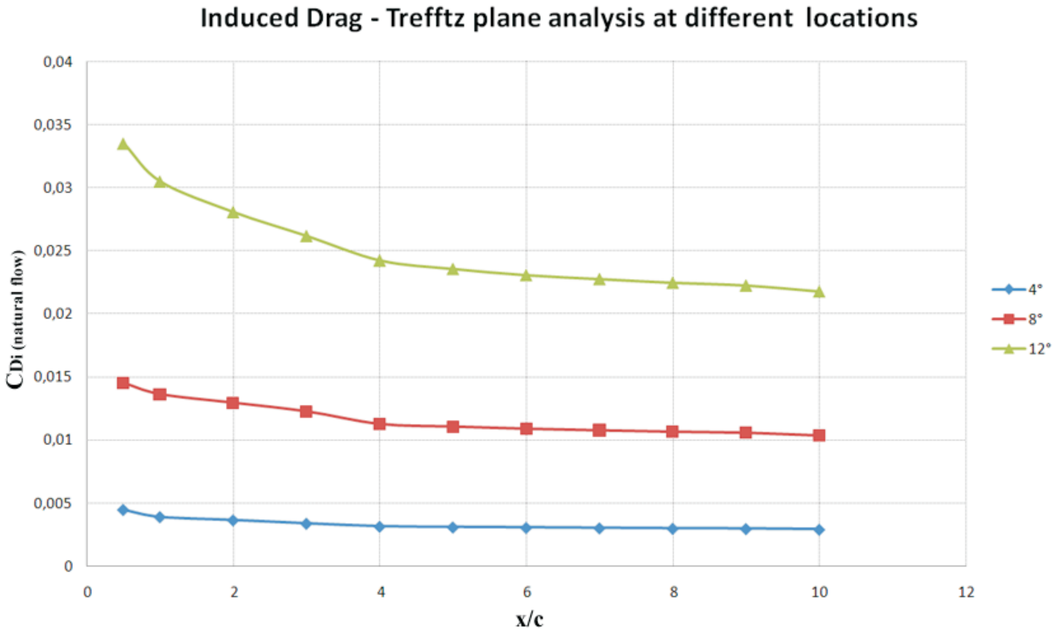

Figure 5.38: Induced drag at different locations.

drag is the result of a trade-off between the reduction of the vorticity close to the tip vortex and the increase in vorticity through the span, because of the local blowing. Indeed, the active control diffuses the main tip vortex structure but increases the total integrated wake drag force. Based on the above observations, it could be stated that the effects of the active flow control are clearly two dimensional.

Tab8: **Induced drag at x/c=4:**

	Total drag		Induced drag	
DEG	No blowing	No blowing	Lift maximized	Lift stabilized
4°	0.0200	0.0031	0.0043	0.0031
8°	0.0369	0.0112	0.0125	0.0112
12°	0.0642	0.0242	0.0265	0.0240

Figure 5.39 plots the induced drag computed at all angles of attack for the natural, and the controlled flow. From the comparisons between the measurements and the computations, it appears that the agreement is quite good. Figure 5.40 plots the percentage of C_{Di} of C_D at $\alpha = 4^\circ$, 8° and 12° for the natural, and the controlled flow. It is well known that the induced drag increases at higher lift coefficients. This trend is observed here, where at $\alpha = 12^\circ$ it accounts up to 45% of the total wing's drag.

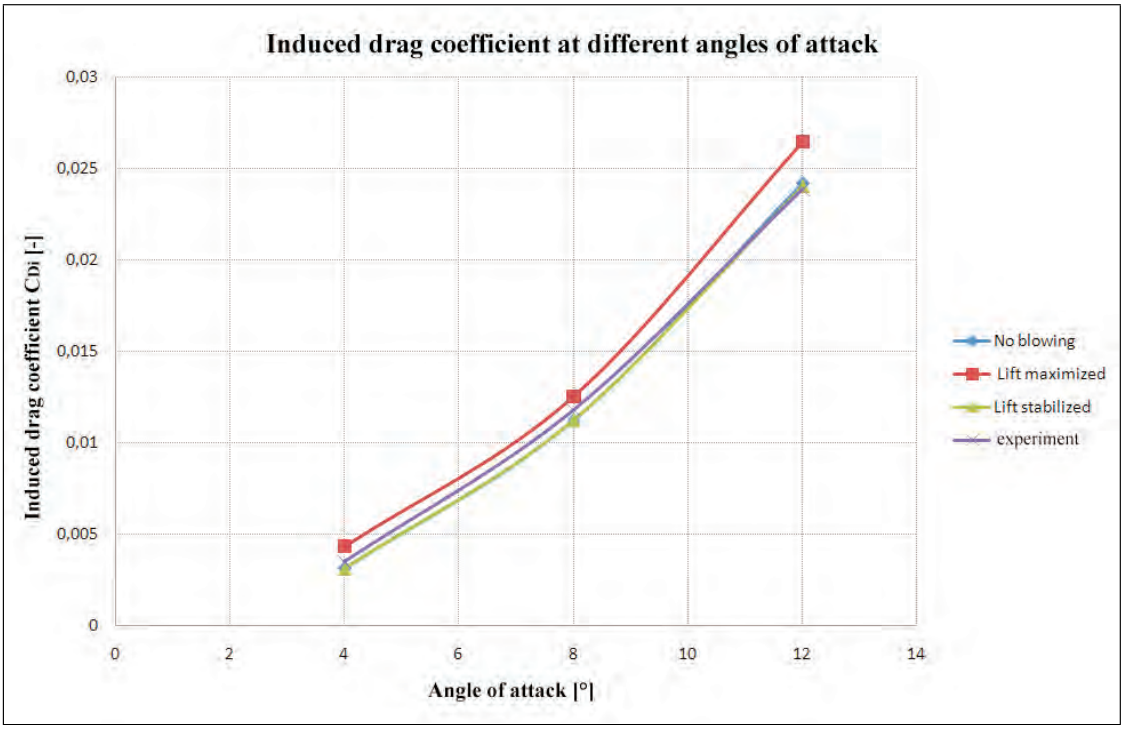

Figure 5.39: Induced drag coefficient at different angles of attack.

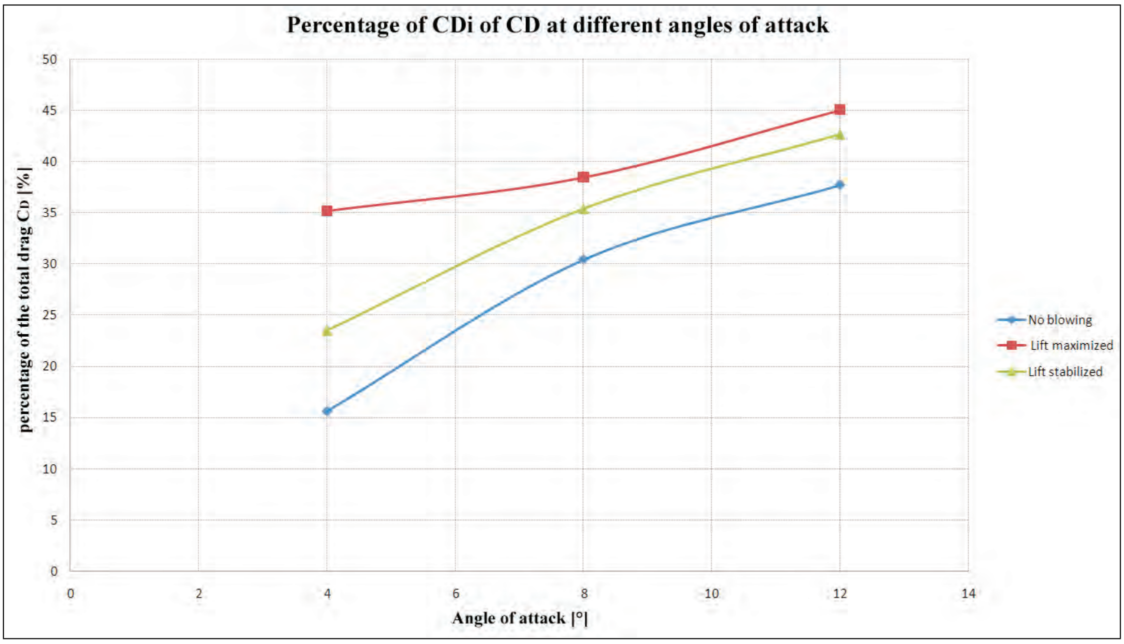

Figure 5.40: Percentage of C_{Di} of C_D

Circulation plots and its development downstream could be observed in fig. 5.42. Circulation is computed at ten planes in range from 0.5 up to 10 chord's lengths downstream for the natural flow cases at $\alpha = 4^\circ$, 8° and 12°. Common decay development is that the decay in vortex circulation is gradual but can also be accelerated by instabilities. The vortex circulation first decays at a relatively small rate, called the turbulent diffusion regime, followed by a rapid decay [9] (see fig. 5.41).

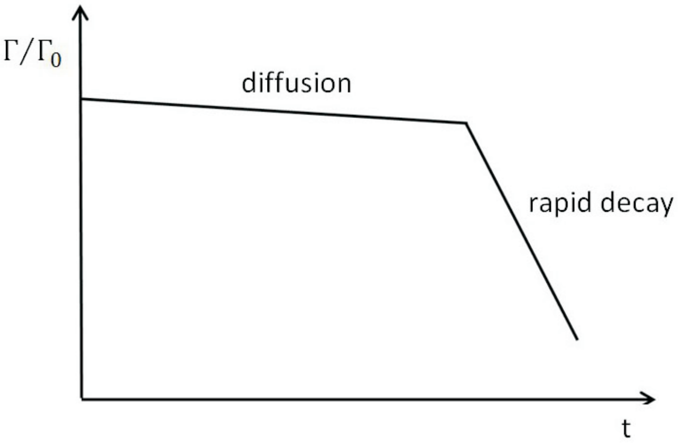

Figure 5.41: Sketch of vortex evolution in terms of circulation versus time.

Circulation can be related to vorticity by Stokes' theorem:

$$\Gamma = \oint_C V dl = \int_S \int \omega dS \tag{5.2}$$

where V is the fluid velocity on a small element of a defined curve, ω is the vorticity, and S is the surface of the slice.

The observations lead to the conclusion that the circulation is stabilized and decay in the turbulent diffusion regime is insignificant within the range from 0.5 up to 10 chord's lengths downstream.

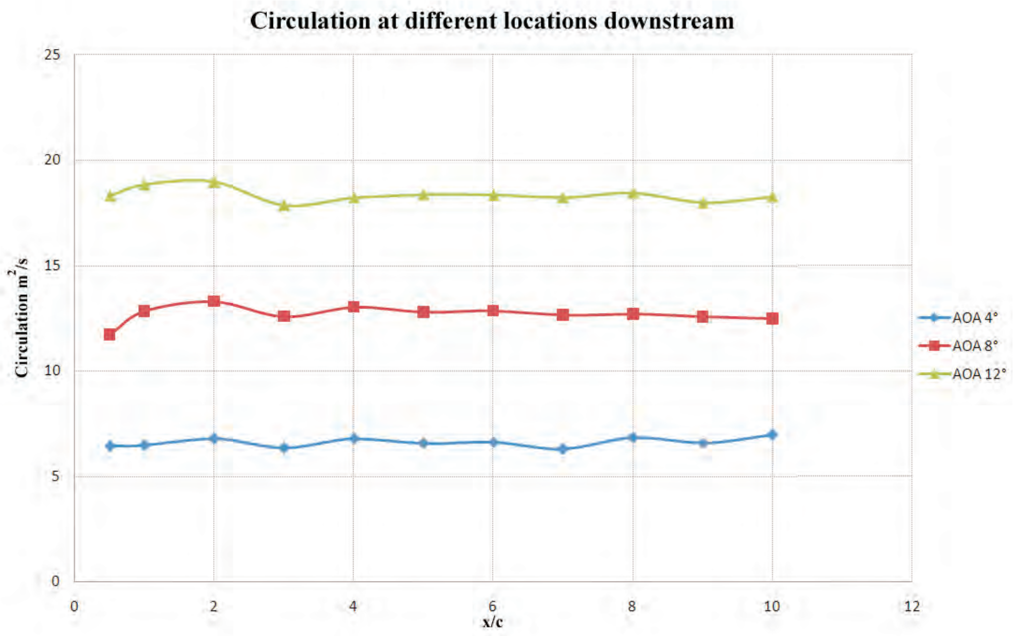

Figure 5.42: Circulation at different locations.

5.3 Aerodynamic performance and loads

The present actuating configuration is examined with the perspective to be capable of reducing the fuel consumption of modern aircrafts and furthermore to replace the conventional control surfaces, thus simplifying the modern aircraft wings. It is important to evaluate aerodynamic performances at different regimes of the blowing. In fig. 5.43 could be seen dependency of C_L,C_D on the global and local velocity ratios on the wing set at $\alpha = 12^\circ$. It could be observed that the device is more effective in terms of drag reduction at higher global velocity ratios and at higher local velocity ratios. However, at high local ratios could be found that lift is very decreased. The lift is getting quite fast into negative gain area at condition $V_{Local} = 1.1$ (more intensive blowing from the upper surface) or higher.

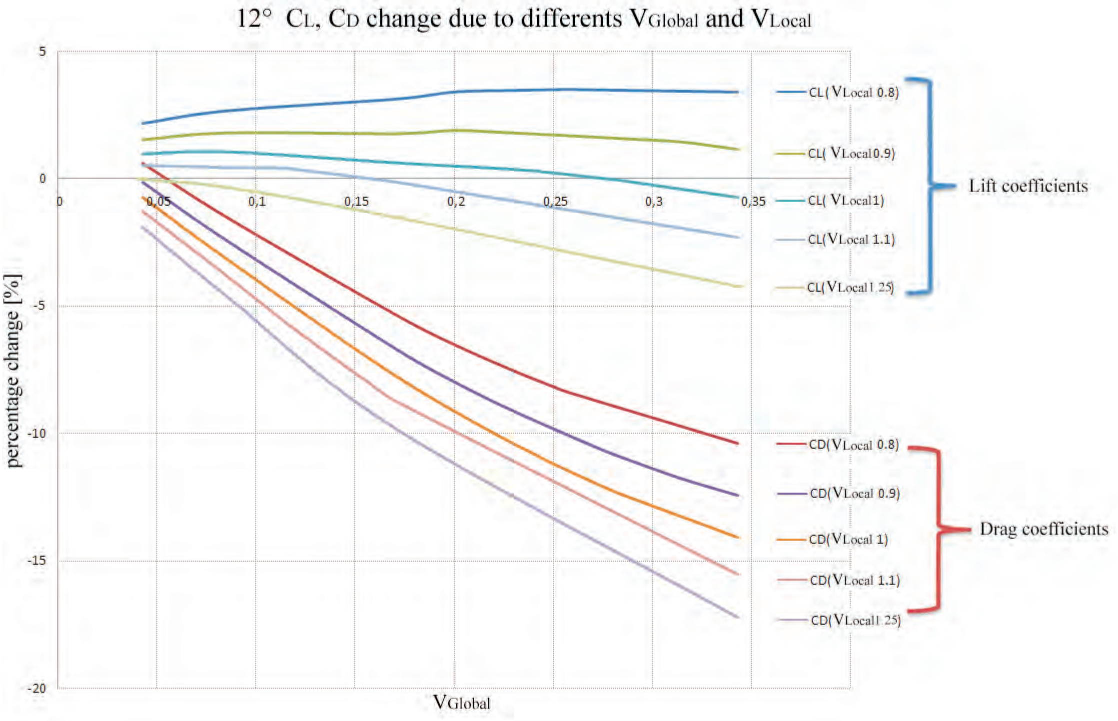

Figure 5.43: Dependency of C_L,C_D

From the computed results can be plotted a lift-drag polar (see fig. 5.44). The drag polar is constructed for the natural flow case and three representative blowing cases. Lift stabilized case represents maximum drag decrease and simultaneous lift stabilization which means that change of the lift is almost zero. Second case, called lift maximized, represents maximum increase of the lift and simultaneous decrease of the drag. Drag minimized case represents maximum drag decrease. In this case, the lift is almost every time lower than in the natural flow case. In this plot can be found interesting behaviour. At higher lift coefficients, new lines are close to the original one. Drag reduction reaches up to 15% at this stage. When lift coefficient is getting lower, it is observed that lines move away. This means that at lower angles of attack the control device is more effective in term of the drag reduction. Reduction of the drag reaches up to 40% with still positive net energy. This conclusion could be a little bit confusing. It is well known that induced drag is higher at higher angles of attack and then the device should have higher impact on the drag at higher angles. However, in the previous chapter 5.2 is shown that main effect of the control device is reducing, so called 2D drag (form+skin friction). Induced drag is almost the same (lift stabilized cases) and even higher in the lift maximized cases. Results which indicate savings around 40% appears to be incredible high and they evoke some criticism. Drag calculated at $\alpha = 4^\circ$ for the natural flow case deviated 122% (tab.2) from the experimental value. However, in the present work comparisons are made directly to the computed natural flow cases thus it should be possible to catch the rate of reduction. Nevertheless, deviations are expected in the drag calculation. Also, it is necessary to mention that conditions of the blowing are absolutely ideal. The slot area is modelled as a top hat velocity inlet boundary condition and blowing is provided steadily from the whole slot's surface.

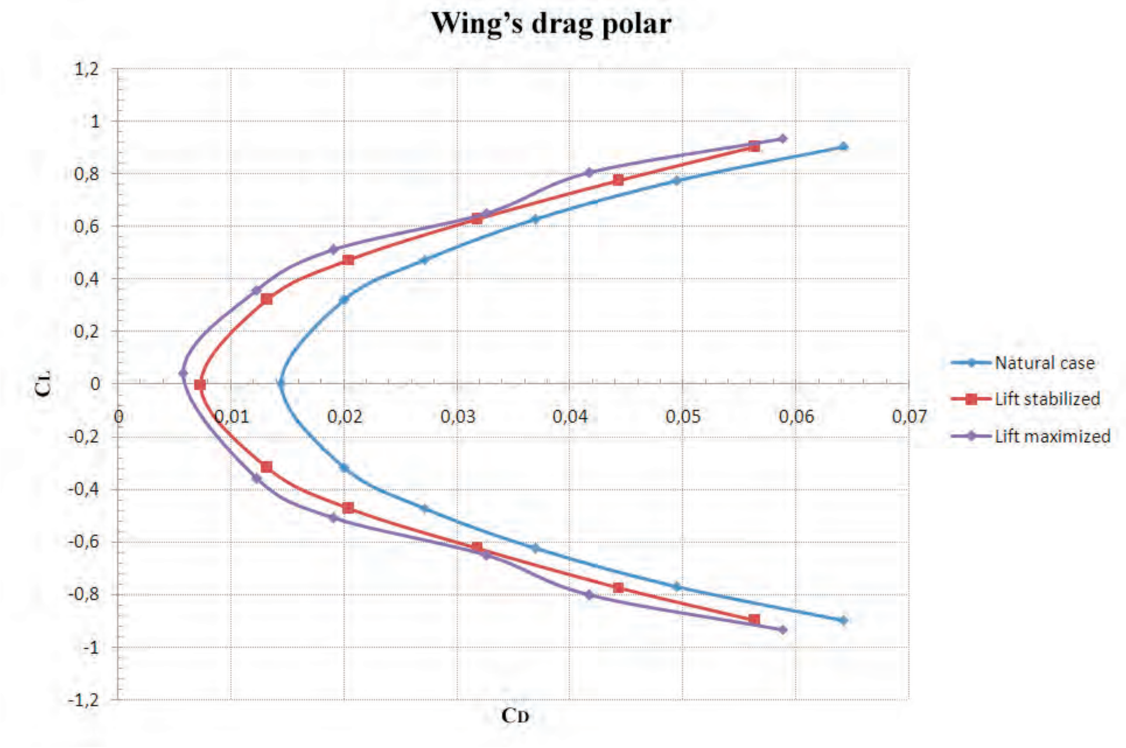

Figure 5.44: Drag polar.

Position of the center of pressure at $\alpha = 4°$ and pitching moment coefficient at $\alpha = 4°$, 8° and 12° for the natural flow cases and representative blowing cases could be found in fig. 5.45 and fig. 5.46. It is observed that position of the center of pressure does not significantly change when the lift stabilized case is used. When blowing is applied at condition of "lift maximized", it could be seen that center of pressure is shifted downstream and towards to the wing tip. The pitching moment coefficient is related to the quarter chord's length. In fig. 5.46 is observed that blowing cases have positive effect on the magnitude of the pitching moment coefficient. This is in agreement with center of pressure plot fig. 5.45. Generally, in the aviation industry an effort is put on to minimize the pitching moment of the wing. Reduction of the pitching moment could be beneficial in many aspects. This could lead into usage of smaller tail surfaces or it could lead to lower negative "tail" lift.

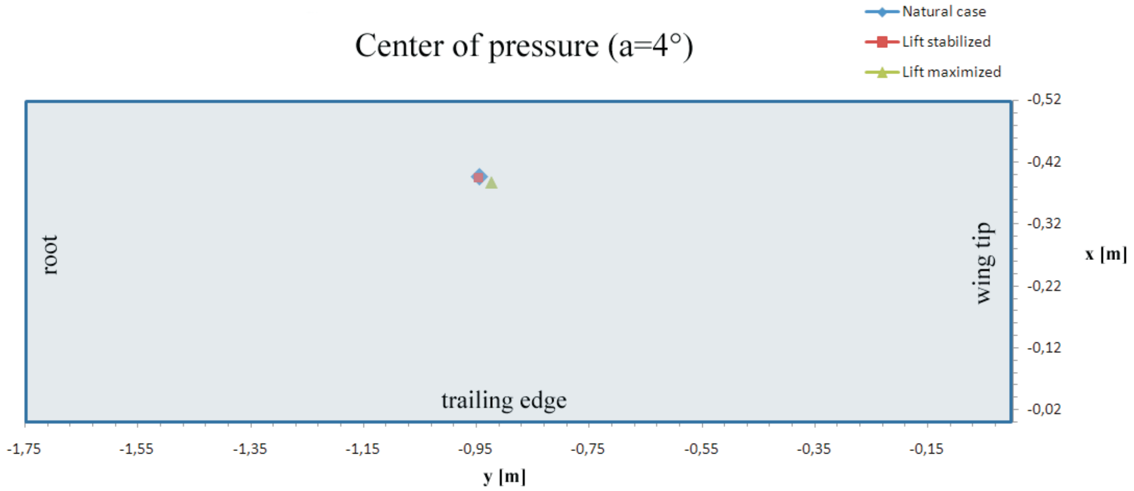

Figure 5.45: Centre of pressure $[\alpha = 4°]$.

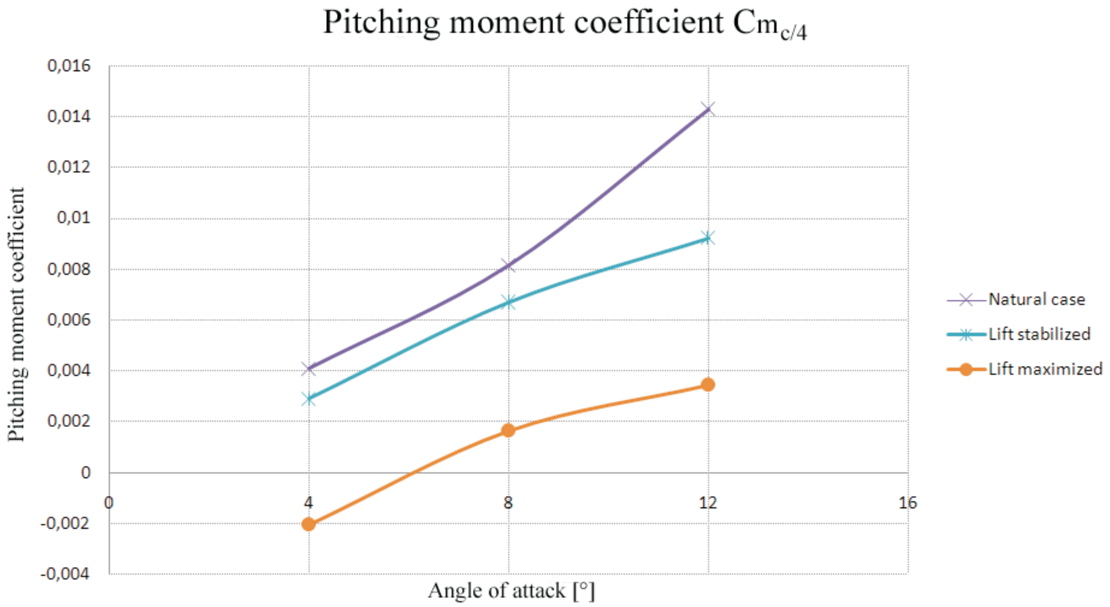

Figure 5.46: Pitching moment coefficient $[\alpha = 4°, \alpha = 8°, \alpha = 12°]$.

Spanwise lift and drag distribution plots are plotted in fig. (5.47 up to 5.50) for the natural and selected blowing cases at $\alpha = 4^\circ$ and 12°. Differences in lift distribution between computed natural flow and experimental lift distribution are in agreement with computed lift coefficient of the wing. At $\alpha = 4^\circ$, the lift coefficient at natural flow case differs from the experimental value about 4%. At $\alpha = 12^\circ$ discrepancy is 13%. At $\alpha = 4^\circ$ and $\alpha = 12^\circ$, the lift stabilized case $(\Delta C_L \approx 0)$ appears to have identical lift distribution with the natural flow. The lift maximized case $(\Delta C_L = +\%)$ keep similar shape of the lift distribution outside of the blowing area at both angles of attack. In affected area by the blowing, the lift distribution is significantly altered and sectional lift coefficient is increased in compare with natural flow case. Increase of the lift towards to the wingtip could have an impact on the structure strength. The shifted distribution causes higher bending moment in the wing's root. Figure 5.49 and 5.50 plots spanwise drag distribution on the wing at $\alpha = 4^\circ$ and 12°. At region which is affected by the blowing (slot area), the sectional drag is decreased. There is found well agreement with experimental drag measurement at $\alpha = 12^\circ$, especially close to the wing tip.

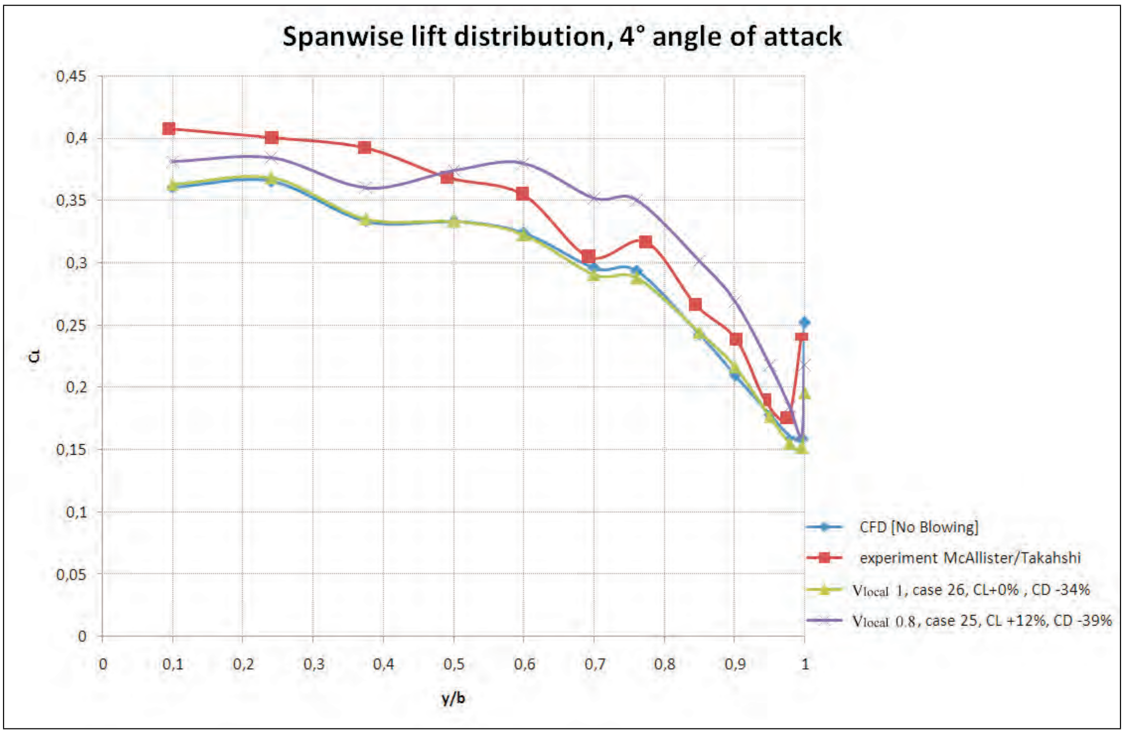

Figure 5.47: Spanwise lift distribution [$\alpha = 4°$].

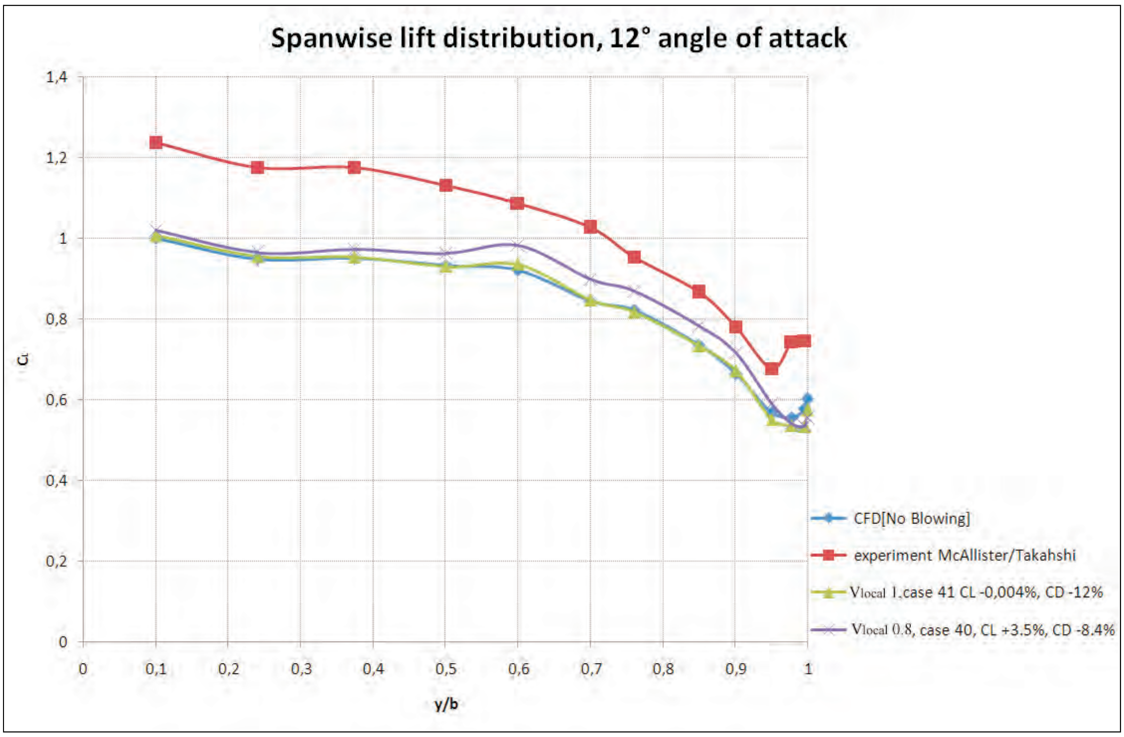

Figure 5.48: Spanwise lift distribution [$\alpha = 12°$].

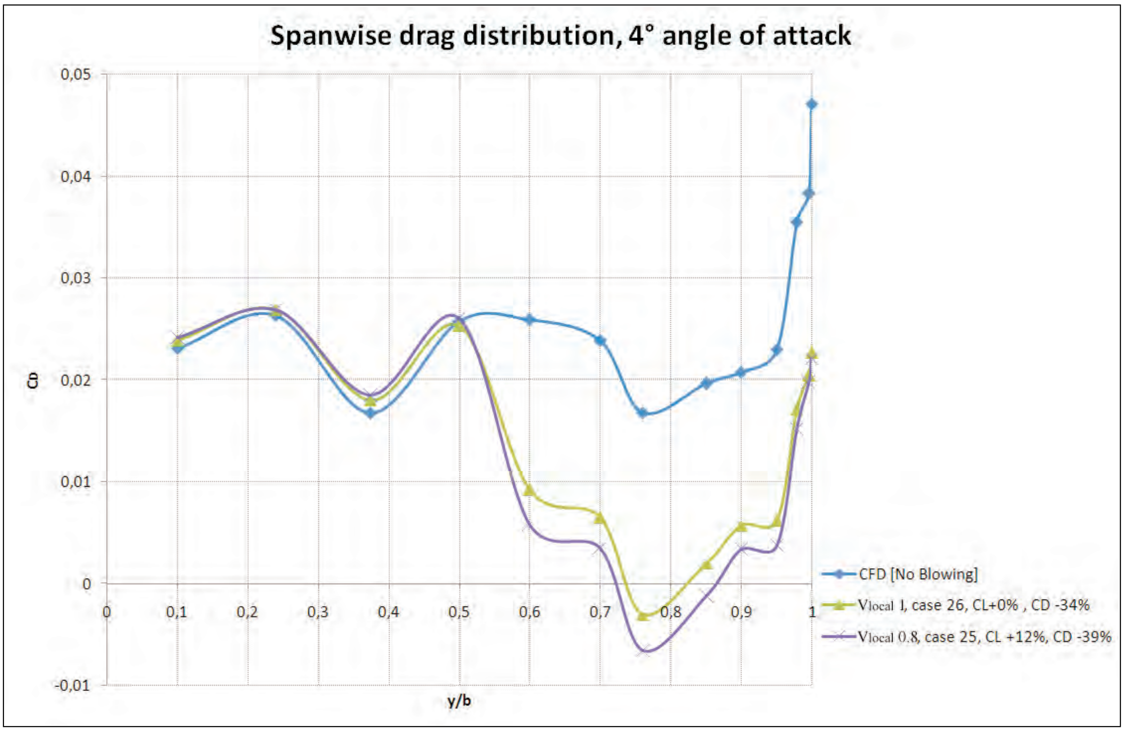

Figure 5.49: Spanwise drag distribution [$\alpha = 4°$].

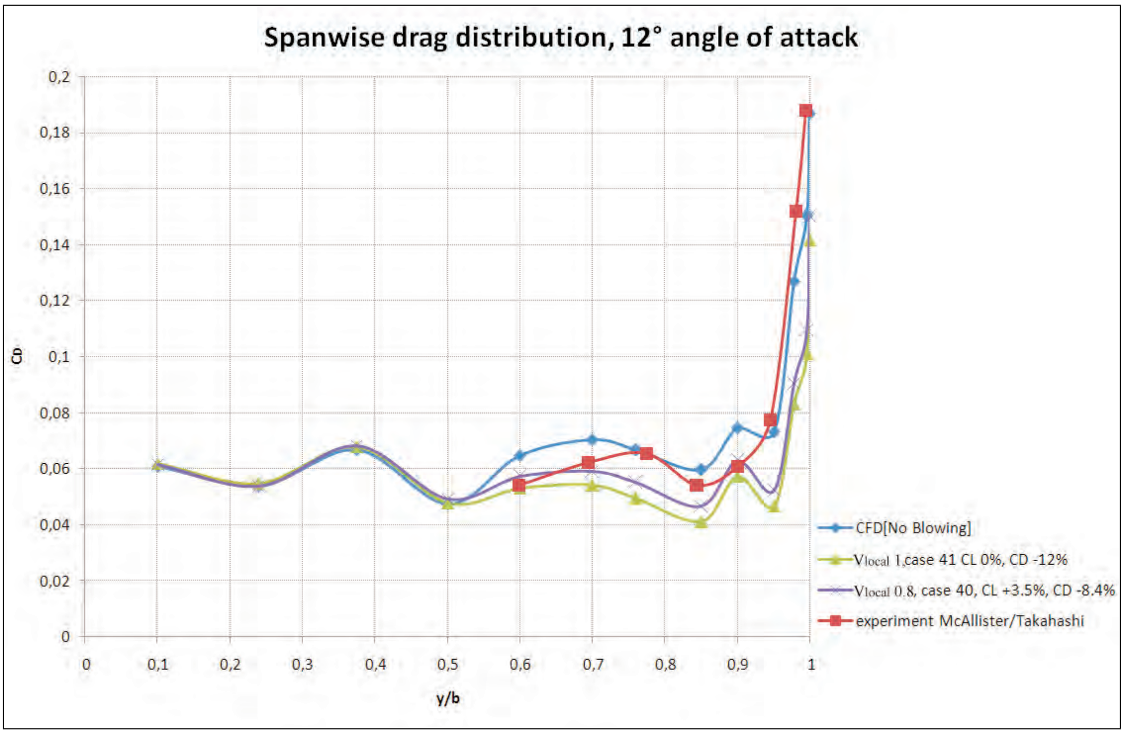

Figure 5.50: Spanwise drag distribution [$\alpha = 12°$].

5.4 Energy efficiency in controlled flow cases

In this chapter the energy efficiency ratio will be thoroughly described, which is one of the main examined parameters in this study. When developing active flow control solutions by using an external energy source, it is necessary to ensure that the system runs efficiently. This means that the energy used to generate the control is less than the energy saved through the aerodynamic drag reduction. The energy efficiency ratio η was formulated in chapter 4.1 as follows:

$$\eta = \frac{P_{Drag\ reduction} - P_{Blowing}}{P_{Drag\ reduction}} \times 100 = \frac{P_{net}}{P_{saved}} \times 100\ [\%]$$

It is defined as the ratio of the net power which is saved from the active control divided by the total saved energy. The most efficient solutions in energy terms are those with η close to 100%. Energy efficiency ratio at the vast majority of the examined cases is positive, which means that always the blowing energy was lower than the gained energy from the drag reduction. The energy savings and demands are evaluated in accordance with reference [28]. The energy saved through aerodynamic drag reduction can be described as follow:

$$P_{Drag\ reduction} = \Delta F_x u_\infty \tag{5.3}$$

where ΔF_x is the drag reduction induced by the blowing and u_∞ the free-stream velocity. The energy used to generate the control is defined as:

$$P_{Blowing} = K \frac{\rho u_{bl}^3 A_{bl}}{2} \tag{5.4}$$

where u_{bl} denotes the blowing velocity of the surface, A_{bl} the total surface of the blowing slot, ρ density of air, and K represents total internal losses. For reasons of simplicity and uncertainty in the design of the actuation set-up, K equals to 1. It is considered that in the circuit there is an ideal pump and the demanding energy for blowing equals to the produced energy from the pump.

In fig. (5.51 and 5.52) change of the energy efficiency ratio is plotted with respect to the change of the lift and drag coefficient at $\alpha = 4^\circ$ and 12°. It is observed that better energy efficiency in terms of the drag reduction is obtained at higher local velocity ratio. For instance, in plot 5.51 at $\alpha = 4^\circ$ the energy efficiency ratio could be observed for a drag reduction of 30%. At condition of $V_{Local} = 1.25$, η equals to 85%, at $V_{Local} = 0.8$, η equals to 58%. This trend is more pronounced at 12° where the energy efficiency ratio for the drag reduction e.g. of 10% is: $\eta = 93\%$ at $V_{Local} = 1.25$ and $\eta = 28\%$ at $V_{Local} = 0.8$. Those results obtained at $V_{Local} = 1.25$ could appear promising. However, the lift is greatly decreased if the flow control device operates at higher V_{Local} ratio than 1. Due to this fact, it is necessary to account the effect of the lift. In fig. (5.53 up to 5.55) is plotted energy efficiency at $\alpha = 4°$,$\alpha = 8°$ and $\alpha = 12°$. Higher or more favorable C_L/C_D ratio is typically one of the major goals in aircraft design, since a particular aircraft's required lift is set by its weight and delivering that lift with lower drag leads directly to better fuel economy, climb performance, and glide ratio. Figure 5.53 plots energy efficiency at $\alpha = 4°$. This flight regime at $\alpha = 4°$ commonly corresponds to a cruise condition. An airplane spends the most of the time in air in cruise regime. In this flight regime it is possible to achieve an increase of C_L/C_D from 16 up to 27 with efficiency around 50%. In case at $\alpha = 4°$, the green line corresponds to $V_{Local} = 1.25$ and it offers the worst performance in comparison with others. However, situation changes at higher angles of attack. In fig. 5.54 and 5.55 could be found that $V_{Local} = 1.25$ offers the best energy efficiency with almost the same performance as the other blowing conditions. Those facts lead to a conclusion that at cruise condition could be more favourable to operate at $V_{Local} = 1$. At higher angles of attack it is better to operate at $V_{Local} = 1.25$.

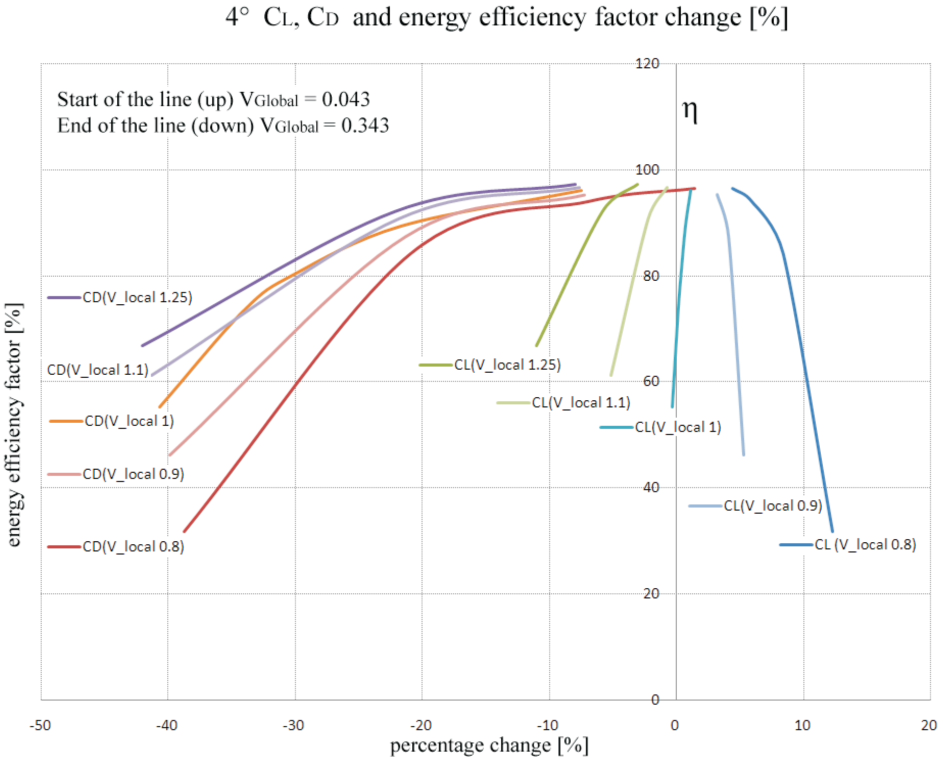

Figure 5.51: $\alpha = 4° C_L, C_D$ and energy efficiency ratio change [%].

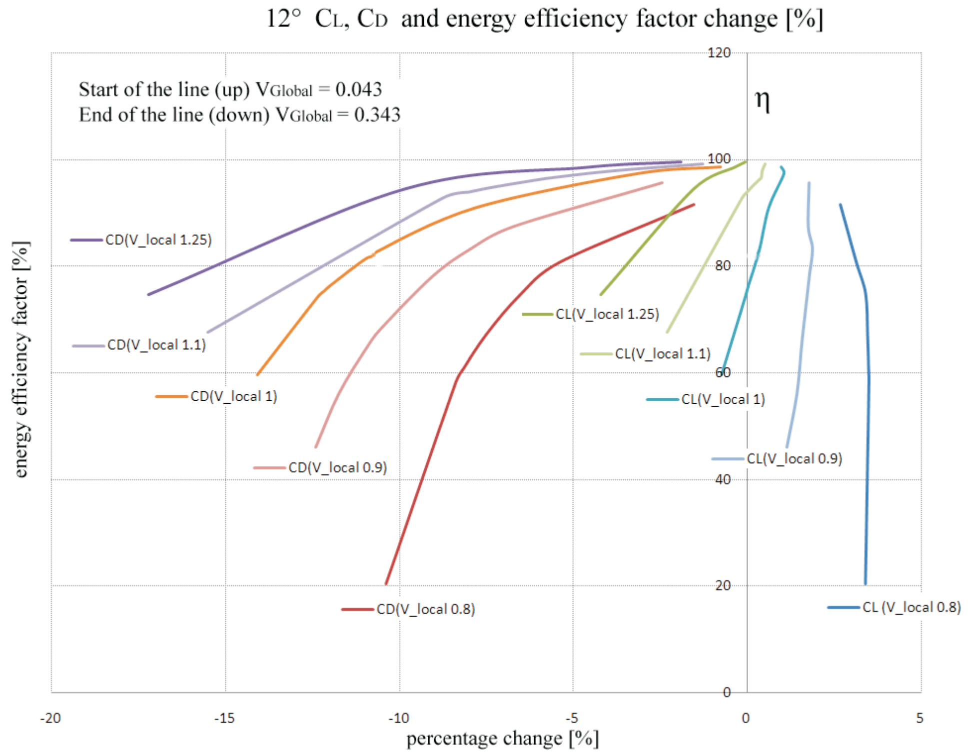

Figure 5.52: $\alpha = 12° C_L, C_D$ and energy efficiency ratio change [%].

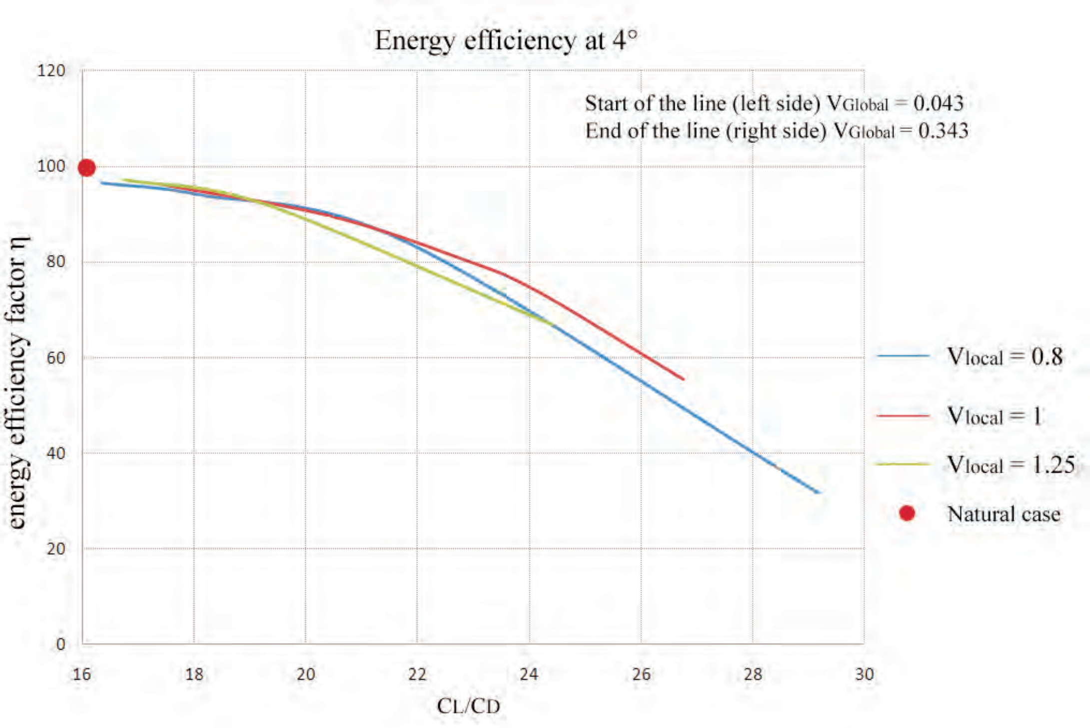

Figure 5.53: Energy efficiency [$\alpha = 4°$].

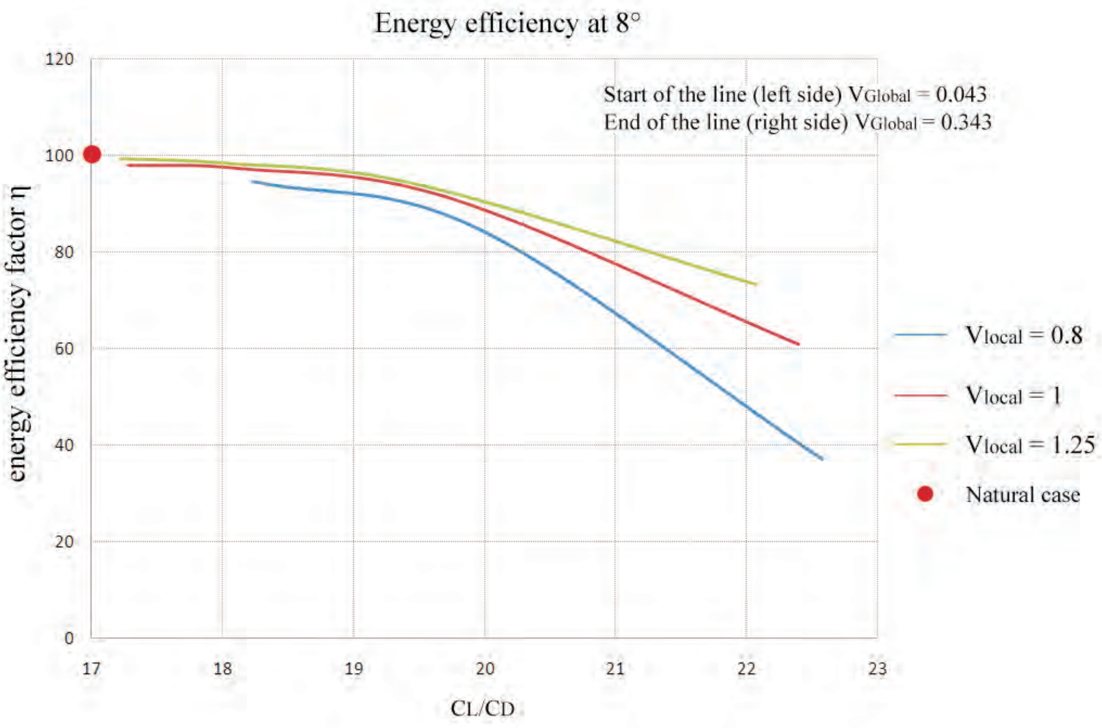

Figure 5.54: Energy efficiency [$\alpha = 8°$].

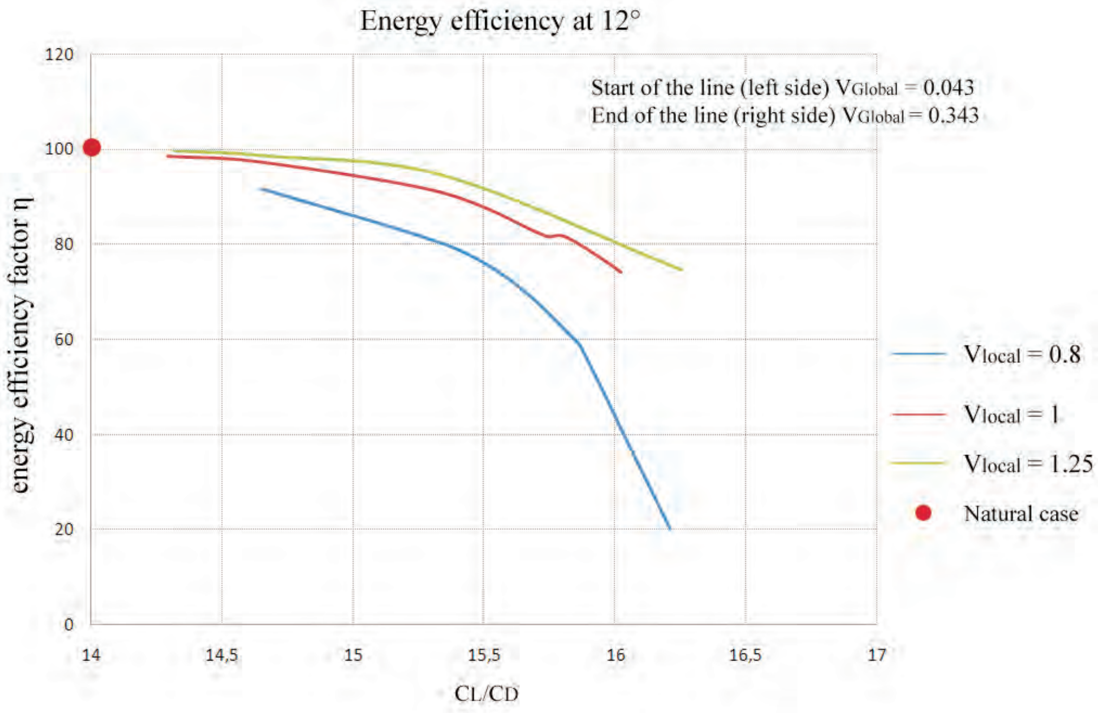

Figure 5.55: Energy efficiency [$\alpha = 12°$].

6 Implementation of the outcome of solution

6.1 Analysis of dependencies

This chapter provides the basic optimization of the performance of the AFC device. It is observed change of the performance of the device as the device is shifted to other position onto the wing. Various configurations are tested in order to show that proposed device is capable to be implemented on the current configurations of airplanes. Tested cases include different size of the slots, an inward location on the wing and different inclination of the jets. Dependence of the overall performance on the magnitude of blowing velocity has been already explored in section 5.3.

6.1.1 Position of the slot on the wing chord

The trailing edge and its low construction height could cause problems when designing such a device. It could be advantageous to shift the device upstream onto the wing. In fig. 6.1, it could be seen that four positions are tested. Each configuration has its own number and it has exactly the same size. In fig. 6.2 and 6.3 significant effects on the drag and lift forces are observed. Percentage change value equals to the normalized change of the force computed in the natural flow case. It could be observed that as the slot moves farther from the trailing edge, the device's performance is worse.

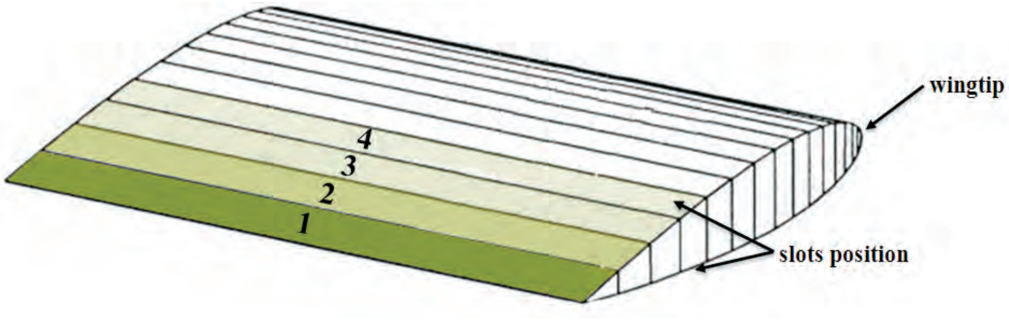

Figure 6.1: Sketch of position of the slots.

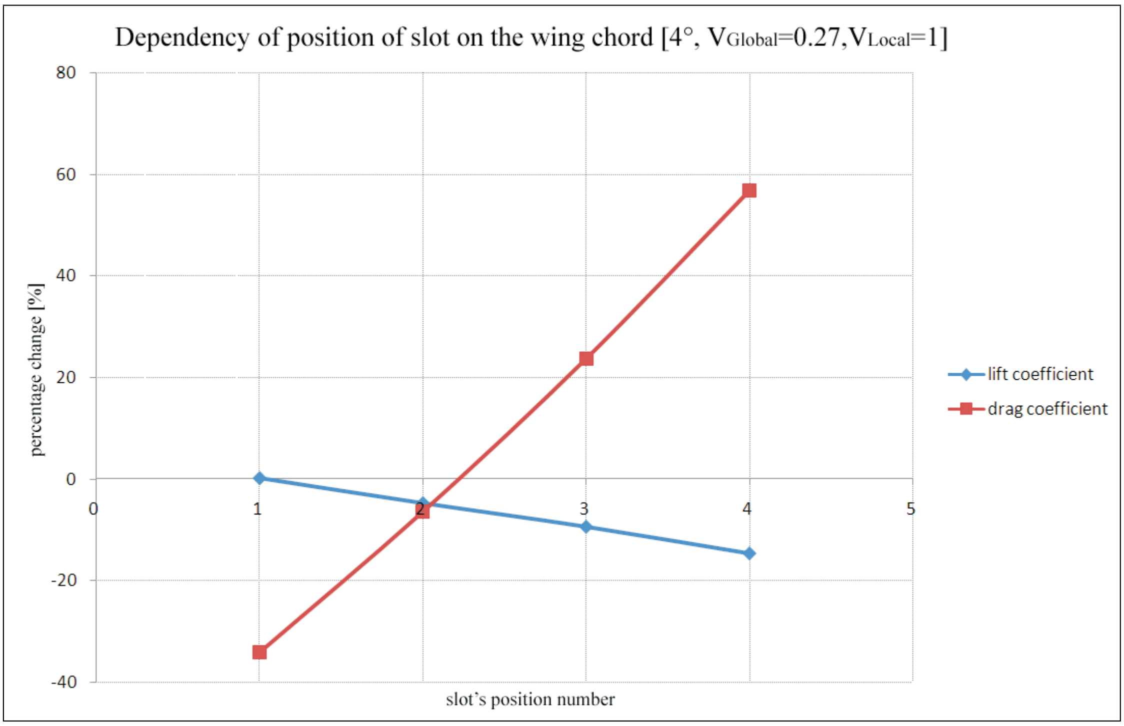

Figure 6.2: Dependence on the position of the slot[$\alpha = 4^{\circ}, V_{Global} = 0.27, V_{Local} = 1$].

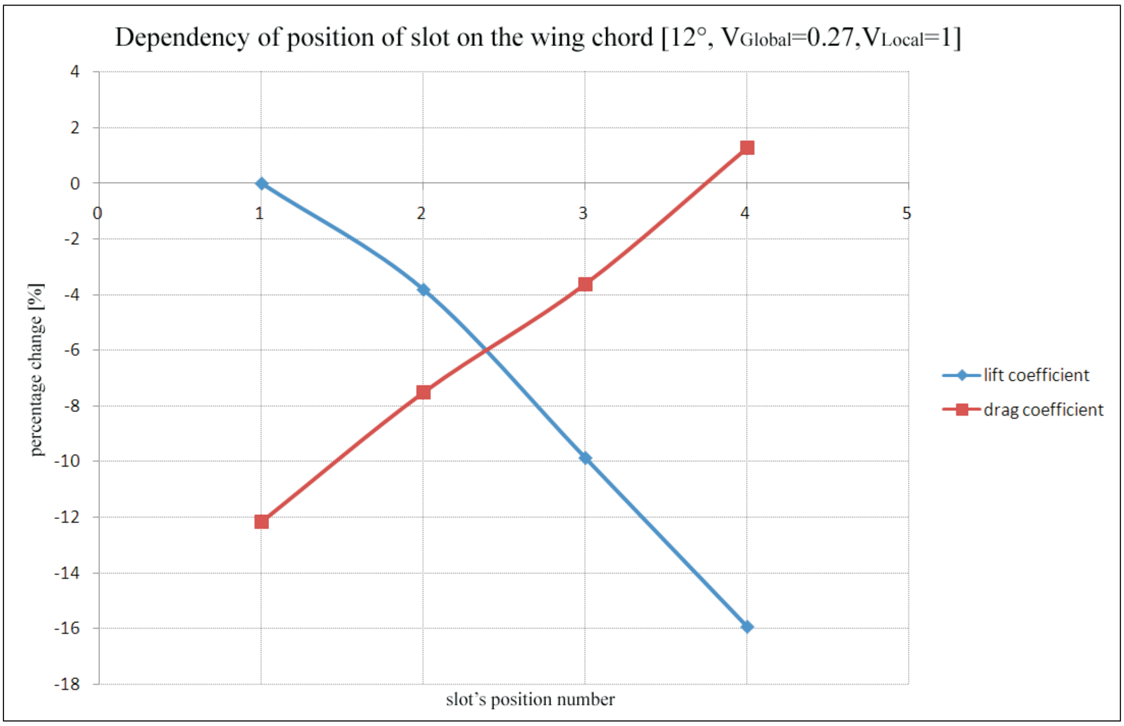

Figure 6.3: Dependence on the position of the slot[$\alpha = 12^{\circ}, V_{Global} = 0.27, V_{Local} = 1$].

6.1.2 Inclination of the jet flow

In the present study, the angle of blowing is restricted only to 90° which means that the jet flow is always parallel to the z-axis. However, it could be hard to force the supplied flow to operate at 90 degrees. This action could lead to large internal energy losses and decrease the device's energy efficiency. Due to this fact, 60° angle of blowing could be more practical but its important to estimate how it affects device's performance. In fig. 6.4 could be found definition of axis and angle of inclination which is measured from the x-axis. In fig. 6.5 and 6.6 could be observed that change of the angle of blowing leads to worse results. At $\alpha = 4°$, reduction of the drag is decreased from 34% at 90° up to 7% at 15°. This is 27% difference. At $\alpha = 12°$, it is observed that the drag reduction has its peak at 60° and total difference is around 1% in drag term. At both cases, lift is decreased and it looks that the effect on the lift is same at both cases. Total difference of the lift is around 5%.

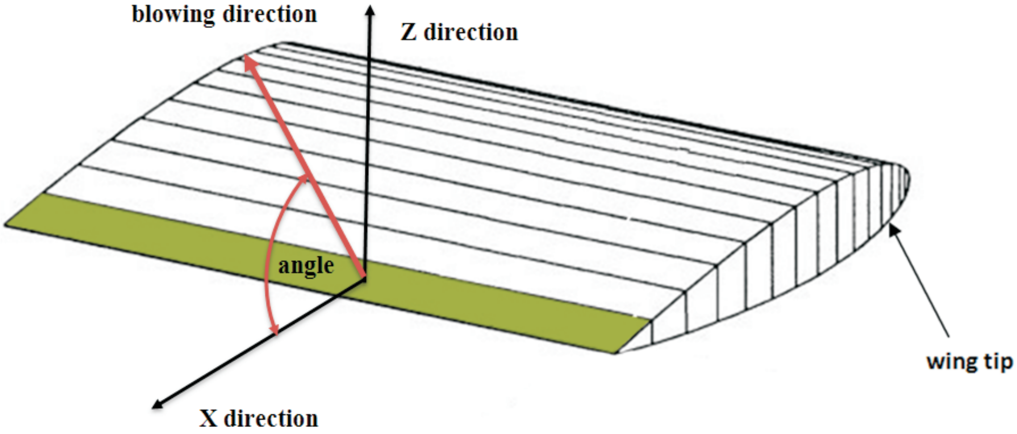

Figure 6.4: Sketch of configuration with inclination of the jets.

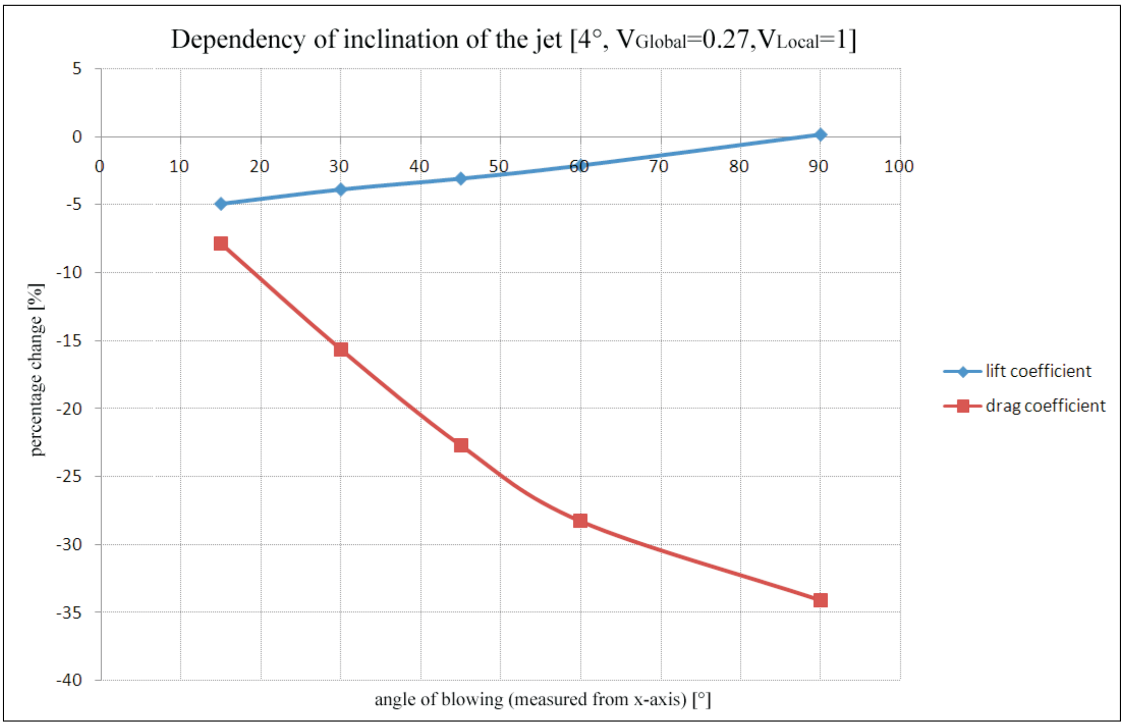

Figure 6.5: Dependence on angle of blowing$[\alpha = 4^{\circ}, V_{Global} = 0.27, V_{Local} = 1]$.

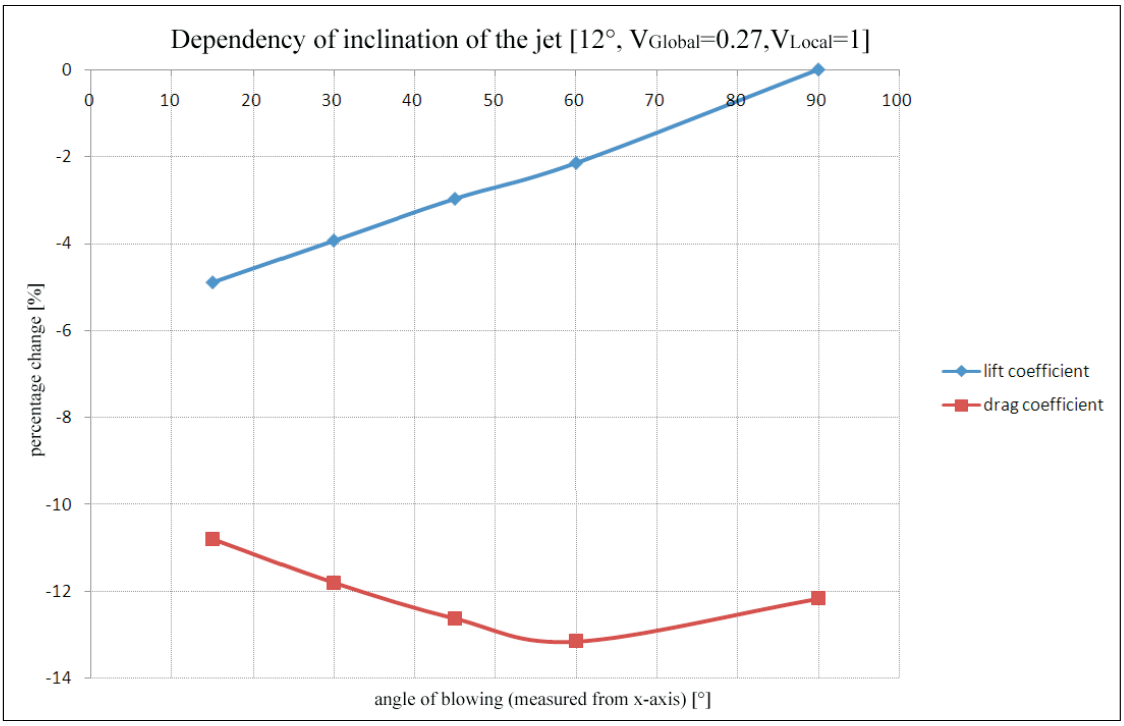

Figure 6.6: Dependence on angle of blowing$[\alpha = 12^{\circ}, V_{Global} = 0.27, V_{Local} = 1]$.

6.1.3 Effect of shift of the slots along the wingspan

In the present study, the slot is positioned at the trailing edge close to the wingtip. In section 5.2 is found that the current configuration has not significant effect on the induced drag force. Drag reduction gain is mainly due to the profile drag decrease. Due to the fact that induced drag is not significantly affected, it could be possible to shift the device toward to the wing root. This configuration could be important in case that AFC is not combined to ailerons. This configuration could be important, because original position of the slot collide with position of ailerons. In fig. 6.7 could be found sketch which defines positions of the slots. The slot is shifted one slot's length, this mean that a new slot ends at the same location where previous one starts. Impacts of this change are examined at $\alpha = 4°$ and $\alpha = 12°$. In tab. 10. it could be observed that the so-called "inner slots" have similar performances. The drag reduction is a little bit lower. The slot is far away from the wingtip area, thus this could be accounted to the induced drag. Also, it is tested the effect of the slot of the double length. It is observed that the drag reduction appears to be proportional to the length of the slot. At $\alpha = 4°$, the drag reduction increased from 34% up to 69%.

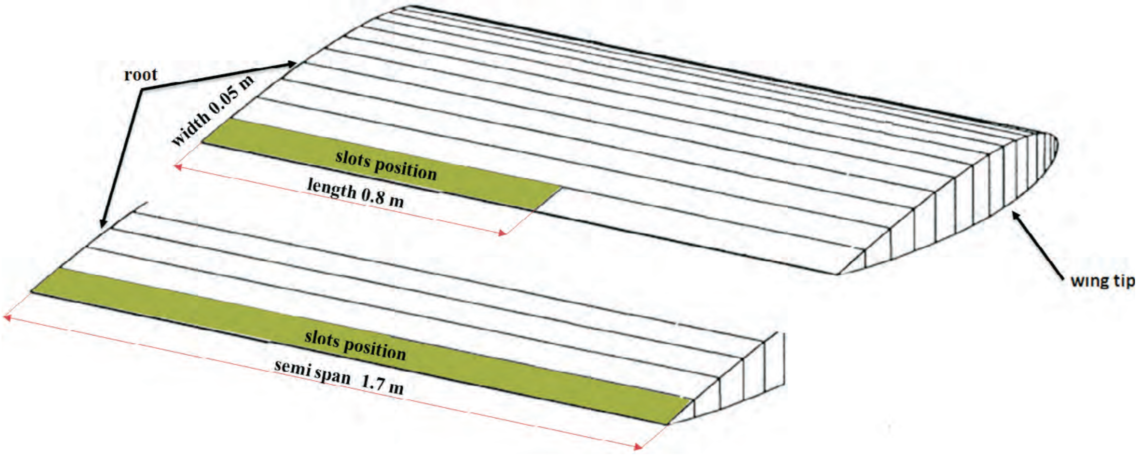

Figure 6.7: Sketch of position of the slots.

Tab10: **Effect of shift of slots along the wingspan:**

$\alpha = 4^\circ$ $V_{Global} = 0.27$ $V_{Local} = 1$	C_L [-]	C_D [-]	ΔC_L %	ΔC_D %
Natural flow	0.3189	0.0200	-	-
Classic slot configuration	0.3194	0.0132	+0.13	-34.1
New “inner slots”	0.3176	0.0132	-0.4	-32.7
New “double length of slots”	0.3182	0.0062	-0.2	-69.1

$\alpha = 12^\circ$ $V_{Global} = 0.27$ $V_{Local} = 1$	C_L [-]	C_D [-]	ΔC_L %	ΔC_D %
Natural flow	0.9021	0.0642	-	-
Classic slot configuration	0.9020	0.0564	0	-12.2
New “inner slots”	0.9078	0.0579	+0.6	-9.8
New “double length of slots”	0.9088	0.0511	+0.7	-20.5

6.1.4 Effect of separation of the slots

The trailing edge has a low construction height. It could cause problems when arranging the jets one above the other. In this section it is investigated the effect of the separated slots. The slots have the same dimensions and they are separated that one an inner slot lies in the inner part of the wing while the other lies in the outer part of the wing. This arrangement could be seen in fig. 6.8. In tab. 11 could be found summarized results. The term “inner slot down, outer slot up” means that blowing is applied downward on inner part of the wing and upward on outer part of the wing. It is observed that this design is not effective. This fact leads to the conclusion that observed benefits in previous arrangements are from favourable interaction between slots one above the other.

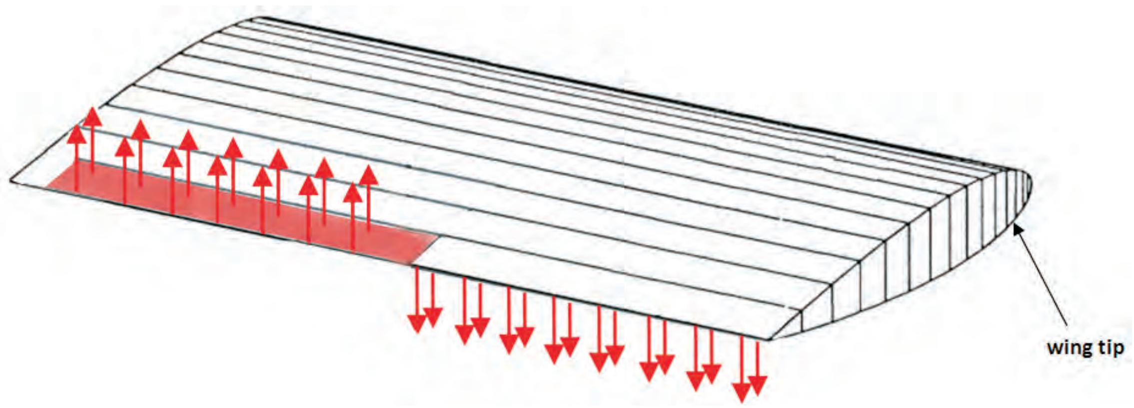

Figure 6.8: Sketch of position of the slots.

Tab11: **Effect of separation of slots:**

$\alpha = 4^\circ$ $V_{Global} = 0.27$ $V_{Local} = 1$	C_L [-]	C_D [-]	ΔC_L %	ΔC_D %
Natural flow	0.3189	0.0200	-	-
Classic slot configuration	0.3194	0.0132	+0.13	-34.1
New “inner slot down, outer slot up”	0.4031	0.0222	+26.4	+11.1
New “inner slot up, outer slot down”	0.2587	0.0236	-18.9	+17.6

$\alpha = 12^\circ$ $V_{Global} = 0.27$ $V_{Local} = 1$	C_L [-]	C_D [-]	ΔC_L %	ΔC_D %
Natural flow	0.9021	0.0642	-	-
Classic slot configuration	0.9020	0.0564	0	-12.2
New “inner slot down, outer slot up”	1.0045	0.06566	+11.4	+2.3
New “inner slot up, outer slot down”	0.8710	0.0725	-3.4	+12.9

6.2 Evaluation of benefits

In this section will be shown benefits of using AFC device implemented on the real airplane. Possible fuel savings together with overall airplane performances will be evaluated. For the purpose of comparison, it is chosen a small single engine plane VUT 100 COBRA manufactured by Evektor [41].

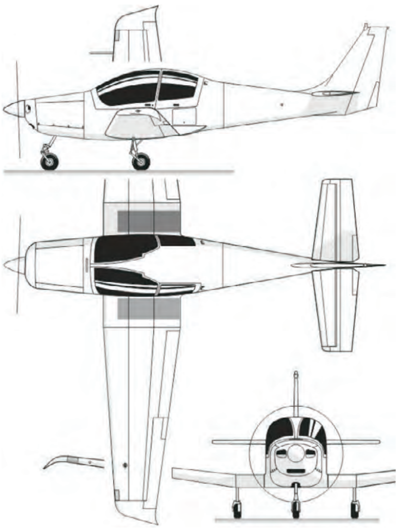

Figure 6.9: VUT 100 Cobra [14].

Tab9: **VUT 100 COBRA:**

Wing area	$S = 13,1m^2$
Wing span	$b = 10,2m$
Wing aspect ratio	$\lambda = 7,936$
Max. take-of weight	$M_{TOW} = 1330kg$
Engine	$Lycoming IO - 360/200hp$
Max. horizontal speed	$V_{max} = 280km/h$
Stall speed without flaps	$V_{S1} = 115km/h$
Stall speed with flaps	$V_{S0} = 95km/h$
Fuel capacity	$m_{fuel} = 240kg$
Range	$R = 2000km$

The drag polar of VUT100 airplane is taken from publication [5] page 149 (see appendix tab. A). For computation of airplane performances, it is favourable to express the real drag polar into, so called, an analytical lift-drag polar. General form of the analytical drag polar can be written as follow:

$$C_D = C_{D0} + \frac{1}{\pi \lambda e} C_L^2 \tag{6.1}$$

where C_D is drag coefficient, C_{D0} is zero-lift drag coefficient, C_L is lift coefficient, λ is aspect ratio of a wing and e is Oswald's efficiency factor. Second term ($\frac{1}{\pi \lambda e}$) is often called as parameter of the induced drag. With use of cubic spline approximation and previous equation, the drag polar of the VUT 100 Cobra could be expressed as:

$$C_D = 0.0296 + 0.0439 C_L^2. \tag{6.2}$$

The tested wing in this study is a rectangular with symmetrical airfoil. The VUT 100 has a trapezoid planform and it uses LS series of airfoils. Due to this fact, it is necessary to make some assumptions before proceeding to comparison.

Aerodynamic performance of the AFC device is not significantly affected by:

- different airfoils
- size and aspect ratio of the wing
- different Reynolds number.

Additional assumptions:

- The weight of the AFC device is considered to be less than 1% of the total weight, thus being negligible in terms of the demands in lift change.
- The real lift-drag polar can be substituted by symmetric analytical lift-drag polar . This is strong assumption because the VUT 100 Cobra have non-symmetrical airfoils. However, in this illustrative case only positive part of the lift-drag polars are used .

In the present study, a lift-drag polar (see fig. 5.44) is related to the wing. Since, the lift to drag polar of a plane VUT 100 is known, next step is to express the lift-drag polar of a Cobra's wing. However, the lift-drag polar of the wing is not known. Due to this fact, it is needed some kind of estimation. Figure 6.10 [27] shows an example of component drag breakdown for five airplanes. Based on this example, it is estimated that drag of the wing takes 36% of the airplane zero-lift drag (C_{D0}). Second term, a parameter of the induced drag, which appears in the analytical lift-drag polar is kept the same.

Suffix (w) represents term related to the wing and (CFD) the term related to the wing which is used in this study.

$$C_{D0w} = 0.36C_{D0} \tag{6.3}$$

Then, the lift-drag polar of the Cobra's wing could be expressed as:

$$C_{Dw} = 0.010656 + 0.0439C_L^2. \tag{6.4}$$

Now, it is ready for implementation of the AFC device on the Cobra's wing. Based on the result in section 5.4 regarding energy efficiency in controlled flow cases, one representative blowing condition is chosen. It is, so called, lift stabilized condition and it is used at all angles of attack. In fig. 5.44 regarding the lift-drag polar, it could be seen as a red line. Process of inclusion the AFC effect could be described as follow: for the natural flow case (blowing off) and blowing case (lift stabilized) is computed percentage drag

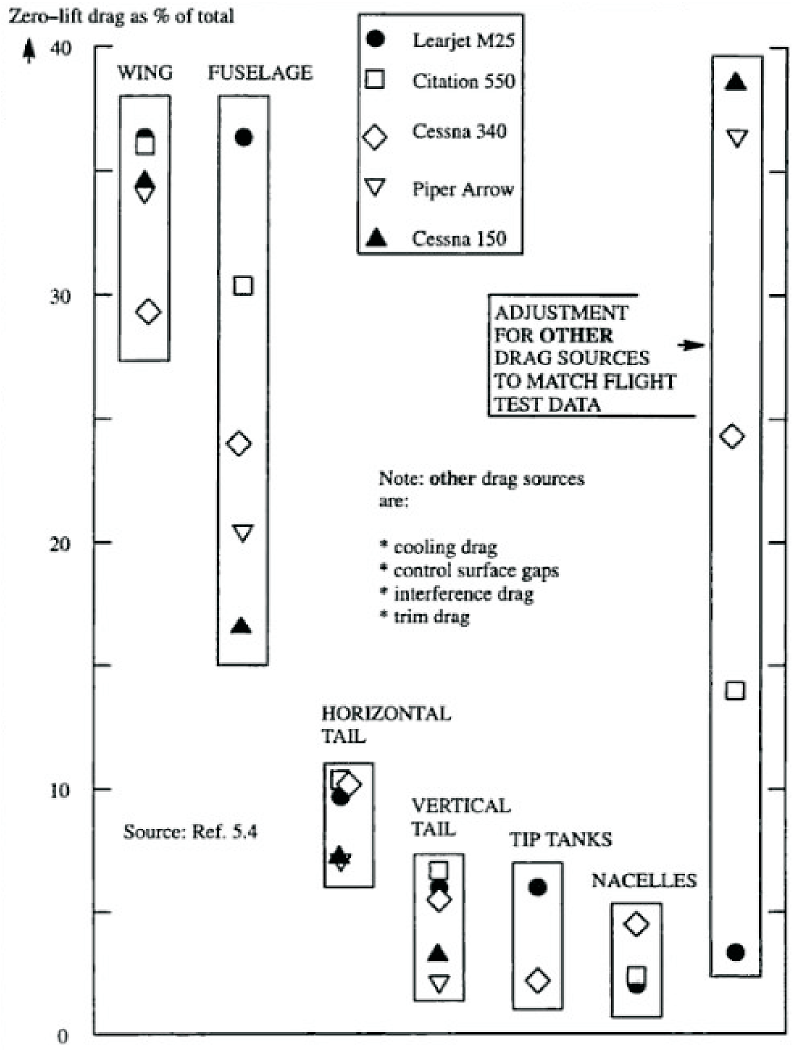

Figure 6.10: Drag force components [27].

difference at all lift coefficients. Then, the same drag difference is applied on the Cobra's lift-drag polar of a wing. This process is clearly visible in tab. 10 (see appendix tab. B). The lift-drag polar of the Cobra's wing with working AFC device could be expressed as:

$$C_{Dw}(AFC) = 0.00562 + 0.0456C_L^2 \tag{6.5}$$

and airplane analytical lift-drag polar as:

$$C_D(AFC) = 0.023972 + 0.0456C_L^2. \tag{6.6}$$

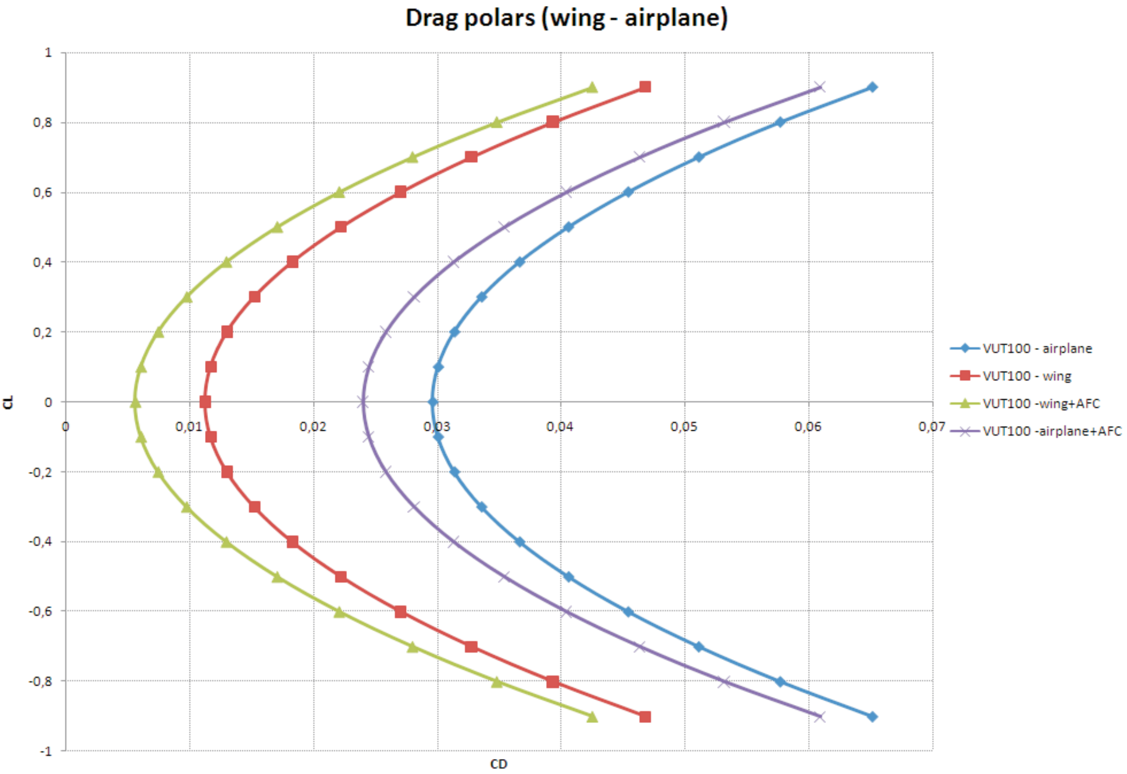

Figure 6.11: Lift-drag polars of VUT 100 Cobra.

Tab12: **Comparison of aerodynamic performances :**

VUT 100 Cobra		
Max. lift-drag ratio	K_{max}	13.87
Minimum drag speed	V_{mD}	46.71 m/s
Drag coefficient at K_{max}	C_{DKmax}	0.0592
Lift coefficient at K_{max}	C_{LKmax}	0.8211

VUT 100 Cobra with AFC device		
Max. lift-drag ratio	K_{max}	15.12
Minimum drag speed	V_{mD}	49.71 m/s
Drag coefficient at K_{max}	C_{DKmax}	0.0479
Lift coefficient at K_{max}	C_{LKmax}	0.7250

Before proceeding to the computations of flight performances, some further assumptions should be stated:

- specific fuel consumption is constant at cruise flight

- airplane configuration is without change

- propeller efficiency is constant

- angle of attack and angle of thrust inclination is close to the zero $\Rightarrow T \doteq D$.
- mass of the airplane is not constant (m $\neq$ constant)

Flight performances are computed at steady horizontal cruise flight at height of flight 0 m of standard international atmosphere.

Tab13: **Additional inputs:**

Heigh of flight	$H = 0m$ at standard atmosphere
Density	$\rho = 1.225 kg/m^3$
Fuel weight flow	$C_h = 0.35 kg/kWh$
Propeller efficiency	$\eta = 0.8$

Thrust required is thrust needed for overcoming drag of an airplane. It can be computed from equilibrium of thrust and drag force at steady horizontal flight (T=D).

$$T_{re} = \frac{C_D}{C_L} G \tag{6.7}$$

where T_{re} is required thrust, G is weight.

Available thrust T_{av} is an engine characteristic. It is obtained from [14] (see appendix tab. C).

Power required P_{re} is computed as:

$$P_{re} = T_{re} \cdot v \tag{6.8}$$

where v is velocity of flight.

It is necessary to include power required by blowing. This power could be estimated by equation 5.4:

$$P_{Blowing} = K \frac{\rho u_{bl}^3 A_{bl}}{2}.$$

For reasons of simplicity, global velocity ratio V_{Global} is constant and its value is 0.3. Overall internal losses are neglected and then $K = 1$. Blowing velocity u_{bl} is then computed as follow:

$$u_{bl} = V_{Global} \cdot V_\infty \tag{6.9}$$

where V_∞ is free stream velocity.

Power available P_{av} is computed as a shaft power $P_s h$ minus $P_{Blowing}$ and multiplied by propeller efficiency η:

$$P_{av} = (P_{sh} - P_{Blowing}) \cdot \eta. \tag{6.10}$$

Maximum horizontal speed is found at condition $P_{av} = P_{re}$. Sumarized results could be found in tab. 14. It could be seen that working device led to increase of maximum speed about 6 percent.

Tab14: **Maximum horizontal speed:**

V_{max} km/h	$V_{max}(AFC)$ km/h	change %
264	280	+6.06

Range is computed at condition of constant speed and height of flight. Consequently of mass reduction of the airplane, the lift coefficent vary in time. Range can be computed from equation [5] p.187:

$$R = \left(\frac{2\eta K_{max}}{gC_{eP}}\right) arctg \frac{\overline{m}_{fuel}\frac{C_{L1}}{C_{LK}}}{1+\frac{C_{L1}^2}{C_{LK}^2}\left(1-\overline{m}_{fuel}\right)} \tag{6.11}$$

where: K_{max} is maximum lift-drag ratio, g is gravity acceleration, C_{eP} is specific fuel consumption, $m\bar{_{fuel}} = 1 - \frac{m_2}{m_1}$, m_1 is mass of an ariplane at the beginning of cruise, m_2 is mass of an airplane at the end, C_{L1} is lift coefficient at current speed, C_{LK} is lift coefficient at speed of maximum lift-drag ratio K_{max}.

Sumarized results could be found in tab. 15. Average increment of range is about 17 % at speeds from 160 km/h up to 300 km/h.

Tab15: **Range:**

Cruise speed km/h	$Range$ km	$Range(AFC)$ km	change %
180	2240	2507	+11.9
220	1816	2130	+17.3
250	1521	1816	+19.4
265	1389	1669	+20.15

Fuel consumption could be expressed by reordering equation 6.11. In tab. 16, fuel savings at different cruise speeds with travel distance set to 500 km are quoted.

Tab16: **Fuel savings after distance of 500 km:**

Cruise speed km/h	$Fuel\ consumed$ kg	$Fuel\ consumed(AFC)$ kg	Fuel saving kg	Normalized saving %
180	57	51.5	5.5	9.6
220	68	58.7	9.3	13.7
250	80	67.9	12.1	15.1
265	88	73.6	14.4	16.4

7 Conclusion

In the present thesis, series of RANS calculations of the flow past a NACA 0015 wing at different angles of attack with active flow control have been performed. Active flow control devices were applied on the wing's surface at a Mach number of $M = 0.21$ and $Re = 2.5 \times 10^6$. Several types and placements were examined in order to find the most powerful and energy efficient configuration. The proposed concept in this study does not follow the conventional active control methods. Large blowing surfaces and low velocity magnitudes at the slot's exits are considered. Therefore, it is not necessary to use high momentum coefficients of the injected fluid. Although the momentum coefficient is similar to most of the referenced studies, it is found that the effects on the flow-field are totally different. It is found that the drag reduction is mainly caused by altering the pressure distribution on the wing. The induced drag itself is affected slightly and in some cases it is even higher. However, it is found that the device has positive effect on the evolution of the tip vortex. The tip vortex is more diffused which could be beneficial for the far-field decay of the trailing vortices. Strategies for drag reduction and lift increase of the wing are demonstrated thoroughly by varying some of the actuation parameters. The active control when operating under some specific conditions could reach very high energy efficiency ratios at all angles of attack, while in the same time could be able to reduce significantly the total drag of the wing, increase the total lift or combine effectively those favorable effects for better flight performance. Maximum drag decrease could exceed 40% of the total drag at low angles of attack, with still positive energy income.

The conclusions that have been drawn in this study can be summarized as follows:

- When applying simultaneous blowing to the upper and lower surfaces within a specific range of V_{Global} and V_{Local}, the lift could remain the same or increases, while the drag decreases.
- Local velocity ratio is found to be effective within $0.8 - 1.1$.
- The present active control affects globally and locally the flow field and the local effect is more significant.
- It is observed diffusion of the vortex in the near-wake of the wing in controlled flow regime.
- Drag reduction reaches up to 15% at $\alpha = 12^\circ$ and at $\alpha = 4^\circ$ it reaches up to 40% while the device is still energy efficient.
- Effect on the reduction of the induced drag is small. The effects of the active flow control device are clearly two dimensional.

- Position of the center of pressure is not significantly affected and at some controlled cases could be beneficial.
- Towards to the trailing edge, performance of the device is increased. The best performance is obtained close to the trailing edge.
- Decrease of the angle of blowing reduces the efficiency of the control.
- Effect of position of the device on the wing span is not significant. The device when shifted towards the wing root has similar performance.
- The drag reduction appears to be proportional to the length of the slot.

However, those conclusions can be considered valid only for this specific or similar wing configurations and at the aforementioned flow conditions. An additional effort needs to be put on the examination of behaviour at different flow conditions and wing configurations. In the present study, it is used a symmetrical airfoil. In future work, it would be necessary to examine device's behaviour on the wing with non-symmetric airfoil and its behaviour with real blowing surface configuration. Also, research on the field of structural design is imperative for future application of this concept. The proposed control surface which is placed close to the trailing edge might bring several difficulties. Further investigations are needed to confirm aforementioned conclusions. An experimental study performed in the wind tunnel could give much more insight into the validity of the present concept's results.

References

[1] Baker, A.J. *Finite element computational fluid mechanics*. McGraw-Hill Book Company, 1983.

[2] Chevalier, H. *Flight test studies of the formation and dissipation of trailing vortices*. SAE technical paper 730295, 1973.

[3] Coimbra, R.F.F., Catalano,F.M. *The effect of wingtip blowing on the vortex drag*. ICAS 2002 congress, 2002.

[4] Crow, S.C., Bate, E. R. *Lifespan of trailing vortices in a turbulent atmosphere*. Journal of aircraft. vol. 13, p. 476-482., July 1976.

[5] Danek, V: *Mechanika letu 1: Letove vykony*. ISBN:978-80-7204-659-1, CERM, Brno, 2009.

[6] Driver, D.M., Seegmiller,H.,L. *Features of a reattaching turbulent shear layer in divergent channel flow*. The American institute of aeronautics and astronautics journal (AIAA), vol. 23, 1985.

[7] Dunham, R.E. *Unsuccessful concepts for aircraft wake vortex minimization*. NASA technical report SP-409, 1976.

[8] Geissler, W. *A family of CFD boundary conditions to simulate separation control*. Aerospace Science and Technology 14, Elsevier Science Ltd., 2010.

[9] Gerz, T., Holzapfel, F., Darracq, D. *Commercial aircraft wake vortices*. Progress in aerospace sciences, Elsevier Science Ltd., 2002.

[10] Hallock, J.N, Eberle, W.R. *Aircraft wake vortices*. Federal aviation administration report FAA-RD-77-23, 1977.

[11] Heyes, A.L, Smith, D.A.R. *Spatial perturbation of a wing-tip vortex using pulsed span-wise jets*. Experiments in fluids, vol.37, Springer-Verlag, 2004.

[12] Hoerner, S.F. *Fluid-dynamic drag*. USA: Hoerner fluid dynamics, 455 p., ISBN 999-11-9444-4, 1965.

[13] Hoerner, S.F. *Aerodynamic shape of the wing tips*. US air force technical report 5752, 25, 1949.

[14] Janhuba, L: *Modification of horizontal tail of VUT 100 aircraft*. Master thesis, Brno University of technology, 2011.

[15] Katz, J., Plotkinn, A. *Low-speed aerodynamics*. McGraw-Hill,Inc., ISBN 0-07-100876-4, 1991.

[16] Kroo, I. *Nonplanar wing concepts for increased aircraft efficiency*. lecture series on innovative configurations and advanced concepts for future civil aircraft, Stanford University, 2005.

[17] Lanchester, F.W. *Aerodynamics*. A. Constable & co., ltd., 442 p.,1907.

[18] Lim, Hock-Bin. *Numerical study of the trailing vortex of a wing with wing-tip blowing*. Joint institute for aeronautics and acoustics, JIAA TR-112, Stanford University, 1994.

[19] Margaris, P., Gursul, I. *Vortex topology of wing tip blowing*. Aerospace science and technology 14, p. 143-160, 2009.

[20] McAlister, K.W, Takahashi, R.K. *NACA 0015 wing pressure and trailing vortex measurements*. NASA technical report 3151, 1991.

[21] Mineck, R.E.. *Study of potential aerodynamic benefits from spanwise blowing at wingtip*. NASA technical report 3515, 1995.

[22] Monsch, S.Ch. *A study of induced drag and spanwise lift distribution for three-dimensional inviscid flow over a wing* . Master thesis, the Graduate School of Clemson University, 2007.

[23] Olsen, J.H, Goldburg, A., and Rogers, M. *Aircraft wake turbulence and its detection*. Proceedings of a symposium on aircraft wake turbulence, Seattle, 1971.

[24] Peric, M. *Numerical methods for computing turbulent flows*. Technical report VKI LS 2004-06, Computional Dynamics Ltd., 2004

[25] Pope, S.B. *Turbulent flows*. Cambridge University press, England, 1995.

[26] Rorke, J.B, Moffitt, R.C. *Wind tunnel simulation of full scale vortices*. NASA technical report CR-2180, 1973.

[27] Roskam, J., Lan Edward, Ch-T. *Airplane aerodynamics and performance*. Design, analysis and research corporation, ISBN 1-884885-44-6, 2003.

[28] Roumeas, M., Gillieron, P., Kourta, A. *Analysis and control of the near-wake flow over a square-back geometry*. Computers & Fluids vol.38, Elsevier, 2009.

[29] Smith, G.D. *Numerical solution of partial differencial equations : finite difference methods*. Oxford applied mathematics & computing science series, Clarendon Press, 1985.

[30] Spalart, P.R., Allmaras, S.R. *A one equation turbuence model for aerodynamic flow*. La Recherche aerospatiale, 1994.

[31] Tavella, D.A., Roberts, L. *A theory for lateral wing-tip blowing*. Joint institute for aeronautics and acoustics, report JIAA TR-60, 1985.

[32] Tavella, D.A., Wood, N., Harrits, P. *Measurements on wing-tip blowing*. Joint institute for aeronautics and acoustics, report JIAA TR-64, 1985.

[33] Tavella,D.A., Wood, N.J., Lee, C.S. *Lift modulation with lateral wing-Tip blowing*. Journal of aircraft, Vol. 25, 1988.

[34] Versteeg, H.K., Malalasekera, W. *An introduction to computional fluid dynamics: The finite volume method*. ISBN: 978-0582218840, Longman Group, 1995.

[35] Whitcomb, R.T. *A Design approach and selected wind-tunnel results at high subsonic speeds for wing-tip mounted winglets*. NASA technical report TN-D-8260, 1976.

[36] Yadlin, Y., Shmilovich, A. *Flow control of airplane trailing wakes*. 9th Symposium on overset composite grid and solution technology, Penn State University, Boeing, 2008.

[37] Yang Ch. et al. *Comprehensive study on tip vortex with lateral jet flow*. Transactions of the Japan society for aeronautical and space sciences, vol. 46, 2003.

[38] Zienkiewicz, O.C., Taylor, R.L. *The finite element method*. Butterworth and Heinemann, 6th edition, ISBN:0-7506-6322-7, 2006.

[39] Zimmer, H. *The Aerodynamic optimization of wings at subsonic speeds and the influence of wingtip design*. NASA report TM-88534, 1987.

[40] *Ansys Fluent 12.0: Theory guide*. Ansys,Inc., 2009.

[41] Single engine airplane VUT 100 COBRA. *http://www.evektor.en*.

Appendix:

Tab. A Drag polar [5] p.149:

C_L	C_D	C_L/C_D
0,164	0,03041	5,29
0,262	0,03271	8,01
0,363	0,03576	10,15
0,464	0,03952	11,74
0,565	0,04388	12,88
0,666	0,04920	13,54
0,767	0,05530	13,87
0,868	0,06222	13,95
0,968	0,07008	13,81
1,069	0,07905	13,52
1,170	0,08939	13,09
1,270	0,10151	12,51

Tab. B Drag polar calculation:

C_L	$C_{Dw}(CFD)$ Natural case	$C_{Dw}(CFD)$ Lift stabilized	Diffrence [%]	C_{Dw} VUT 100	Diffrence [%]	$C_{Dw}(AFC)$ VUT 100
-0,9	0,06229	0,05661	9,11	0,04681	9,11	0,04254
-0,8	0,05226	0,04624	11,5	0,03934	11,5	0,03481
-0,7	0,04341	0,03709	14,5	0,03276	14,5	0,02799
-0,6	0,03574	0,02916	18,4	0,02705	18,4	0,02207
-0,5	0,02925	0,02245	23,2	0,02222	23,2	0,01706
-0,4	0,02394	0,01696	29,1	0,01827	29,1	0,01294
-0,3	0,01981	0,01269	35,9	0,0152	35,9	0,00974
-0,2	0,01686	0,00964	42,8	0,01300	42,8	0,00744
-0,1	0,01509	0,00781	48,2	0,01169	48,2	0,00605
0	0,0145	0,0072	50,3	0,01125	50,3	0,00559
0,1	0,01509	0,00781	48,2	0,01169	48,2	0,00605
0,2	0,01686	0,00964	42,8	0,01300	42,8	0,00744
0,3	0,01981	0,01269	35,9	0,01520	35,9	0,00974
0,4	0,02394	0,01696	29,1	0,01827	29,1	0,01294
0,5	0,02925	0,02245	23,2	0,02222	23,2	0,01706
0,6	0,03574	0,02916	18,4	0,02705	18,4	0,02207
0,7	0,04341	0,03709	14,5	0,03276	14,5	0,02799
0,8	0,05226	0,04624	11,5	0,03934	11,5	0,03481
0,9	0,06229	0,05661	9,11	0,04681	9,11	0,04254

Tab. C Available thrust [14]:

Height [meters]	0	1000	2000
Power [hp/kW]	200/147,1	179/131,6	159/116,9
TAS [m/s]	Available thrust [N]		
0	3900	3518	3134
5	3718	3305	2944
10	3500	3101	2763
20	3065	2722	2426
30	2685	2383	2123
40	2348	2081	1854
50	2055	1819	1619
60	1806	1598	1421
70	1599	1413	1255
80	1422	1256	1116
90	1276	1126	1000
100	1150	1015	900
110	1042	919	815
120	949	836	741
130	866	762	675